Mixing Under Transcritical Flow Conditions

Sebastien Candel
J. Rodriguez
T. Schmitt

Ecole Centrale Paris
EM2C Laboratory, CNRS
Chatenay-Malabry, France 92295

March 2011

Final Report for 08 October 2009 to 08 February 2011

**Air Force Research Laboratory
Air Force Office of Scientific Research
European Office of Aerospace Research and Development
Unit 4515 Box 14, APO AE 09421**

REPORT DOCUMENTATION PAGE			Form Approved OMB No. 0704-0188

Public reporting burden for this collection of information is estimated to average 1 hour per response, including the time for reviewing instructions, searching existing data sources, gathering and maintaining the data needed, and completing and reviewing the collection of information. Send comments regarding this burden estimate or any other aspect of this collection of information, including suggestions for reducing the burden, to Department of Defense, Washington Headquarters Services, Directorate for Information Operations and Reports (0704-0188), 1215 Jefferson Davis Highway, Suite 1204, Arlington, VA 22202-4302. Respondents should be aware that notwithstanding any other provision of law, no person shall be subject to any penalty for failing to comply with a collection of information if it does not display a currently valid OMB control number. **PLEASE DO NOT RETURN YOUR FORM TO THE ABOVE ADDRESS.**

1. REPORT DATE *(DD-MM-YYYY)*	2. REPORT TYPE	3. DATES COVERED *(From – To)*
03-03-2011	Final Report	08 October 2009 - 08-February 2011

4. TITLE AND SUBTITLE	5a. CONTRACT NUMBER
Mixing Under Transcritical Flow Conditions	FA8655-10-1-3005

5b. GRANT NUMBER

Grant 10-3005

5c. PROGRAM ELEMENT NUMBER

61102F

6. AUTHOR(S)	5d. PROJECT NUMBER
Sebastien Candel	
J. Rodriguez	**5d. TASK NUMBER**
T. Schmitt	
	5e. WORK UNIT NUMBER

7. PERFORMING ORGANIZATION NAME(S) AND ADDRESS(ES)	8. PERFORMING ORGANIZATION REPORT NUMBER
Ecole Centrale Paris EM2C Laboratory, CNRS Chatenay-Malabry, France 92295	N/A

9. SPONSORING/MONITORING AGENCY NAME(S) AND ADDRESS(ES)	10. SPONSOR/MONITOR'S ACRONYM(S)
EOARD Unit 4515 BOX 14 APO AE 09421	AFRL/AFOSR/RSW (EOARD)
	11. SPONSOR/MONITOR'S REPORT NUMBER(S)
	AFRL-AFOSR-UK-TR-2011-0001

12. DISTRIBUTION/AVAILABILITY STATEMENT

Approved for public release; distribution is unlimited. Available only to U.S. Government or Federal Purpose Rights License.

13. SUPPLEMENTARY NOTES

14. ABSTRACT

The project focused on the mixing behavior of fluids under transcritical flow conditions. This topic is relevant to rocket propulsion applications and it is also applicable to other high pressure systems such as gas turbine combustors. Extensive work in this general area of propulsion has been performed at the EM2C (Energetique, Moleculaire, Macroscopique et Combustion) laboratory at Ecole Centrale Paris (ECP) which has suitable complemented the experimental work that has been recently conducted at the Air Force Research Lab at Edwards Air Force Base. The report, which is divided in three major parts, encompasses the results of modeling efforts, further analysis of experimental data, and comparisons between the two. The first part deals with the Large-Eddy Simulation of non-reactive shear coaxial jets, the second part expands on the area of spectral analysis and the final part presents the work performed using an in-house code developed by the Numerical Combustion Group of the EM2C laboratory. This code is based on the Direct Numerical Simulation technique.

15. SUBJECT TERMS

EOARD, Fluid Dynamics, Rocket Engines

16. SECURITY CLASSIFICATION OF:			17. LIMITATION OF ABSTRACT	18, NUMBER OF PAGES	19a. NAME OF RESPONSIBLE PERSON
a. REPORT	b. ABSTRACT	c. THIS PAGE			Brad Thompson
UNCLAS	UNCLAS	UNCLAS	SAR	106	19b. TELEPHONE NUMBER *(Include area code)* +44 (0)1895 616163

GRANT/COOPERATIVE AGREEMENT DELIVERABLE

TYPE : FINAL REPORT (ITEM 0003)

TITLE : MIXING UNDER TRANSCRITICAL FLOW CONDITIONS

INVESTIGATORS: T. SCHMITT, J. RODRIGUEZ, S. CANDEL

AWARD NO. : FA8655-10-1-3005

ISSUING AGENCY OFFICE :
European Office of Aerospace Research and Development
86 Blenheim Crescent
Ruislip, Middlesex HA4 7HB
United Kingdom

GRANT RECIPIENT :
Centrale Recherche SA
8 Rue Jean Goujon
75008 Paris, France

LOCATION :
EM2C Laboratory, CNRS
École Centrale Paris
92295 Châtenay-Malabry, France

Mixing under Transcritical Flow Conditions: EOARD Sponsored Research Final Report (FA8655-10-1-3005)

J. Rodriguez, T. Schmitt, S. Candel

March 1, 2011

Contents

Summary

This document presents the work performed under the auspices of the Air Force Office of Scientific Research (AFOSR) through the European Office of Aerospace Research and Development (EOARD) with award number FA8655-10-1-3005. The project focused on the mixing behavior of fluids under transcritical flow conditions. This topic is relevant to rocket propulsion applications and it is also applicable to other high pressure systems such as gas turbine combustors. Extensive work in this general area of propulsion has been performed at the EM2C (Energétique, Moléculaire, Macroscopique et Combustion) laboratory at École Centrale Paris (ÉCP) which has suitable complemented the experimental work that has been recently conducted at the Air Force Research Lab (AFRL) at Edwards, Air Force Base (AFB) in California. The report, which is divided in three major parts, encompasses the results of modeling efforts, further analysis of experimental data, and comparisons between the two. The first part deals with the Large-Eddy Simulation (LES) of non-reactive shear coaxial jets, the second part expands on the area of spectral analysis and the final part presents the work performed using an in-house code developed by the Numerical Combustion Group of the EM2C laboratory. This code is based on the Direct Numerical Simulation (DNS) technique.

Introduction

The following report is divided into three parts which present different aspects of non-reactive transcritical flows with applications in liquid rocket engine environments and other propulsion and power generation systems. Part I of the report is concerned with the large eddy simulation of coaxial jets injected under transcritical conditions. In particular, three transcritical experimental cases performed by the Combustion Devices Group at AFRL were modeled. This type of flows feature a shear coaxial geometry that presents many interesting challenges such as understanding and quantifying mixing behavior and spreading of the inner jet into the outer jet and the surrounding fluid. The thermodynamics of flows near the critical point of the fluid - a point which indicates the beginning of a thermodynamic region where the state of the fluid cannot be distinguished between liquid and gas - are also complex, with some properties acquiring unusual values such as zero surface tension and zero heat of vaporization. The flow dynamics of such cryogenic, transcritical shear coaxial jets are of interest because of their widespread use as propellant injectors. The latter also makes them ideal candidates for the analysis of combustion instabilities. It is desired to have a better understanding of how the inner and outer streams of a coaxial jet interact, mix and burn in such conditions to be able to model spatial and temporal release of energy more accurately. This in turn will aid in analyzing coupling phenomena between the injector flow and the combustion chamber modes which are mechanisms that produce oscillations in pressure and temperature that could lead to undesired phenomena such as very high heat flux at the combustion chamber walls. Numerical simulation helps uncover details that cannot be found using experimental techniques, such as knowing the value of the velocity vector at any desired position in the flow and easily extracting spectral properties from a given location.

These spectral properties are analyzed in Parts I and II of this report. The spectral analysis of Part I focuses on the analysis of the flow structures and their associated spectral content as observed in the simulations. For cases with no acoustic modulation, numerical probes were placed in points of interest within the flow to analyze their spectral content. For instance, in regions where a strong recirculation zone is observed or at a point where a mixing layer is present. Using this analysis, preferred modes or frequencies of the system are retrieved and associated Strouhal numbers calculated. The spectral analysis in Part I also includes simulations with acoustic modulation for the purpose of understanding more the combustion instability phenomena as described above. For the cases with acoustic modulation, the spectral content was obtained not only for one point but also for an entire line of locations, in order to follow the dynamics of the flow along that particular axis. Results are shown at the end of Part I of this report. All contents of Part I were submitted as an article for publication in the journal Physics of Fluids and are currently under review.

Part II of this report deals with the analysis of the spectral content of coaxial jets injected under transcritical conditions with the same goal of identifying any periodicities in our data sets. The data sets analyzed now include some of the experimental data gathered at AFRL. The signal from which spectral content is extracted is the intensity of light at each pixel from images captured by a high-speed camera. Spectral maps are obtained from experimental cases with and without acoustic modulation. The same axes as those used in Part I of this report were used to allow comparison. Spectral analysis is a technique that could be used extensively with other experimental datasets already obtained at AFRL to analyze frequency content. The results of this technique applied to cases without acoustic modulation and their comparison with selected simulation results are shown first. The second set of results consists of cases with acoustic modulation. Spectral maps of both experimental data and simulation results are shown. It is found that both techniques clearly identify the modulation frequency. As an interesting note, given

the difference in the nature of the signal used from each type of data, the quantitative comparison of the physical location of the mode for one of the cases is remarkable.

The last part of this report focuses on the use of a direct numerical simulation tool to model nitrogen flows. DNS is often used to evaluate certain flow properties from which suitable subgrid-scale (SGS) models are developed to be used in LES. These "subgrid-scale" models are needed in LES because an LES grid is too coarse to resolve the smallest eddies and flow patterns present in the flow. Since the way in which the flow behaves and turns at the smallest scales is responsible for an important energy transfer step (of kinetic energy into heat) within the flow the need to know how these smallest eddies and flow patterns behave is very important. DNS grids do resolve even the smallest scales of the flow so they are able to take into account this energy transfer within the flow; however, using a DNS grid to model the flow of a rocket engine combustion chamber or around an aircraft engine turbine blade would be impossible given the number of grid points such a problem would require. This is why in practice DNS is limited to very simple geometrical domains.

Nonetheless, LES of transcritical and supercritical flows is feasible and DNS has been used to obtain SGS models to incorporate them to LES codes. Parts I and III discuss some of the groups involved in this type of research. In Part III, the direct simulation of nitrogen flow using a DNS tool developed at the EM2C laboratory of ÉCP is considered. It explains its capabilities, the different thermodynamic modules available for the user, and the validation performed using a one-dimensional direct numerical simulation. This part contains results of a 2D simulation of the evolution of a shear layer formed between two nitrogen streams flowing in opposite directions. The simulation provides detailed evolution of a smooth transition between the two flows into large vortices which eventually merge to form larger ones highlighting the mechanics of vortex pairing.

Part I

Modeling of Transcritical Mixing using Large Eddy Simulation

Experiments and numerical simulation of mixing under supercritical conditions

Authors: T. Schmitt[1], J. Rodriguez[1,2], I. A. Leyva[2] and S. Candel[1]

[1]EM2C, CNRS, École Centrale Paris, 92295 Châtenay-Malabry, France,
[2]AFRL/RZSA, Edwards AFB, CA. 93524, USA

List of Figures

List of Tables

Chapter 1

Abstract

Supercritical conditions designate a situation where the working fluid pressure is above the critical point. Among these conditions, it is interesting to identify a transcritical range which corresponds to cases where the pressure is above the critical point, but the injection temperature is below the critical value. This situation is of special interest because it raises fundamental issues which have technological relevance in the analysis of flows in liquid rocket engines. This situation is here envisaged by analyzing the behavior of a nitrogen shear coaxial jet comprising an inner stream injected at temperatures close to the critical temperature and a coaxial flow at a higher temperature. Experiments are carried out both in the absence of external modulation and by imposing a large amplitude transverse acoustic field. Real gas Large Eddy Simulations are performed for selected experiments. The combination of experiments and calculations is used to evaluate effects of injector geometry and operating parameters. Calculations retrieve what is observed experimentally when the momentum flux ratio of the outer to the inner stream $J = (\rho_e u_e^2)/(\rho_i u_i^2)$ is varied. Results exhibit the change in flow structure and the development of a recirculation region when this parameter exceeds a critical value. The instantaneous flow patterns for different momentum flux ratios are used in a second stage to characterize the dynamical behavior of the flow in terms of power spectral density of velocity and density fluctuations. Results obtained under acoustic modulation provide insight on mixing enhancement of coaxial streams with a view of its possible consequences in high frequency combustion instabilities. It is shown in particular that the presence of strong acoustic modulations notably reduces the high density jet core length, indicating an increased mixing efficiency. This behavior is more pronounced when the jet is placed at the location of maximum transverse velocity fluctuations.

Chapter 2

Introduction

Flows formed by coaxial injectors raise many fundamental issues. Such flows are also of practical relevance for high performance cryogenic liquid rocket engines (LREs). It is important to understand the basic processes taking place in these flows to improve the design methodology for future cryogenic LREs. Another potential application of research reported in this article lies in the area of combustion instability. It is known that mechanisms driving combustion oscillations result from the coupling between the injector flow, the combustion process and the chamber acoustic modes. The manner in which the inner and outer streams originating from a coaxial element interact with each other and with their surroundings may affect the temporal and spatial release of chemical energy within the chamber leading to undesired oscillations associated with a resonant acoustic motion. In most LREs, performance has been enhanced by augmenting the chamber pressure. Current LOx/H_2 engines like the SSME, Vulcain2 and RS-68 operate at values exceeding the critical pressure of their individual propellants. The inner jet, oxygen, is generally injected in a transcritical or liquid-like state (*i.e.* at a pressure higher than the critical value but at a temperature lower than the critical temperature) and it is surrounded by a higher-velocity hydrogen stream at supercritical temperature [72]. The inner fluid stream injected in a transcritical form evolves to a supercritical state as its temperature rises because of mixing and possibly combustion. Under such thermodynamic conditions, the system exhibits particular features that differ from those of a two-phase flow or of a pure gaseous injection. The objective of the present work is to compare experiments and simulations in which shear coaxial jet configurations are established at pressures above the critical point of the injected fluid, but at transcritical temperatures without and with acoustic excitation. For this study, nitrogen (N_2) is the only fluid used in the inner, outer and chamber flows.

At this point it is worth reviewing previous work dealing with supercritical injection. Starting with single round-jets, experiments have been carried out at AFRL (Air Force Research Laboratory) [9] and DLR (Deutsches Zentrum für Luft- und Raumfahrt) [29, 41] (see also Oschwald *et al* [43] for a review up to 2006). Some recent investigations are reported by Segal and Polikov [61] and Roy and Segal [56]. These studies indicate that the liquid break-up and atomization mechanism which prevail at subcritical pressure is no longer observable because surface tension and latent heat of vaporization vanish at supercritical pressures [47]. The jet of fluid then dissolves in the ambient gas, with no evidence of droplets. The flow features "comb-like" structures at the edge of the dense stream a type of pattern which is not observed at subcritical pressures [9]. The geometry of the flow is reminiscent of that of a variable density turbulent gas stream [9]. This behavior has been confirmed by experimental measurements of visual spreading rates in the initial region which are found to be consistent with theoretical growth rate expressions for incompressible variable-density turbulent mixing layers. Quantitative measurements of density [4, 41, 29],

spreading rate and axial decay coefficients obtained by DLR [43, 40] using spontaneous Raman scattering also convey the same type of information.

Coaxial injection is investigated by several researchers at AFRL [14, 13, 25, 24, 55, 54] who examine the single-species case, and by Mayer and Smith [30] who examine a stream of nitrogen injected at low temperature (high density) surrounded by a high velocity stream of moderate temperature helium. Quantitative measurement of species density are reported by Oschwald *et al* [42] for a coaxial nitrogen / hydrogen injection, using spontaneous Raman Scattering. When compared with the round jet configuration, a strong reduction of the jet density potential core length is observed [43]. For shear coaxial jets, it has been found that the momentum flux ratio between the outer stream and the inner jet ($J = (\rho_e u_e^2)/(\rho_i u_i^2)$) is of major importance for the mixing efficiency [22, 69]. It has also been found that combustion is more stable and more efficient at high values of this quantity [5]. Different flow regimes may be obtained by varying this ratio [51] and that the inner jet core length decreases as the momentum flux ratio increases [13, 25].

The dynamics of coaxial transcritical jets is of interest for the study of combustion instability. This can be examined by considering the interaction of acoustic waves with transcritical flows and its influence on mixing efficiency. Effects of an acoustic modulation on a single round jet at sub- and supercritical pressure is investigated by Chehroudi and Talley [8] who find that effects on the jet structure are more profound in the subcritical case. The impact of the modulation is reduced as the initial jet velocity is augmented. The impact of acoustics on a non-reacting shear coaxial jet has been investigated experimentally by Leyva and Rodriguez [25, 24, 55, 54]. They have assessed the effects of acoustics on the jet by measuring the spreading angle of the inner and outer jets and the length of the inner jet before its first break-up. It has been found that the injector geometry has an effect on the susceptibility of the coaxial flows to acoustic modulation. For the injector geometry studied here, acoustics have a measurable effect on the reduction of the inner jet dark core length for an intermediate value of J at pressures varying from 1.5 to 5.0 MPa. Reactive cases were also experimentally investigated (see [5, 19, 67, 64, 65] for example, and [53, 32] for acoustically modulated cases) but will not be detailed here since they are out of the scope of the present article.

The numerical modeling of such complex flows has been considered more recently by various groups. It is first noted that in the transcritical range, thermodynamic properties notably differ from those of a perfect gas and cannot be accurately represented with the standard perfect gas (PG) equation of state (EOS). Thermodynamics and "real-gas" (RG) EOS are required [47, 15, 71]. Cubic equations of state are generally used to this purpose [37], but more precise (and numerically expensive) equations may also be employed [71]. This issue and the modeling of transport properties are extensively reviewed in [1], [37], [31] and [2].

The models described in the previous studies are used in various calculations. Mixing at supercritical pressure is studied with direct numerical simulation in a mixing layer configuration, to show the role of density gradients on the global layer stability and turbulence characteristics and the strong effect on the molecular mixing of the reduced species diffusion near critical conditions [2]. This highlights the need for approriate subgrid-scale models for Large Eddy Simulation (LES) under supercritical pressure conditions [63, 68].

A few large eddy simulations (LES) have been performed under transcritical conditions. An extensive review of non-reacting LES in the period ending in 2006 can be found in Zong et al. [76]. A single nitrogen round jet was studied by Zong [74, 73] and recently by Schmitt *et al* [59]. Again, the stabilizing effect of the density gradient, and its role on turbulent energy redistribution along the mixing layer was identified [74]. Shear coaxial injection of oxygen and methane has also been simulated by Zong and Yang [75]. This has been continued by considering a non-reactive coaxial injector submitted to acoustic modulations [26]

15

where a significant reduction of the jet intact core length is observed when acoustic perturbations are present.

One also notes that LES have been used for reactive cases at supercritical pressures. Shear coaxial jet flames were investigated by Oefelein [37, 38], Oefelein and Yang [36], Zong and Yang [77], Matsuyama *et al.* [28], Masquelet *et al.* [27] and Schmitt *et al.* [57]. The problem is also considered in the Reynolds Average Navier-Stokes (RANS) framework (see for example [16], [11] or [49]).

The present investigation focuses on the mixing behavior in the flow originating from a shear coaxial injector in the absence or in the presence of external acoustic modulation. Three operating points are considered corresponding to different momentum flux ratios. The coaxial jet geometry corresponds to a thick inner jet post (the wall which separates the inner and outer streams in the coaxial configuration has a thickness of the order of the jet diameter). In this article each case is defined by the chamber pressure, the momentum flux ratio, and the coaxial jet geometry which is fixed in the present study. The main components of the experimental facility are reviewed in chapter 3. Balance equations and models used in the simulations are briefly described in chapter 4. The definition of the computational domain and other numerical aspects are considered in chapter 5. The influence of the momentum flux ratio is examined in chapter 6. Results obtained are used to examine the dynamics of the flow and identify the spectral content in the various regions. Effects of a transverse acoustic modulation are investigated in chapter 7.

Chapter 3

Experimental configuration

The experimental work described in this article was carried out at the Supercritical Cryogenic Test Facility (EC-4) of the Air Force Research Laboratory at Edwards Air Force Base, California. The facility features a test chamber that can achieve pressures over 5 MPa and cryogenic injection at temperatures below 120 K. The photograph in Fig. 3.1(a) shows the main test chamber and several key components of the facility. A schematic view of the test chamber is provided in Fig. 3.1(b). The facility was used to obtain a shear coaxial jet flow where the inner jet was cooled down to be denser than the outer jet under typical combustion chamber pressures, resembling conditions found in practice where the inner jet oxidizer is injected at a significantly lower temperature compared to that of the outer jet stream. A second equally important objective was to include the capability to perform acoustic forcing. When this was achieved the coaxial jet flow parameters were varied and the coaxial jet behavior was observed with and without acoustic excitation.
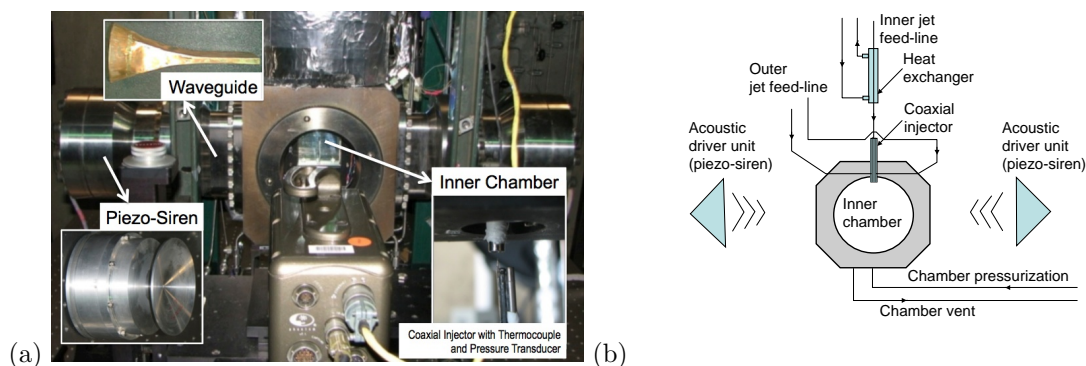
Figure 3.1: (a) Photograph of the main test chamber and key instrumentation of EC4, the supercritical cryogenic facility at AFRL, Edwards AFB. (b) Flow diagram of the test chamber and its vicinity.

To run a test, a laboratory-wide high pressure gaseous nitrogen supply was fed into the inner and outer flow lines of the coaxial jet and the flow rates adjusted to correspond to those of the desired test conditions. The mass flow rates through the inner and outer jets were measured with Porter mass flow meters (models 122 and 123-DKASVDAA). The same gaseous nitrogen supply used for the coaxial jet

was also employed to increase the pressure in the test chamber and achieve the required level, which was measured with a Stellar 1500 transducer. The jet temperatures were controlled by adjusting the flow rates of liquid nitrogen through the heat exchangers placed on the feed lines. Densities of the two jets were deduced from the measured temperatures and pressure using the National Institute of Standards and Technology's thermophysical properties of fluid systems online database [23]. These values in conjunction with the mass flow rate data provided the injection velocities and the corresponding Reynolds numbers, velocity and momentum flux ratios. Several thermocouples were used across the heat exchanger and in other locations to keep track of the conditions of the flow in order to maintain the required flow properties for each test case. Appendix A provides a summary of the operating conditions achieved for all cases reported in the present article. Two images of the shear coaxial injector can be seen in Fig. 3.2. The first, Fig. 3.2(a), gives a full view before assembly and the second, Fig. 3.2(b) shows a plane view of the end section. The inner jet diameter is $d_i = 0.51$ mm. The outer jet has an inner diameter, of 1.59 mm and outer diameter of 2.42 mm. The injector outer diameter was 3.18 mm. The length to inner diameter ratio was 100 for the inner jet and 34 for the outer jet based on the hydraulic diameter. The coaxial injector was installed so that the inner and outer jets were nominally concentric. The inner jet exit plane was recessed by 0.3 mm from the outer jet exit plane. This recess length was chosen to mimic realistic coaxial jet configurations used in practice.

(a) (b)
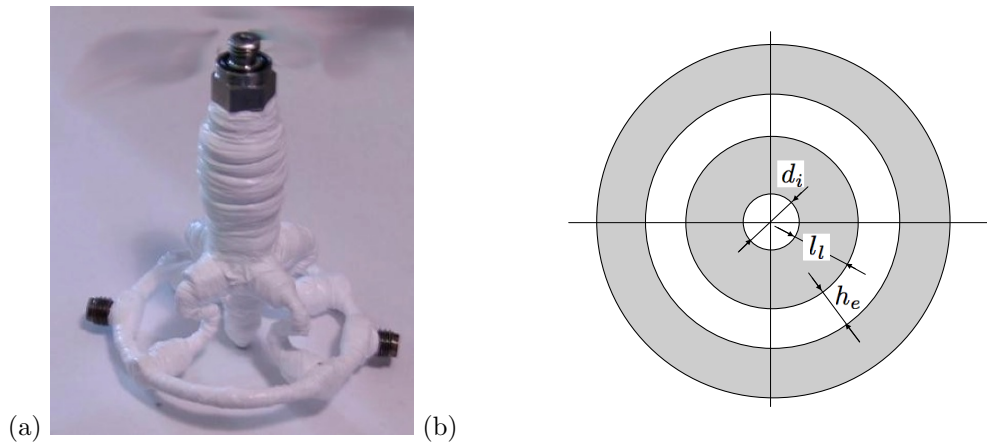
Figure 3.2: (a) Photograph of the shear coaxial injector used in this study. (b) Exit plane view of the injector.

The coaxial injector was placed in an inner chamber within the main test chamber. This unit was protruding into the chamber by 5 mm through a 17 mm in diameter central orifice in the top wall. This inner chamber was created to augment the level of acoustic modulation acting on the coaxial flow. The inner chamber had a height of 6.6 cm, a width of 7.6 cm and a depth of 1.3 cm. The flow was exhausted through another orifice at the center of the bottom wall.

Injection temperatures were measured with unshielded traveling type E thermocouples with a bead diameter of 0.1 mm. The accuracy of the thermocouples used in the study was checked with an RTD and found to be within 1 K. A miniature pressure transducer (Kulite Semiconductor Products, models CCQ-062-1000A and CCQ-093-750A) was placed next to the thermocouple using a small metallic post for support, and recorded pressure fluctuations at a sampling frequency of 20 kHz. These pressure transducers having an absolute pressure range of either 6.9 MPa or 5.2 MPa, respectively were used to used to scan the wavefield induced by the acoustic driver units prior to flow experiments.

The coaxial jet structure was observed with backlighting (shadowgraph) imaging. The flow was illuminated with a light source (Newport variable power arc lamp set at 160W or 300W) and the transmitted light was recorded with a Phantom v7.1 high-speed camera capable of recording up to 160,000 frames per second at a resolution of 32 pixels by 32 pixels. The camera equipped with AF Nikkor 35-105 mm lens and a Nikon No. 1 Close-Up lenscan be seen at the bottom center in Fig. 3.1(a). The image resolution in the present experiments varied from 128 pixels $\times$ 224 pixels to 196 pixels $\times$ 400 pixels, depending on chamber pressure and outer to inner momentum flux ratio. The images were in a grayscale scale with each pixel taking a value between 0 and 255 for different intensities of gray with as extreme values white and black. Each pixel represents an approximate area of 0.08 mm $\times$ 0.08 mm. Depending on the resolution chosen, the framing rate was 20, 25 or 41 kHz. The exposure time was generally 1-2 μs and the number of images saved per run was 1000.

The images recorded were then processed using a Matlab subroutine based on the Otsu technique [44]. The subroutine takes a grayscale image and finds a pixel threshold value. All the pixel values above this threshold are converted to black and the remaining pixels to white. Then the subroutine measures the length of the black region extending from the exit of the coaxial jet. This is referred to as the "dark core length". A "mean dark core length" l_{dc} is then obtained by averaging over the set of images recorded by the camera.

Acoustic modulation of this setup was obtained with two piezo-sirens placed at each end of the chamber at a distance of 34 cm from the jet axis, custom-designed for the Air Force Research Laboratory by Hersh Acoustical Engineering, Inc (the piezo-sirens can be seen at both sides of the chamber in Fig. 3.1(a)). A Fluke 100 MS/s arbitrary waveform generator (model 292) was used to produce two sinusoidal waves with the same frequency but with a prescribed phase between them. The signals were then sent to two amplifiers (Krohn-Hite model 7500 and a Trek model PZD2000A), one for each piezo-siren. The amplified signals were in the 200 to 540 V range. To accommodate for the rectangular chamber, a waveguide with a catenary contour, see upper left corner of Fig. 3.1(a), was used to transmit the waves from the circular cross-section of each siren to a rectangular cross-section. The maximum root-mean-square acoustic pressure fluctuations generated by the two piezo-ceramic acoustic sources in the inner chamber, measured using the three differential Kulite pressure transducers (model XCQ-093-25D) flush mounted on a lateral chamber wall, varied from 8.0 to 22 kPa and were produced in the 2.9 to 3.1 kHz range. These operating conditions were obtained by manually varying the frequency on the signal generator and finding the highest possible pressure amplitude.

The phase difference between the signals sent to the piezo-siren elements was varied to expose the coaxial jet to different effective positions relative to the pressure node or antinode of the acoustic field. When the two piezo-siren elements produce waves with a zero degree phase angle between them, the motion of the piezo-siren radiating membranes is synchronized and in opposite directions. This produces conditions of high pressure perturbations and low velocity fluctuations at the center of the chamber, where the coaxial jet is located which correspond to a pressure antinode or velocity node. In contrast, when the two drivers present a 180-degree phase difference, then the radiating membranes move in the same direction, generating high velocity fluctuations with very small variations in pressure at the jet location producing a pressure node or velocity antinode.

Chapter 4

Balance equations and models

At this stage it is worth briefly reviewing the spatially filtered balance equations and introduce the real gas models and subgrid scale closures used in the large eddy simulations.

4.1 Governing equations

A single species flow configuration is investigated in the present study. In this situation, the vector of conservative variables for a compressible flow is $\boldsymbol{w} = (\rho, \rho\boldsymbol{u}, \rho E)^T$, where ρ is the density, $\boldsymbol{u}$ the velocity vector and E the total energy (E is the sum of internal energy e_s and kinetic energy $e_k = 1/2 \sum u_i^2$). The present large-eddy simulations are carried out by integrating the mass weighted spatially filtered Navier-Stokes equations. In the following balance equations ($\overline{\phi}$ designates a spatially filtered variable while $\tilde{\phi}$ is a mass-weighted (Favre) spatially filtered variable :

$$\frac{\partial \overline{\rho}}{\partial t} + \frac{\partial \overline{\rho}\tilde{u}_j}{\partial x_j} \quad = \quad 0 \tag{4.1}$$

$$\frac{\partial \overline{\rho}\tilde{u}_i}{\partial t} + \frac{\partial \overline{\rho}\tilde{u}_j\tilde{u}_i}{\partial x_j} \quad = \quad -\frac{\partial \overline{p}}{\partial x_i} + \frac{\partial \overline{\tau_{ij}}}{\partial x_j} - \frac{\partial \tau_{ij}^t}{\partial x_j} \tag{4.2}$$

$$\frac{\partial \overline{\rho}\tilde{E}}{\partial t} + \frac{\partial \overline{\rho}\tilde{E}\tilde{u}_j}{\partial x_j} + \frac{\partial \overline{p}\tilde{u}_j}{\partial x_j} \quad = \quad -\frac{\partial \overline{q_j}}{\partial x_j} - \frac{\partial q_j^t}{\partial x_j} + \frac{\partial \tilde{u}_i\overline{\tau_{ij}}}{\partial x_j} \tag{4.3}$$

In Eqs. 4.1-4.3, p is the pressure, $\boldsymbol{x}$ the spatial coordinates vector and t is the time. The laminar viscous stress tensor $\boldsymbol{\tau}$ and heat flux vector $\boldsymbol{q}$ are expressed as linear functions of the strain rates and temperature gradient respectively. Laminar viscosity and heat conductivity coefficients are determined with the Chung *et al.* method [12]. For the single species case investigated in the present article, no additional diffusion terms are needed since the Soret and Dufour effects naturally vanish. The modeling of the subgrid-scale stress tensor τ_{ij}^t and heat flux vector q_j^t requires some discussion. It is known from recent studies that subgrid closure rules for real gases differ from those used for perfect gas flows. In principle one should take into account additional terms arising from the nonlinearity of the state equation, and from the large variations in transport properties as explained in some recent studies by Bellan *et al.* [2], Selle *et al.* [63] and Taskinoglu and Bellan [68]. However the modeling issues are not completely settled. It is also known from other calculations that the low pressure subgrid scale models yield suitable results for transcritical

and supercritical round jets [59, 62]. It was decided for these reasons to keep these low pressure closures for the subgrid scale models as described in more detail in Sec. 4.3.

4.2   Real gas thermodynamics and equation of state

Real gas thermodynamics for high pressure flow calculations is envisaged in many recent studies where accurate descriptions of the fluid state are derived from various types of equations [1, 71]. The present simulations rely on the Peng-Robinson equation of state [45] (Eq. 4.4) which is used in the analysis to model the departure from an ideal-gas behavior. This EOS is less accurate than the modified version but it is also simpler and requires a smaller amount of calculations. The fluid state is expressed in the form :

$$p = \frac{\rho r T}{1 - \rho b} - \frac{\rho^2 a(T)}{1 + 2\rho b - \rho^2 b^2} \tag{4.4}$$

where T is the temperature, $r = R/W$ where R is the perfect-gas constant and W the molar mass. The Peng-Robinson coefficients $a(T)$ and b for a single-species fluid are [47]:

$$a = 0.457236 \frac{(rT_c)^2}{p_c} \left(1 + c(1 - \sqrt{T_R})\right)^2 \tag{4.5}$$

$$b = 0.077796 \frac{rT_c}{p_c} \tag{4.6}$$

with

$$c = 0.37464 + 1.54226\omega - 0.26992\omega^2 \tag{4.7}$$

where $T_c = 126.2$ K and $p_c = 3.396$ MPa are the critical temperature and pressure of nitrogen, $\omega = 0.0372$ represents its acentric factor and $T_R = T/T_c$ is the reduced temperature. This equation offers a good trade-off between computational cost and precision. The pressure dependence of thermodynamic functions and coefficients are subsequently derived from the EOS [33, 38, 71]. Departure energy Δe_s and specific heat Δc_v at constant volume are given by [20, 47]:

$$\Delta e_s = -\int_{\rho}^{\rho_0} \left\{ \frac{T}{\rho^2} \left(\frac{\partial p}{\partial T}\right)_{\rho, Y_k} - \frac{p}{\rho^2} \right\}_T d\rho \tag{4.8}$$

$$\Delta c_v = -T \int_{\rho}^{\rho_0} \left\{ \left(\frac{1}{\rho^2} \frac{\partial^2 p}{\partial T^2}\right)_{\rho, Y_k} \right\}_T d\rho \tag{4.9}$$

where $\Delta e_s = e_s(\rho, T) - e_s^0(T)$ and $\Delta c_v = c_v(\rho, T) - c_v^0(T)$. The enthalpy and specific heat at constant pressure are then deduced from :

$$h_s = e_s + \frac{p}{\rho} \qquad c_p = c_v + \frac{T\alpha^2}{\rho\beta} \tag{4.10}$$

The thermal expansion coefficient α and the isothermal compressibility coefficient β appearing in the previous expressions are given by:

$$\alpha = -\frac{1}{\rho} \left(\frac{\partial \rho}{\partial T}\right)_p \qquad \beta = \frac{1}{\rho} \left(\frac{\partial \rho}{\partial p}\right)_T \tag{4.11}$$

The low-pressure references (i.e. e_s^0 and c_v^0) are obtained from the JANAF Thermodynamical Tables [7], and only depend on temperature.

4.3 Subgrid-scale models and assumptions

As indicated previously, the present simulations rely on a standard (low pressure) subgrid scale closure, the WALE model, in which the stress tensor τ_{ij}^t is conveniently expressed in terms of the spatially resolved strain rates $\widetilde{S}_{ij}$ [35] :

$$\tau_{ij}^t \quad = \quad 2\nu^t \left(\widetilde{S}_{ij} - \frac{1}{3}\delta_{ij}\widetilde{S}_{ll} \right) \tag{4.12}$$

where

$$\nu^t \quad = \quad (C_w\Delta)^2 \frac{(s_{ij}^d s_{ij}^d)^{3/2}}{(\widetilde{S}_{ij}\widetilde{S}_{ij})^{5/2} + (s_{ij}^d s_{ij}^d)^{5/4}} \tag{4.13}$$

$$s_{ij}^d \quad = \quad \frac{1}{2}\left(\widetilde{g}_{ij}^2 + \widetilde{g}_{ji}^2 \right) - \frac{1}{3}\,\widetilde{g}_{kk}^2\,\delta_{ij} \tag{4.14}$$

In the previous expression the WALE model constant $C_w = 0.4929$ and $\widetilde{g}_{ij}$ is the irrotational part of the stress tensor :

$$\widetilde{g}_{ij} = \frac{\partial \widetilde{u}_i}{\partial x_j} \qquad \text{and} \qquad \widetilde{g}_{ij}^2 = \widetilde{g}_{ik}\widetilde{g}_{kj} \tag{4.15}$$

The WALE model distinguishes velocity gradients associated with the rotational and pure shear components of the velocity gradients in order to distinguish regions where turbulence is transitional and regions where it is is fully developed. It is well suited to the treatment of shear flows of the type considered in this article.

The subgrid scale heat flux is modeled using a standard gradient transport assumption :

$$\overline{q_i}^t \quad = \quad -\lambda_t \frac{\partial \widetilde{T}}{\partial x_i} \tag{4.16}$$

The subgrid scale conductivity is cast in the form $\lambda_t = c_p\mu_t/\mathrm{Pr}_t$ where $\mu_t = \rho\nu_t$ and Pr_t respectively designate the subgrid dynamic viscosity and turbulent Prandtl number. As in low pressure simulations a constant value $\mathrm{Pr}_t = 0.7$ is used in the present calculations.

Chapter 5

Numerical aspects

The mass weighted spatially filtered compressible Navier-Stokes equations in combination with the subgrid scale models described previously are integrated in the AVBP flow solver [60, 34]. This code has already been used to calculate low and moderate pressure reactive flows of multicomponent mixtures of perfect gases. The spatial discretization on unstructured or hybrid meshes facilitates applications in which the geometry is complex, a feature which is quite useful if one wishes to analyze practical configurations. The LES of turbulent flows requires a low-dissipation algorithm [21, 18] which is often obtained with centered discretization schemes. The present integration method relies on a Taylor-Galerkin weighted residual central distribution scheme, called TTG4A. This scheme is third-order in space and fourth-order in time [50].

The real gas equation of state, thermodynamics and transport coefficients have been implemented in AVBP. The convective fluxes Jacobian matrices, used by the scheme, are expressed in terms of real gas thermodynamics to preserve the overall consistency of the code. A fully consistent treatment of associated boundary conditions is based on the characteristic wave decomposition method NSCBC [46, 34] and includes specific expressions provided for real gas thermodynamics in[39]. The highly nonlinear thermodynamics of the transcritical fluid stream induces large density gradients between the dense transcritical fluid and the surrounding gaseous stream which require a specific stabilization procedure. This relies on artificial viscosity and is used when unresolved gradients are detected following a method described in [59]. The real gas AVBP flow solver has already been used to simulate transcritical cryogenic flames of various types [48, 58, 57].

5.1   Computational domain and mesh

The geometry of the computational domain essentially matches the experimental configuration. A three dimensional view of the external boundaries is given in Fig. 5.1(a). The longitudinal section of the chamber is rectangular (59.4×76.0 mm) and its width is 12.7 mm. The fluid streams are injected by a coaxial element which protrudes by 5 mm into the chamber (Fig. 5.1b). This injector is located in the center of a 17 mm-diameter hole in the inlet wall. No co-flow is directly injected through this orifice during the experiment but nitrogen gas may traverse this aperture as a result of entrainment by the coaxial streams giving rise to a finite flow velocity in this region. The entrained fluid originates from a large reservoir defined on the upstream side of the central hole. Details about the injector geometry

are given in Fig. 5.2(a). The inner injector diameter, inner duct thickness, annular duct thickness and outer duct diameter are respectively $d_i = 0.51$ mm, $l_l = 0.54$ mm, $h_e = 0.415$ mm and $d_o = 2.42$ mm. The mesh comprises 2 100 000 nodes corresponding to 10 000 000 tetrahedra. It is highly refined near
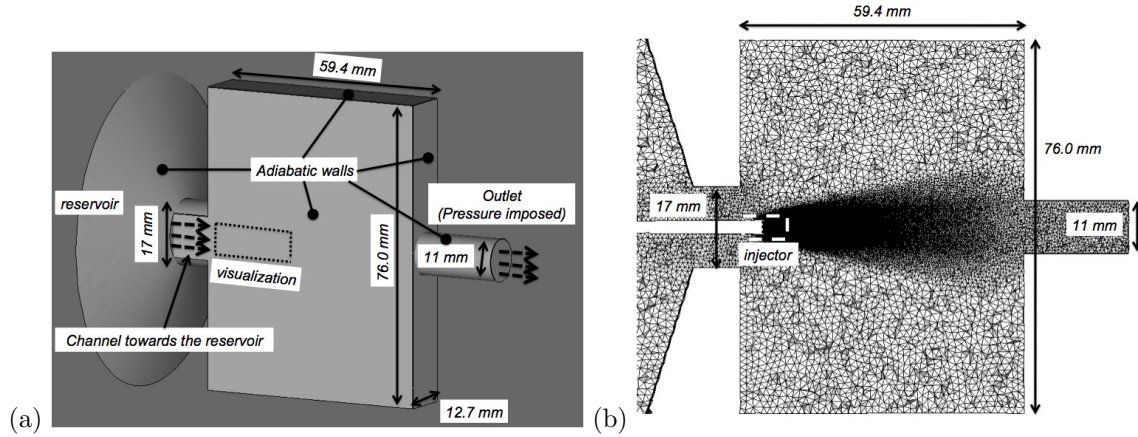
Figure 5.1: (a) Three-dimensional visualization of the reservoir. (b) Longitudinal cut of the mesh.

the injector (Fig. 5.2(b)), with a constant characteristic size of 0.032 mm on a distance of 10 inner jet diameters. The mesh is then slowly coarsened towards the domain outlet (Fig. 5.1(b)).
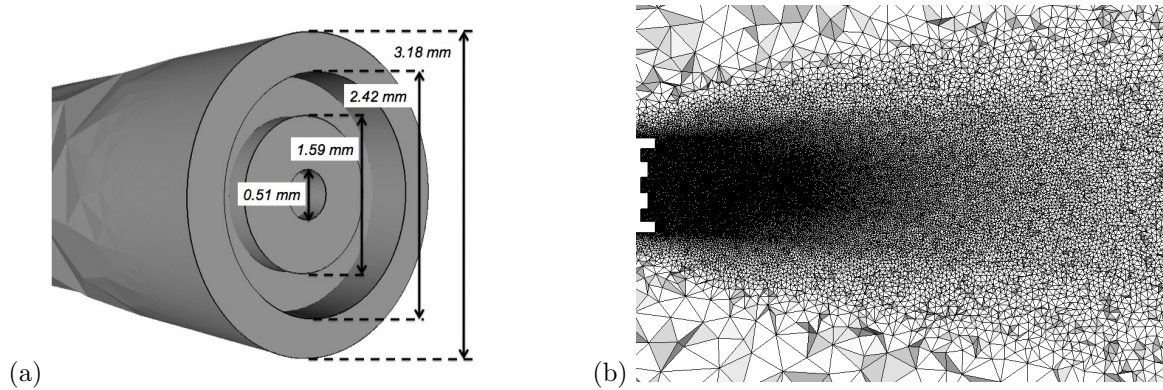
Figure 5.2: (a) Closer view of the injector. (b) Longitudinal cut of the mesh (35 inner injector diameters).

5.2   Injection characteristics and boundary conditions

Three test conditions are considered in this analysis designated as "N2","N6" and "N8". Case "N6" serves as a reference simulation. The two other cases, designated as "N2" and "N8", are also calculated in order to analyze effects of the momentum flux ratio on the flow behavior (Ch. 6). The three cases differ by their injection temperatures and velocities, yielding momentum flux ratios J of 1, 2.6 and 9.1 for cases "N2", "N6" and "N8" respectively. The corresponding density ratios S are 5.84, 5.74 and 3.22

respectively. Injection conditions are gathered in Tab. 3.1 and Tab. 3.2 which respectively correspond to the outer and inner streams. Injection conditions are placed on thermodynamic plots on Fig. 5.3. The density and volumetric internal energy notably depart from a perfect gas behavior when temperature is close and below the critical value. The influence of acoustic perturbations will only be investigated in a single case corresponding to "N6" (Ch. 7).

In all cases, pressure is maintained at the outlet boundary using non-reflecting characteristic conditions at an adapted level of 3.56 MPa and the chamber and reservoir are initially filled with nitrogen at the same pressure and a temperature 213 K (the corresponding density is 59.6 $kg\ m^{-3}$). All solid boundaries are treated as adiabatic slip walls. Velocity perturbations (with an amplitude of 3 % of the mean flow) are added at injection in order to represent effects of turbulent fluctuations using a procedure described in [6, 66, 17].

(a)   (b)
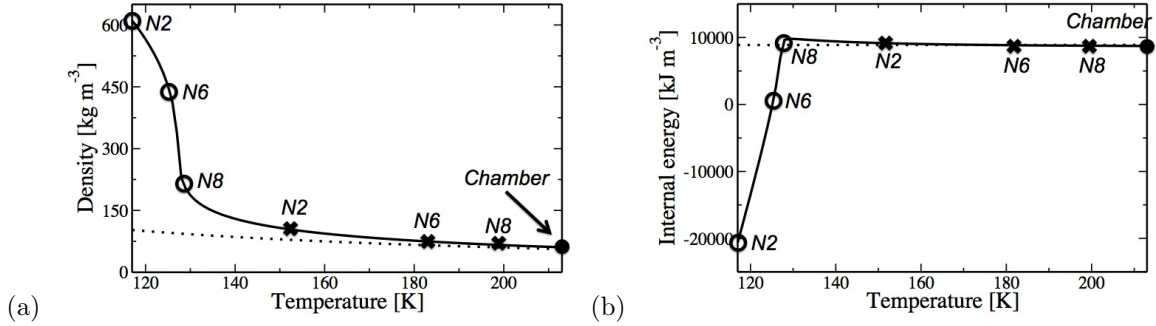
Figure 5.3: Thermodynamic state calculated with the PR EOS (—) and the perfect gas EOS (· · ·). (a) Density in terms of temperature. (b) Volumetric internal energy (*i.e.* ρe_s) in terms of temperature. The pressure is constant and equal to 3.56 MPa. Symbols: ∘ inner jet conditions; × outer stream conditions; • chamber conditions.

Case	$J = (\rho_e u_e^2)/(\rho_i u_i^2)$	$M = (\rho_e u_e)/(\rho_i u_i)$	$S = \rho_i/\rho_e$	$U = u_e/u_i$
N2	1.05	0.42	5.86	2.48
N6	3.05	0.72	5.65	4.15
N8	9.3	1.70	3.22	5.48

Table 5.1: Injection characteristics of the simulated cases. J is the momentum flux ratio between the outer and the inner jets, M the mass flux ratio, S the density ratio and U is the velocity ratio. ρ_i, ρ_e, u_i and u_e are the inner and outer jet densities and velocities.

5.3   Simulation procedure

Simulations are carried out on a coarse mesh, with an initial solution corresponding to a uniform fluid at rest. The flow is then qualitatively established after three convective periods. Results are then interpolated on the final mesh. Data averaging can be started after one transient period. The simulated physical time is given in Tab. 5.2 together with the number of simulated convective periods. Finally, the CPU time (equal to the product $n_{core} \times n_{hours}$) needed to obtain the average solution (which does not

include the CPU time needed for the transient flow and the simulation on the coarse mesh) is also given in this table.

Case	Δt^a [ms]	$\Delta t^a/\tau_{u_i}$	$\Delta t^a/\tau_{u_e}$	CPU time [h]
N2	14.3	1.9	4.8	35 000
N6	22.7	4.4	18.2	45 000
N8	10.4	4.0	21.2	20 000

Table 5.2: Averaging time for cases "N2", "N6" and "N8". Δt^a is the physical averaging time. τ_{u_i} represents one convective time over 35 d_i for the inner jet and τ_{u_e} represents one convective time over 35 d_i for the outer jet. $\tau_{u_i} = (35d_i)/u_i$; $\tau_{u_e} = (35d_i)/u_e$.

Chapter 6

Effect of momentum flux ratio

It is first natural to consider the influence of the momentum flux ratio on the system behavior. Flow patterns calculated numerically and obtained experimentally are first compared in Sec. 6.1. This is followed by a description of the mean flow in Sec. 6.2 and by an analysis of flow dynamics in Sec. 6.3.

6.1   Instantaneous flow patterns

Instantaneous backlighting images obtained experimentally are shown in Fig. 6.1(a),(c),(e). In the dark core light is deviated by changes in the refraction index. This in turn delineates regions where the density takes large values (the deviation can be roughly linked to the second derivative of the density integrated on the line of sight). It is generally admitted that the dark region represents the position of the dense core, and qualitatively highlights its external boundaries giving an insight on the main structures present in the flow [43]. As the momentum flux ratio is increased, the inner jet axial length is reduced. Case "N2" exhibits large scale structures over about 10 inner injector diameters downstream of the injector. These structures are not identifiable in cases "N6" and "N8". The latter is characterized by a sudden termination of the inner jet at a few inner jet diameters from the exit plane. In contrast with cases "N2" and "N6", the inner stream appears to be quickly mixed with the surrounding fluid and the central jet can no longer be clearly identified downstream of this abrupt termination.

Longitudinal slices of instantaneous density distributions extracted from simulations are shown in Fig. 6.1(b),(d),(f) which respectively correspond to "N2", "N6" and "N8" cases. Comparisons between these figures and the experimental backlighting images are admittedly qualitative. Nevertheless, general experimental features corresponding to these different cases are replicated. One finds that case "N2" features large scale structures which are not present in cases "N6" and "N8". The abrupt termination noticed in case "N8" is retrieved numerically. This is also made more apparent in the density iso-surfaces corresponding to $\rho = 0.1(\rho_i - \rho_e) + \rho_e)$ plotted in Fig. 6.2. The large scale structures observed experimentally characterize case "N2", and disappear as the momentum flux ratio is increased (cases "N6" and "N8").

(a)

(b)

(c)

(d)

(e)

(f)
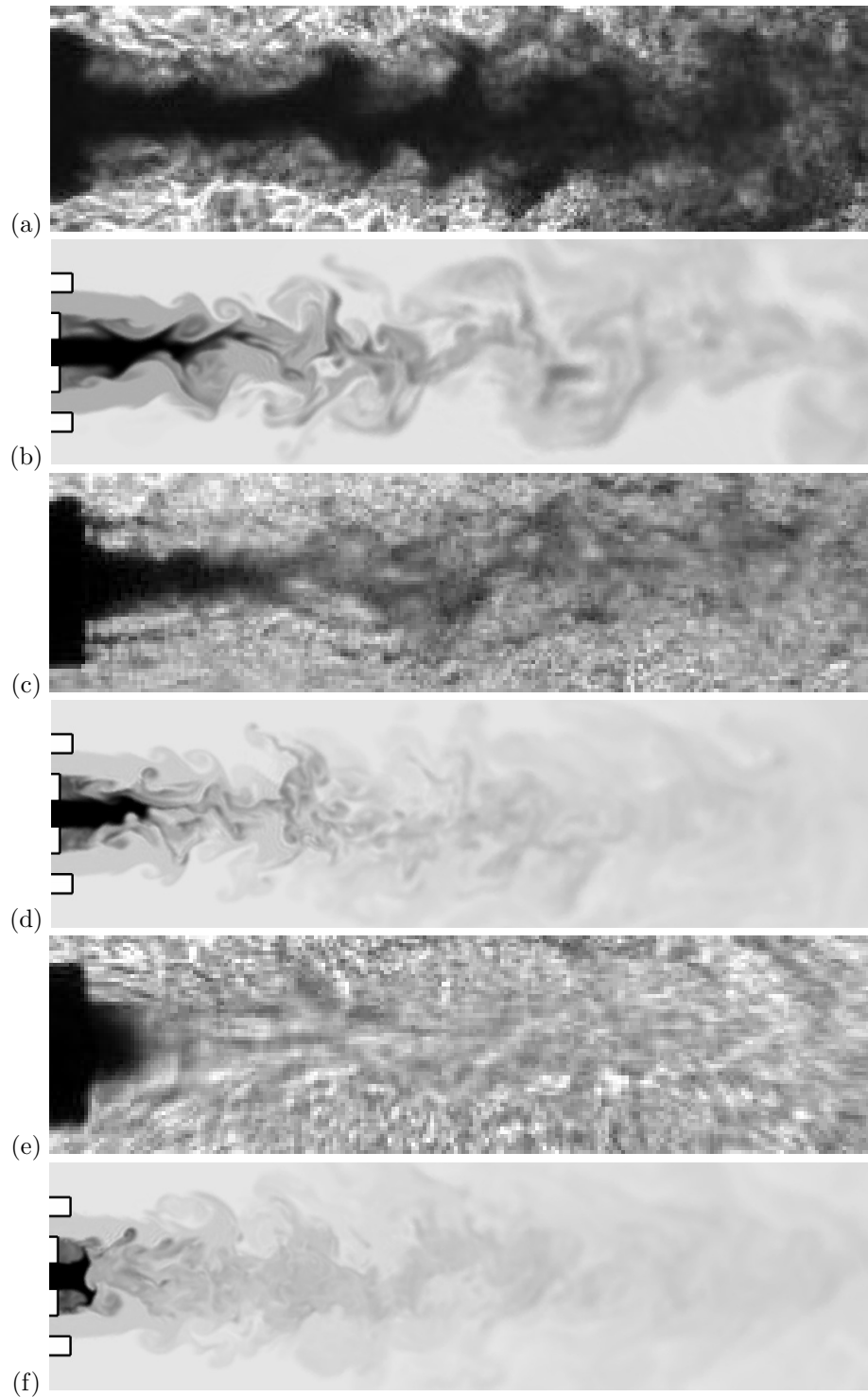
Figure 6.1: Comparison between experimental visualizations (backlighting) and typical instantaneous density distributions obtained from simulations (white: $60 \, \text{kg} \, \text{m}^{-3}$; black: inner jet injection density (Tab. 3.2) ; logarithmic scale). *Case "N2" (J=1.05)* : (a) Experimental backlighting image, (b) Calculated density. *Case "N6" (J=3.05)* : (c) Experimental backlighting image, (d) Calculated density. *Case "N8" (J=9.3)* : (e) Experimental backlighting image, (f) Calculated density.
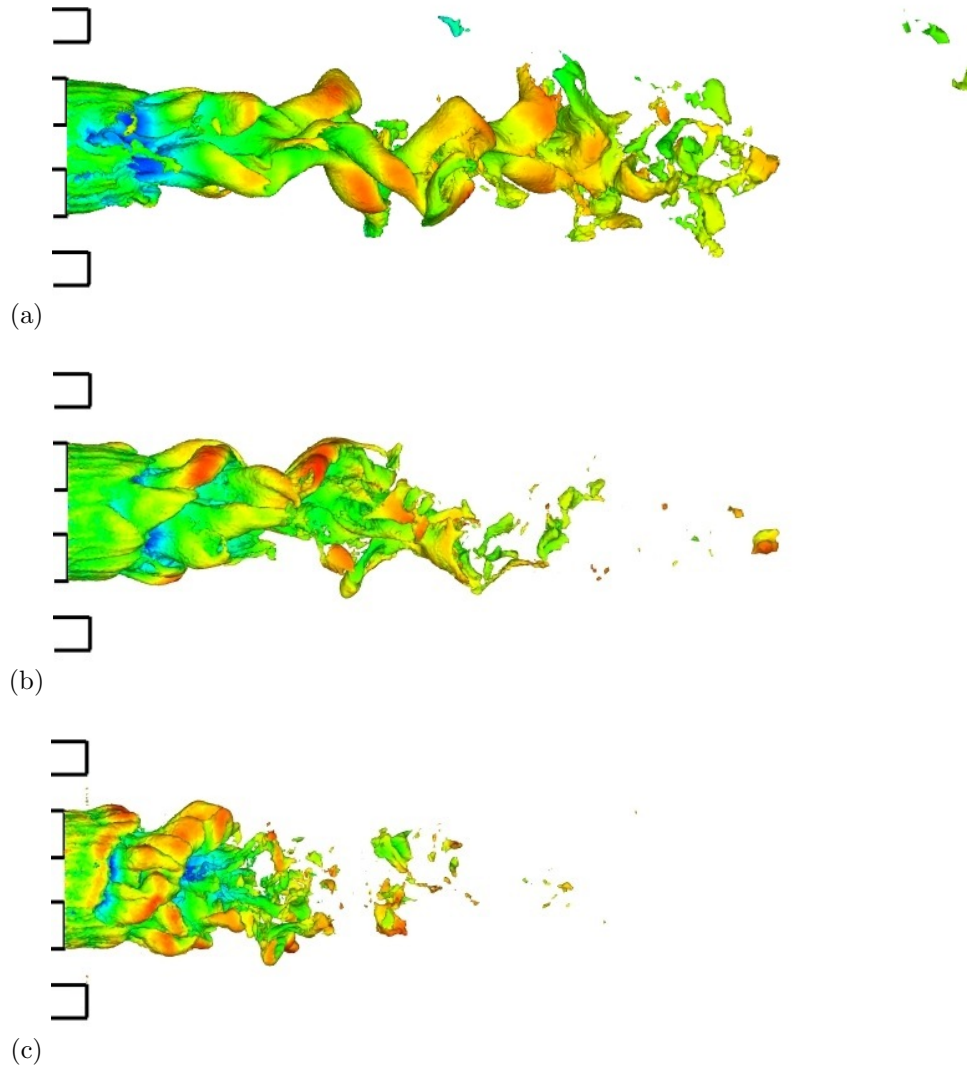
Figure 6.2: *LES results.* Density iso-surface corresponding to $\rho = 0.1(\rho_i - \rho_e) + \rho_e$ colored by the axial velocity. (a) *case "N2" (J=1.05)* u_{min}=-2 m s^{-2}, u_{max}=6.5 m s^{-2}, (b) *case "N6" (J=3.05)* u_{min}=-4 m s^{-2}, u_{max}=16 m s^{-2}, (c) *case "N8" (J=9.3)* u_{min}=-5 m s^{-2}, u_{max}=40 m s^{-2}. The plot corresponds to 20 inner injector diameters.

6.2 Mean flow description

It is first interesting to examine effects of the momentum flux ratio on the mean "dark core" length. Since the density field cannot be directly compared to the experimental light distribution images, it is natural to define a set of density length scales and compare them with the dark core length deduced from the data. The jet core characteristic lengths are defined by considering the axial density distribution :

$$l_\rho^{0.99} = x_\rho^{0.99} - x_0 \qquad l_\rho^{0.5} = x_\rho^{0.5} - x_0 \qquad l_\rho^{0.1} = x_\rho^{0.1} - x_0 \tag{6.1}$$

where x_0 is the axial position of the inner injector exit, $x_\rho^{0.99}$, $x_\rho^{0.5}$ and $x_\rho^{0.1}$ are positions on the jet axis where density is respectively equal to 99 % of its initial value, to $0.5(\rho_i - \rho_e) + \rho_e$ or to $0.1(\rho_i - \rho_e) + \rho_e$. These three lengths are shown in Fig. 6.3(a) together with mean density profiles on the centerline.

It is also useful to define at this point another length scale based on the axial mean velocity profile. The central jets all feature an initial decrease in the axial velocity on the centerline as can be seen in Fig. 6.3(b). The minimum value is reached at x_u which is used to define a new length scale $l_u = x_u - x_0$.

Characteristic lengths are gathered in Tab. 6.1 for comparison with experimental measurements of the "dark core" length. The latter values are deduced from backlighting images by measuring the "dark region" size from average images. Again, comparison between experiment and simulation is limited. As already noted in [43], lengths deduced from experimental backlighting data are generally larger than those deduced from density measurements. It is however clear that there are similarities between trends in simulations and experiments. In agreement with experiments, numerical results indicate a reduction in the density length scales as the momentum flux ratio is increased. The velocity length scale is reduced and the amplitude of the velocity defect is enhanced as the momentum flux ratio is increased. The flow
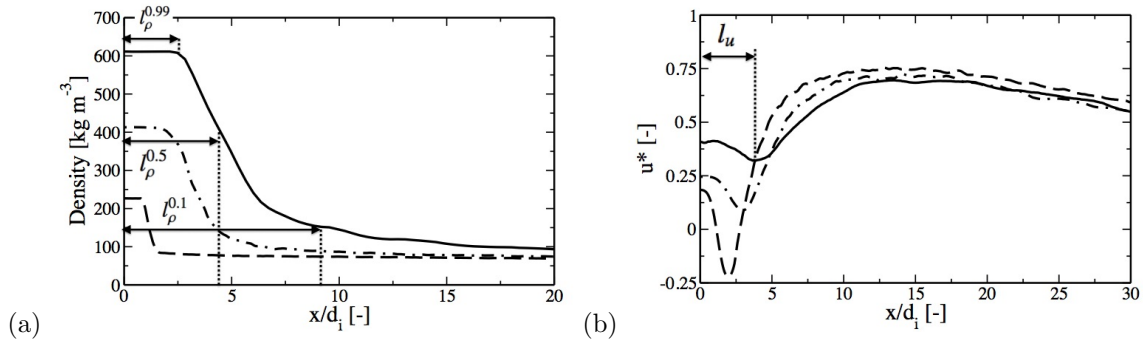
Figure 6.3: Centerline profiles deduced by averaging LES results. (a) Density, (b) Axial velocity normalized by the outer injection velocity $u^* = u/u_e$. —— : Case "N2", — · — : Case "N6" and − − : Case "N8".

may also be characterized by the distributions of mean axial velocity plotted in Fig. 6.4. The outer flow contracts towards the central stream and pinches the central jet to a point where this stream disappears. In the three cases, a small back-flow is generated behind the injector lips. As the momentum flux ratio is increased beyond a certain critical value (case "N8"), the central jet is surrounded by a negative axial velocity region (Fig. 6.4c).

Case "N8" exhibits a large negative value, as observed previously in Fig. 6.4(c). Further downstream, the flows behave in a self-similar fashion in terms of axial velocity normalized by the outer jet injection velocity. Beyond this section, the impact of the inner jet on the flow disappears as this jet is mixed with

Case	$l_\rho^{0.99}/d_i$	$l_\rho^{0.5}/d_i$	$l_\rho^{0.1}/d_i$	l_u/d_i	l_{dc}/d_i
N2	2.57	4.40	8.66	3.8	15.5
N6	1.81	3.37	5.88	2.95	6.0
N8	0.85	1.17	1.67	1.96	2.5

Table 6.1: Characteristic lengths deduced from simulations based on axial density and velocity profiles and from experimental measurement of the dark core size.
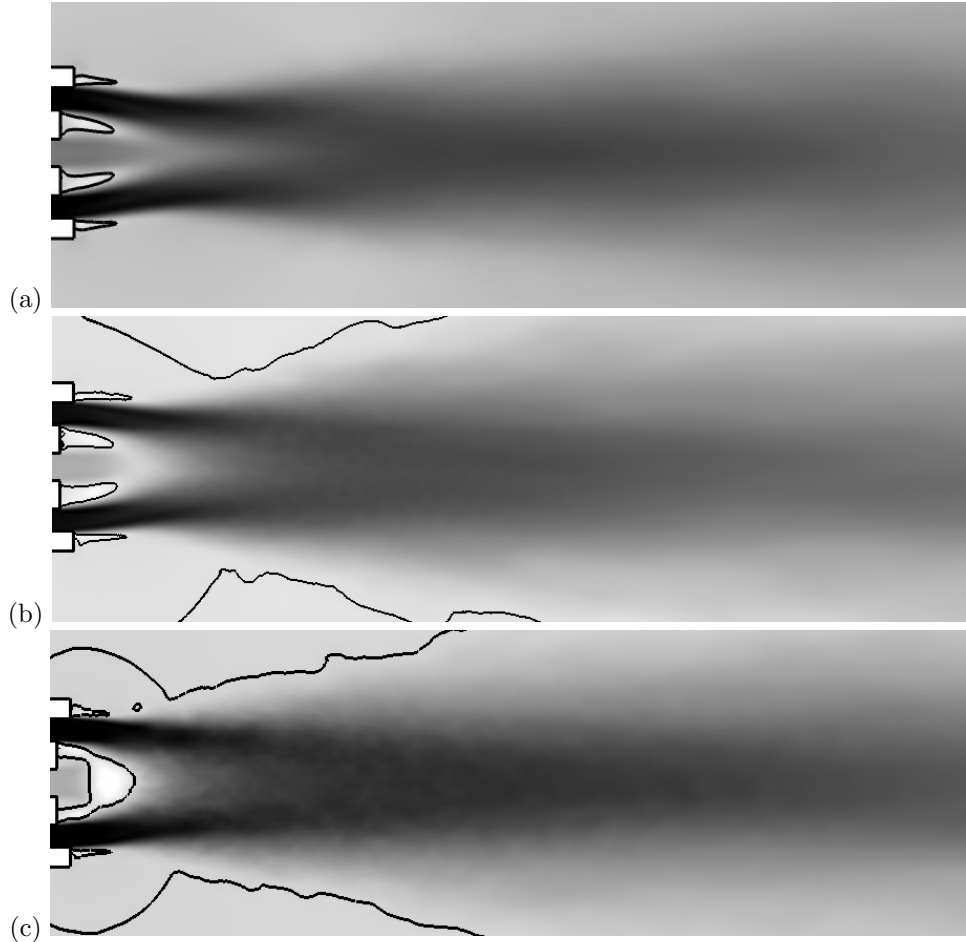
Figure 6.4: Distribution of axial velocity (white: minimum ; black: maximum). This map corresponds to 35 inner injector diameters. − iso-contour of zero axial velocity. (a) *case "N2" (J=1.05)*, (b) *case "N6" (J=3.05)*, (c) *case "N8" (J=9.3)*.

the outer stream. Since the mass flow rate of the outer jet is much higher than that of the inner jet, the outer jet dominates the flow. Interestingly, the three profiles merge at $x > 15d_i$, indicating a self-similar behavior when profiles are plotted in terms of normalized variables.

Radial profiles of normalized density and axial velocity are plotted in Fig. 6.5 for case "N6" (case "N2" is not shown here because its behavior is quite similar). The first profiles lie in the potential core region $(x < x_\rho^{0.99})$, and feature constant levels of density and velocity in that region. Negative values of axial velocity indicate that back-flow is generated behind the lips. The density profile behind the inner lip shows a rapid variation towards the outer stream. This is attributed to an efficient mixing of inner and outer streams associated with the formation of vortical structure behind the inner lip and the generation of a back flow. In this region, mass is extracted from the central jet by vortical structures and recirculates upstream. Dynamics in this region is discussed in Sec. 6.3. The profile at $3d_i$ corresponds to $x = x_u$. The density stratification is still apparent. At $x = 15d_i$, velocity and density are maximum on the centerline, and a jet-like profile is retrieved. Further downstream, the flow behaves like a single round jet and develops in a self-similar fashion. The half width at half maximum (HWHM) of density L_ρ is plotted in Fig. 6.6(a). For $x > 20d_i$, this quantity evolves quasi-linearly $L_\rho = E_\rho^H(x - x_v)$, where E_ρ^H is the spreading rate of the jet and x_v is a virtual origin. Linear regressions for $20d_i < x < 35d_i$ give spreading rates of 0.12, 0.11 and 0.11 for cases "N2", "N6" and "N8", respectively. These values are in agreement with those given for example by Chen and Rodi [10] for a single jet and with results obtained from previous high pressure simulations of single species round jets [59, 76]. In this region of the flow the density profile takes a gaussian shape (Fig. 6.6b). A linear evolution of the density decay is also observed, but not shown here, confirming that the flow is self-similar in the downstream region. Since
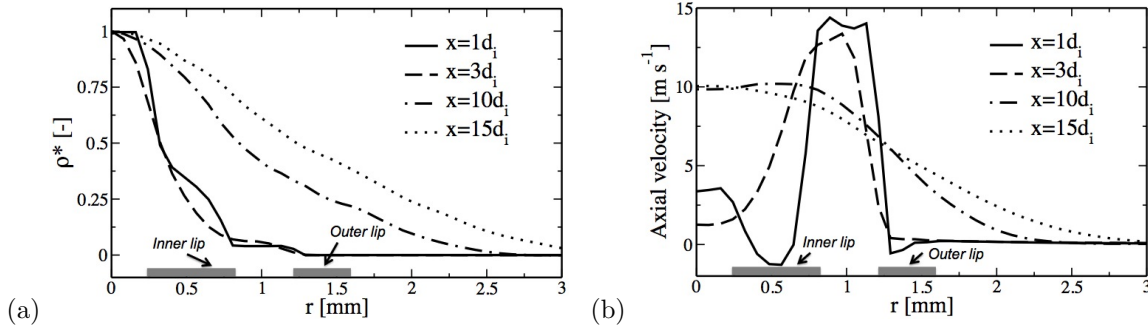
Figure 6.5: *LES results*, Case "N6". (a) Radial profiles of normalized density $\rho^* = (\rho - \rho_\infty)/(\rho_c - \rho_\infty)$ (b) Radial profiles of axial velocity.

the flow develops in a confined domain one may wonder if it is influenced by recirculation in the chamber. Examination of velocity distributions in the domain indicates that the outer recirculation velocities are low and that the reverse flow in the outer region has a limited influence on the coaxial jet structure.

6.3 Near injector flow dynamics

Large eddy simulations allow detailed analysis of the flow dynamics. This can be accomplished by estimating the spectral content of fluctuations in various regions of the flow to identify the preferred modes of the system. To this end, it is convenient to place a set of sensors in the flow and examine the corresponding velocity and density time series. This is illustrated in Fig. 6.7. Since the general flow
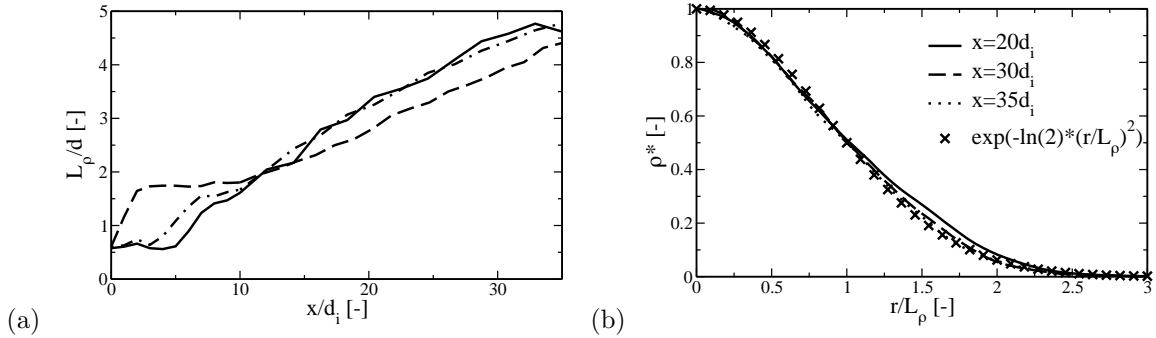
Figure 6.6: *LES results* (a) Half Width Half Max of density — Case "N2", $- \cdot -$ Case "N6" and $- -$ Case "N8". (b) Radial profiles of normalized density $\rho' = (\rho - \rho_\infty)/(\rho_c - \rho_\infty)$.

structures of cases "N2" and "N6" differ from that corresponding to "N8", it is natural to study these two cases separately (Sec. 6.3.1). Case "N8" is then considered in Sec. 6.3.2.
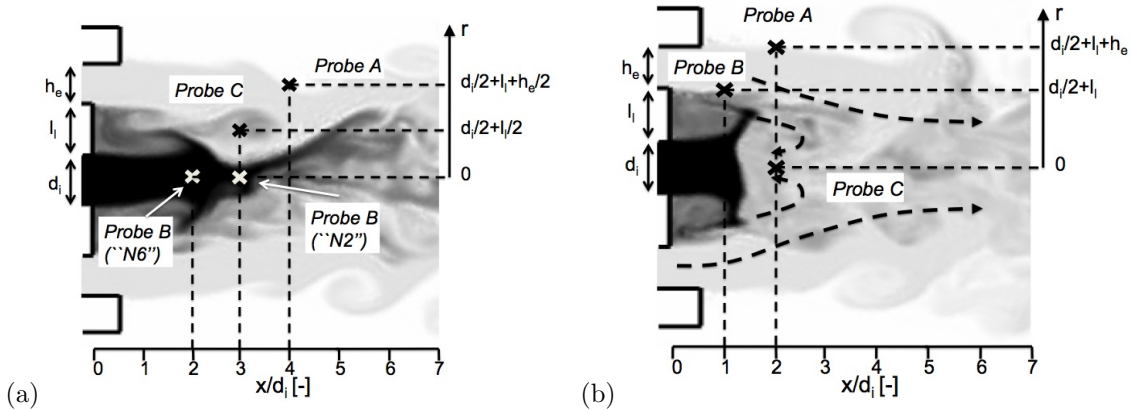
Figure 6.7: The three sensor locations. The numerical probes are used to measure characteristic frequencies in the coaxial flow. (a) Case "N6" (J=3.05). Density distribution (white: 60 kg m^{-3} ; black: 410 kg m^{-3} ; logarithmic scale). Sensor B is placed at the end of the inner jet potential core which corresponds to different location in cases "N2" and "N6". (b) Case "N8" ($J = 9.3$). Density distribution (white: 60 kg m^{-3} ; black: maximum ; logarithmic scale). Sensor C is located in the recirculation region.

6.3.1   Cases "N2" and "N6"

To examine the spectral information it is natural to define a set of Strouhal numbers associated with characteristic scales and velocities in the region of interest. The meaningful length scales in this study are the inner injector diameter d_i, the inner lip thickness l_l and the annular jet thickness h_e. Two velocities characterize the system : the inner and outer jet injection velocities (u_i and u_e, respectively). The resulting Strouhal numbers and the probes used to measure frequencies are shown in Tab. 6.2. Probes A and B are used to evaluate the fundamental frequencies of the outer and inner streams. Probe C

provides the dominant frequency associated with eddy structures released behind the injector lip and associated with the outer jet. From instantaneous snapshots (see Fig. 6.7 for example) and animations, these structures are found to originate from the lip corner on the outer-jet side. Positions of the different probes are shown in Fig. 6.7 (a). Note that the axial location of probe B is not the same in cases "N2" and "N6", because this probe is placed at the end of the potential core. Power spectral densities are estimated using Welch's method of periodograms. Statistical averaging is obtained by segmenting the finite data set in M overlapping blocks (a 50 % overlap is used to augment the number of periodograms used in the averaging procedure). Because the number of samples is limited the averaging is carried out over $M = 8$ blocks in the outer flow and on $M = 4$ blocks in the inner jet (power is concentrated in the low frequency range and it is important to augment the resolution to distinguish the maximum frequency). The frequency resolution corresponding to the different sensors is given in Tab. 6.2.

$St = (fl)/u$	l	u	Probe (Fig. 6.7(a))	Δf [Hz]
St^e	h_e (0.41 mm)	u_e	A	N2: 375 ; N6: 250
St^i	d_i (0.51 mm)	u_i	B	N2: 187 ; N6: 125
St^l	l_l (0.54 mm)	u_e	C	N2: 375 ; N6: 250

Table 6.2: Definition of characteristic Strouhal numbers. The characteristic length and velocity l and u are given in the second and third columns. The frequency f corresponds to the power spectral density maximum estimated from the simulations. Δf is the frequency resolution.

The outer and central streams are destabilized at a few diameters d_i from the injector exit. The measured frequency for the outer jet (probe A) is 3 600 Hz for case "N2" and 8 550 Hz for case "N6" (Fig. 6.8), which correspond to St^e_{N2}=0.25 and St^e_{N6}=0.25. The central high-density jet presents a fundamental instability at 1 620 Hz and 1 740 Hz for cases "N2" and "N6" (Fig. 6.9) respectively (probe B). The associated Strouhal numbers are then St^i_{N2}=0.34 and St^i_{N6}=0.26. For both cases, the fundamental mode of the inner and outer streams fall in the typical range for round jets (0.2 - 0.4).
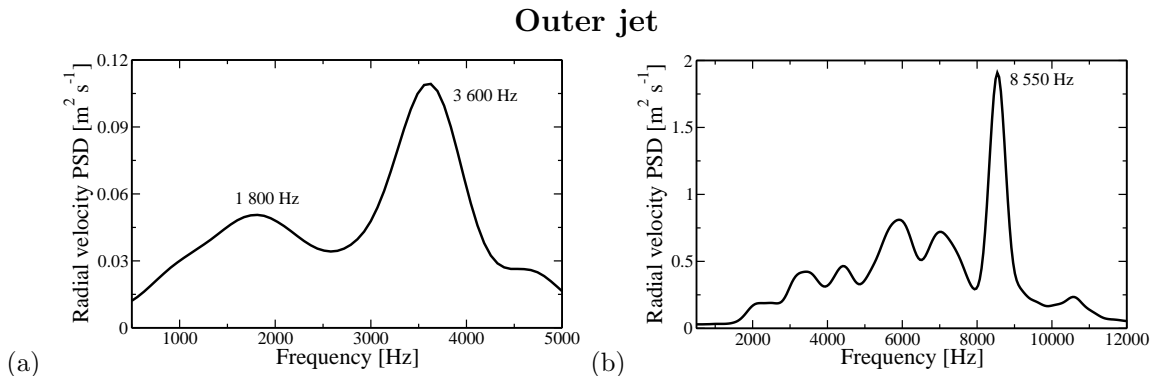
Figure 6.8: Power spectral density of the radial velocity in the outer jet (probe A). Averaging is carried out on $M = 8$ blocks with a 50% overlap. (a) Cases "N2" (J=1.05), (b) Case "N6" (J=3.05).

The mixing layer between the two jets features eddy structures generated downstream of the central lip. Their dynamics is similar to that observed for vortices shed behind a backward-facing step. The characteristic frequencies are found to be 1 620 Hz and 3600 Hz, for cases "N2" and "N6" (Fig. 6.10),

Inner jet
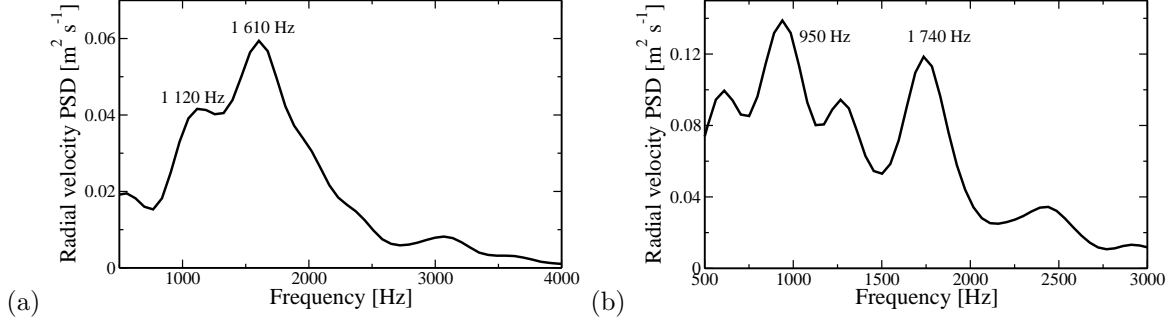
Figure 6.9: Power spectral density of radial velocity in the inner jet (probe B). Averaging is carried out on $M = 4$ blocks with a 50% overlap. (a) Cases "N2" (J=1.05), (b) Case "N6" (J=3.05).

respectively. Such frequencies correspond to Strouhal numbers St^l_{N2}=0.15 and St^l_{N6}=0.23 for cases "N2" and "N6" which are slightly higher than the commonly determined values for backward-facing step instabilities (St=O(0.1) [70]). This could be attributed to a reduction of the "effective" lip thickness as shear is increased. It turns out that the backward-facing step vortical structures induce a back-flow behind the lip (Fig. 6.4). High density fluid from the central jet is entrained and recirculates behind the lip. One may then consider that this results in a reduced "effective" lip thickness which intervenes in the formation of the vortical structures, thus limiting their spatial development and increasing the instability frequency. All the Strouhal numbers obtained are gathered in Tab. 6.3. The frequency obtained for case "N2" is interestingly close to that associated with the inner jet preferred mode. This observation may explain why large scale structures are exclusively observed in this case (Fig. 6.1).

Inner lip
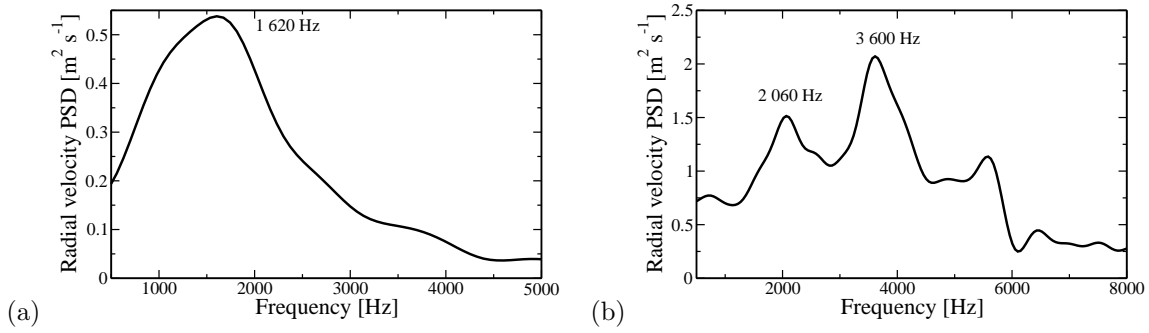
Figure 6.10: Power spectral density of radial velocity in the mixing layer behind the inner lip (probe C). Averaging is carried out over $M = 8$ blocks with a 50% overlap. (a) Cases "N2" (J=1.05), (b) Case "N6" (J=3.05).

Case	St^e (probe A)	St^i (probe B)	St^l (probe C)
N2	0.25	0.34	0.15
N6	0.25	0.26	0.23

Table 6.3: Characteristic Strouhal numbers obtained from the simulations for cases "N2" and "N6".

6.3.2   Case "N8": recirculation regime

The mechanism leading to mixing of the high density jet with the outer stream is somewhat different for case "N8". It is already known that the dense jet ends abruptly and that a recirculation bubble is established beyond that point. As done previously for cases "N2" and "N6", characteristic length scales used to define the relevant Strouhal numbers are given in Tab. 6.4 and the probes used to characterize this case are shown in Fig. 6.7(b). Probe C is inside the recirculation region and is located at $x = x_u$. This case is highly turbulent and features a broadband spectrum so that temporal data are arranged in $M = 16$ blocks to ensure a reasonable statistical convergence. A 50 % overlap is used to obtain the maximum possible averaging number. The resulting frequency resolution is in this case 1 000 Hz. This value may seem quite high, but should be compared to the spectral range which extends to 25 000 Hz.

$St = (fl)/u$	l	u	probe (Fig. 6.7(b))
St^e_{N8}	h_e (0.41 mm)	u_e	A
St^l_{N8}	l_l (0.54 mm)	u_e	B
St^b_{N8}	$d_i + l_l$ (0.51+0.54 mm)	u_e	C

Table 6.4: Strouhal numbers definitions. l and u are the characteristic length and velocity used to define the Strouhal numbers. f represents the frequency obtained from the simulations and Δf is the frequency resolution.

The dominant frequency for the outer jet (probe A) is 21 600 Hz (Fig. 6.11), which corresponds to St^e_{N8}=0.25, as also obtained for the two other cases. The inner jet is notably affected by the recirculation bubble. Its longitudinal development is limited and mass is ejected in the radial direction in the form of thin layers appearing in Fig. 6.7(b). The resulting structure is similar to a counterflow. This motion leads to the formation of a recirculation ring of high density fluid behind the inner lip with a characteristic size of the order of the lip thickness. Vortex roll-up is observed behind the inner lip, in the mixing layer established between the inner and outer jets. These structures are similar to those observed in cases "N2" and "N6", but they strongly interact with higher density layers emerging from the central jet and their spatial development is limited by the recirculation region. The corresponding Strouhal number is St^l_{N8}=0.26 (Fig. 6.12(a)). These eddy structures lead to the formation of the recirculation region. The measured frequency corresponds to St^b_{N8}=0.18 (Fig. 6.12(b)). The dynamics of this bubble is similar to that observed behind a bluff body terminated by a flat face, for which the characteristic Strouhal number is close to 0.2. The Strouhal numbers obtained in this analysis are gathered in Tab. 6.5.

St^e_{N8} (probe A)	St^l_{N8} (probe B)	St^b_{N8} (probe C)
0.25	0.26	0.18

Table 6.5: Characteristic Strouhal numbers obtained from the simulations for case "N8".
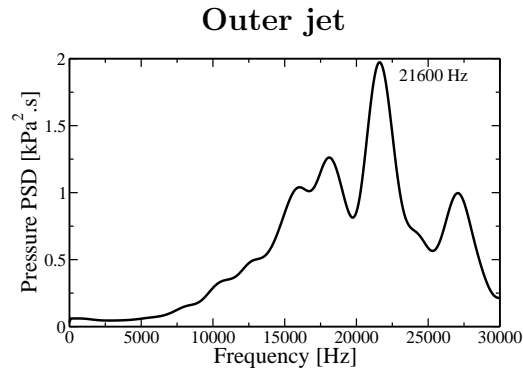
Figure 6.11: Case "N8" (J=9.3). Power spectral density of pressure on Probe A. Averaging is carried out over $M = 16$ blocks with 50% overlap.
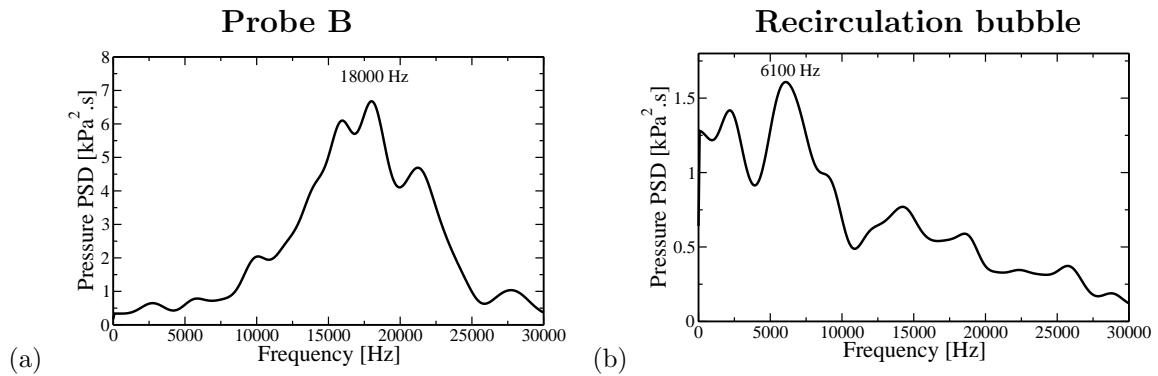
Figure 6.12: Case "N8" (J=9.3). (a) Power spectral density of pressure on Probe B, (b) Power spectral density of pressure in the recirculation bubble. Averaging is carried out over $M = 16$ blocks with 50% overlap.

Chapter 7

Effects of transverse acoustic modulation

Effects of an acoustic modulation are now investigated in case "N6". This operating point is chosen because the core is sufficient long to allow an examination of external modulation effects. The methodology used to impose an acoustic excitation is described in Sec. 7.1. Results are then compared with experimental observations in Sec. 7.2 and discussed in Sec. 7.3.

7.1 Modulation methodology

An acoustic modulation is obtained by imposing harmonic modulations of the normal velocity at the outer boundaries using a method devised by Rey *et al.* [52] (Fig. 7.1). The modulation has the form :

$$v_1 = \sin(2\pi f t) \qquad v_2 = \sin(2\pi f t + \phi) \tag{7.1}$$

where v_1 and v_2 are the normal velocities at the lateral boundaries, f is the modulation frequency set equal to 3 000 Hz, ϕ designates the phase between the imposed modulations. All other boundaries are treated as in the previous cases (in the absence of modulation). This technique is first validated by simulating an acoustic perturbation in the absence of the central flow. Longitudinal distributions of the rms pressure fluctuations are shown in Fig. 7.2. When $\phi = 0$ (Fig. 7.2(a)), the normal velocities at the boundaries are in phase and this yields a maximum pressure fluctuation on the injector axis. A pressure probe placed at 5 mm from the injector exit confirms this behavior. As expected pressure fluctuations are observed with a 2 % peak-to-peak oscillation with respect to the mean chamber pressure while the transverse velocity remains unperturbed. When the normal velocities at the boundaries are in phase opposition ($\phi = \pi$), the pressure vanishes on the centerline and the transverse velocity oscillation reaches its maximum (Fig. 7.2(b). Spectral analysis also indicates that the perturbed field is dominated by the imposed modulation frequency and that the harmonic content is negligible.

The simulated cases are defined in Tab. 7.1. Injection conditions correspond to case "N6". Modulation amplitudes of 1 and 2% of the mean chamber pressure are imposed. These two cases are studied for $\phi = 0$ and $\phi = \pi$ respectively corresponding to a pressure antinode and a pressure node on the central axis.
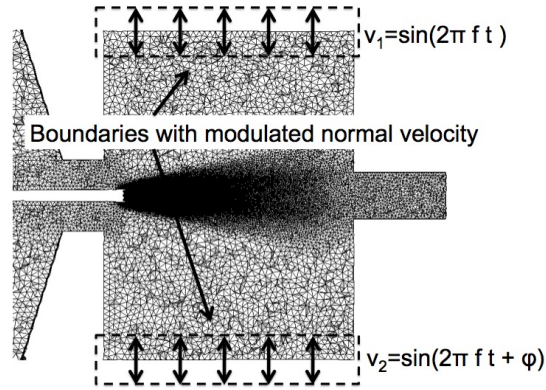
Figure 7.1: Longitudinal slice in the computational domain showing the methodology retained to impose acoustic perturbation.
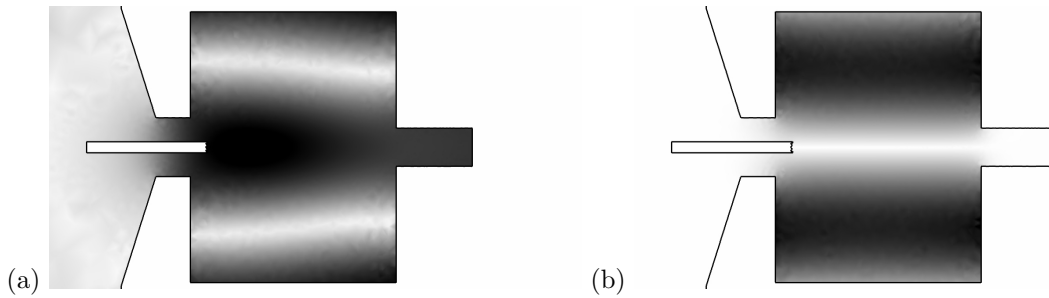
Figure 7.2: Results obtained under acoustic modulation in the absence of flow. (a) RMS pressure fluctuations for acoustic perturbations in phase ($\phi = 0$). (b) RMS pressure fluctuations for acoustic perturbations in phase opposition ($\phi = \pi$).

Case	$N6^{2\%}_{\phi=0}$	$N6^{2\%}_{\phi=\pi}$	$N6^{1\%}_{\phi=0}$	$N6^{1\%}_{\phi=\pi}$
P_{pp}/P_0	2.0 %	2.0 %	1.0 %	1.0 %
ϕ	0	π	0	π

Table 7.1: Test cases with acoustic modulation.

7.2 Calculated flow dynamics and experimental data

When acoustic modulations are in phase, pressure fluctuations are produced at the injector outlet at the modulation frequency. This leads to oscillations of the axial velocity at the imposed frequency. Such variations in the longitudinal velocity induce a periodic shedding of ring-like patterns (Fig. 7.3). Structures are created behind the inner lip and in the outer mixing layer. These structures develop in an axi-symmetric fashion producing annular vortices. The vortices produced in the inner jet lip entrain fluid from the inner jet, involving mass from the inner jet in the vortex roll-up. These results are qualitatively consistent with experimental observations shown in Fig. 7.5(a), where a varicose motion is clearly identifiable. When acoustic perturbations are in phase-opposition (Fig. 7.4), the resulting
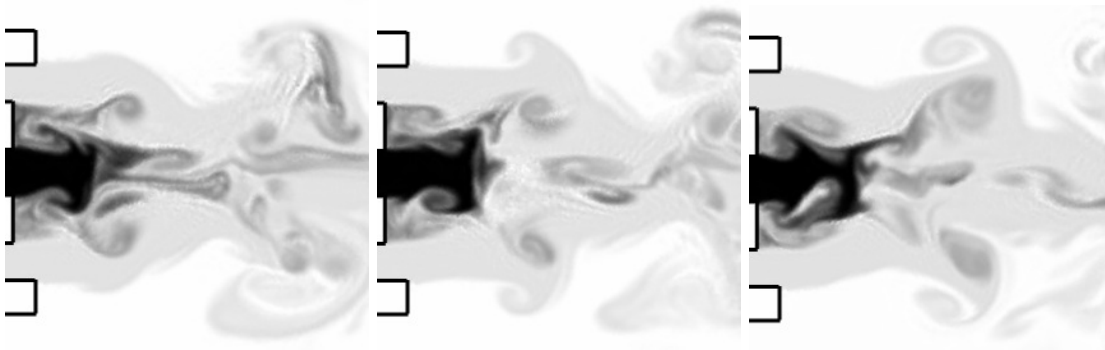
Figure 7.3: Case "N6$_{\phi=0}^{2\%}$" (J=3.05). Longitudinal slices of density (white: 60 kg m^{-3} ; black: maximum ; logarithmic scale). These images correspond to three successive times in one period.

transverse velocity perturbation induces a sinusoidal motion, as observed experimentally in Fig. 7.5(b) and vortices are shed in an asymmetric fashion.
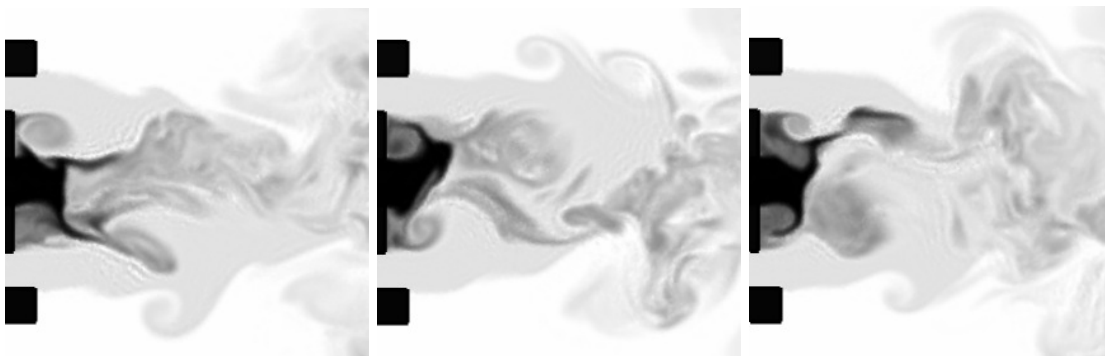
Figure 7.4: Case "N6$_{\phi=\pi}^{2\%}$" (J=3.05). Longitudinal slices of density (white: 60 kg m^{-3} ; black: maximum ; logarithmic scale). These images correspond to three successive times in one period.

The centerline density and axial velocity are plotted in Fig. 7.6. Acoustic perturbations significantly reduce the dense core length and increase the amplitude of the low velocity region just behind the central jet. Characteristic length ratios between acoustically perturbed cases and the reference case "N6" are

(a)   (b)
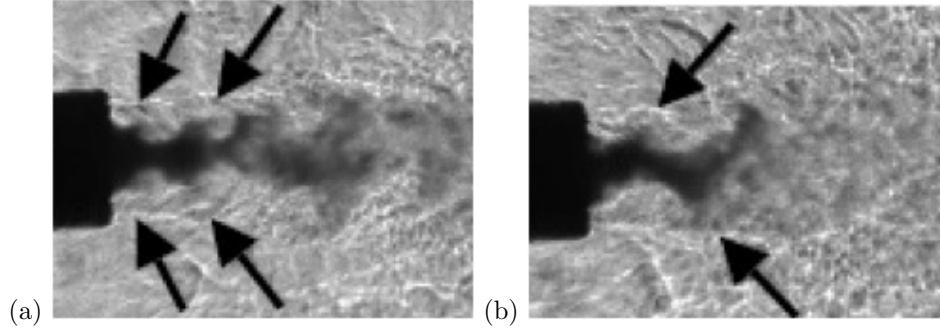
Figure 7.5: Experimental shadowgraphs for case "N6". (a) Acoustic modulation is in phase, (b) Acoustic modulation is in phase-opposition.

given in Tab. 7.2. These ratios are in agreement with experimental measurements. It is interesting to note that the cases corresponding to phase opposition produce the shortest dense core. It is also found that multiplication of the perturbation amplitude by a factor of two does not lead to a proportional reduction of the dense core.

(a)   (b)
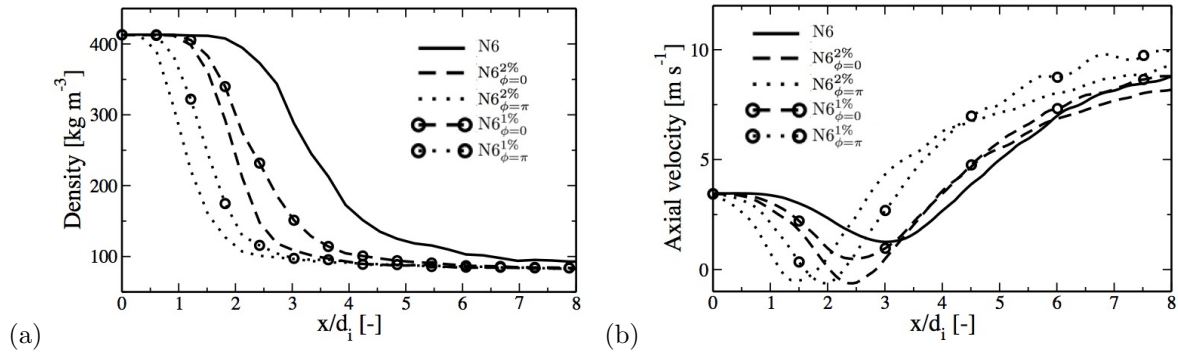
Figure 7.6: (a) Density profile on the centerline. (b) Axial velocity profile on the centerline.

Case	$N6^{2\%}_{\phi=0}$	$N6^{2\%}_{\phi=\pi}$	$N6^{1\%}_{\phi=0}$	$N6^{1\%}_{\phi=\pi}$
$l^{0.5}_\rho / l^{0.5}_{\rho,noac}$	0.60	0.34	0.70	0.45
$l^{0.1}_\rho / l^{0.1}_{\rho,noac}$	0.53	0.36	0.66	0.45
Experiments	-	-	0.68	0.55

Table 7.2: Influence of acoustic modulations on the characteristic length in case "N6".

7.3   Spectral analysis of acoustic modulation effects

The response of the flow to the external modulation may now be discussed by examining the spectral content of velocity fluctuations. This is done by plotting spectral maps of these fluctuations along three

axial lines in the flow. The first (line C) corresponds to the centerline, the second (line B) is centered on the lip, the third (line A) is centered on the outer jet annulus (see Fig. 7.7).
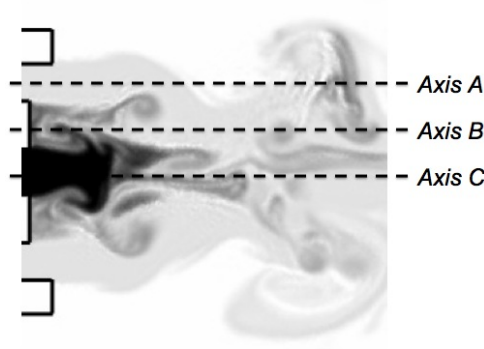
Figure 7.7: Case "N6$_{\phi=0}^{2\%}$" (J=3.05). Positions of the three axial lines used in the spatial spectral analysis.

7.3.1 Case "N6$_{\phi=0}^{2\%}$"

In phase excitation induces axial velocity modulations on the centerline. This is clearly seen in Fig. 7.8(a), 7.9(a) and 7.10(a), where the 3 000 Hz fluctuations are well retrieved. The amplitude of the axial velocity fluctuation is nevertheless very low in the high-density region (Fig. 7.11), in the potential core of the inner jet ($x <$1.05 d$_i$, defined by the region along the centerline axis where $\rho > 0.99\rho_i$, see Fig. 7.6(a)). This region of the flow is less affected by the axial modulation than the surround streams. The response of the jets to this modulation is determined by examining the transverse velocity. Both the outer jet and the flow behind the inner lip show a strong response at 3 000 Hz (Fig. 7.8(b) and 7.9(b)). It means that the axial perturbation promotes a destabilization of these jets and vortex roll-up at the same frequency. This is not the case along the inner jet centerline, where the transverse response at 3 000 Hz is not distinguishable (Fig. 7.10(b)). Since the geometry and the perturbation are both axisymmetric around this axis, such a velocity motion is naturally limited. The dominant frequency after the potential core ($x >$1.05 d$_i$) is close to 1 000 Hz. The spectral content of the inner jet is shown in Fig. 7.11 at $x = d_i$, at the end of the potential core. The axial velocity is dominated by the modulation at 3 000 Hz, with a low amplitude, but also features a lower frequency component around 1 200 Hz. In contrast with the outer jet, the radial velocity responds at half of the imposed frequency (around 1 500 Hz). These fluctuations are nevertheless small compared to those measured in the gaseous part of the flow. As a consequence, the high density part of the inner jet seems to be virtually insensitive to the acoustic modulation. The frequency that dominates at the end of the potential core is close to half of the modulation frequency. This frequency is also observed in the analysis of density fluctuations.

7.3.2 Case "N6$_{\phi=\pi}^{2\%}$"

A transverse velocity modulation is again applied at 3 000 Hz but the phase is now equal to π. As in the previous case "N6$_{\phi=0}^{2\%}$", this transverse modulation affects all the jets as shown in Fig. 7.12 (b), 7.13 (b) and 7.14 (b). The amplitude of this transverse perturbation is much lower in the high density part of the inner jet (Fig. 7.15 and 7.14(b) for $x < d_i$). Axial velocity perturbations are induced in the outer jet and behind the inner lip (Fig. 7.12(a) and 7.13(a)), associated with vortex roll-up at the same frequency.

Axis A
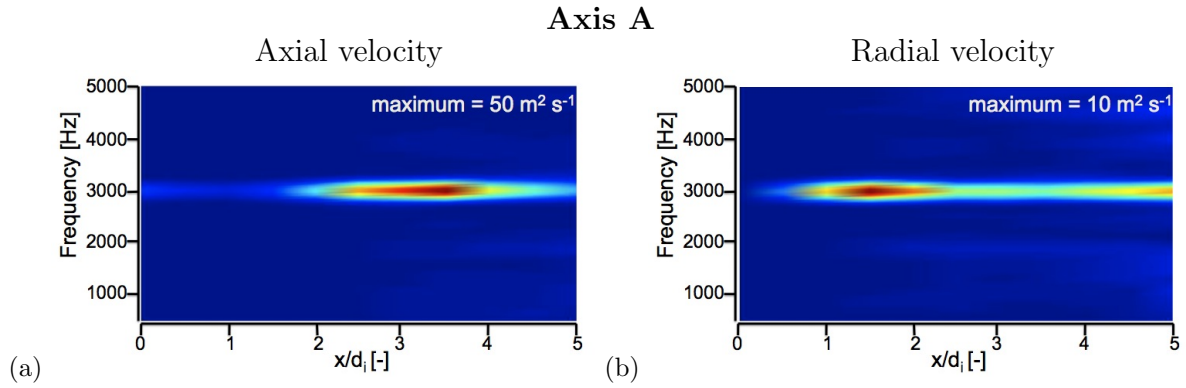
Figure 7.8: Case "N6$_{\phi=0}^{2\%}$" (J=3.05). Spectral map along line A ($r = d_i/2 + l_i + h_e/2$). (a) Axial velocity, (b) Radial velocity.
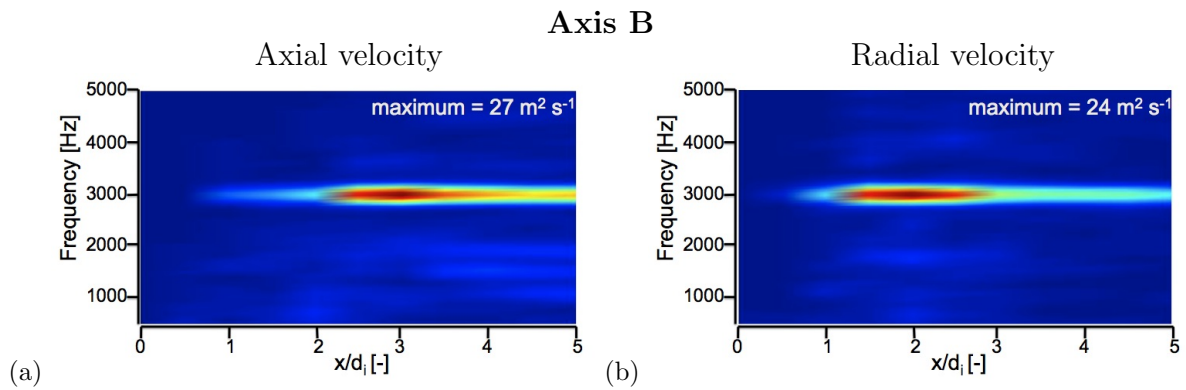
Axis B

Figure 7.9: Case "N6$_{\phi=0}^{2\%}$" (J= 3.05). Spectral map along line B ($r = d_i/2 + l_i/2$). (a) Axial velocity and (b) Radial velocity.

Axis C
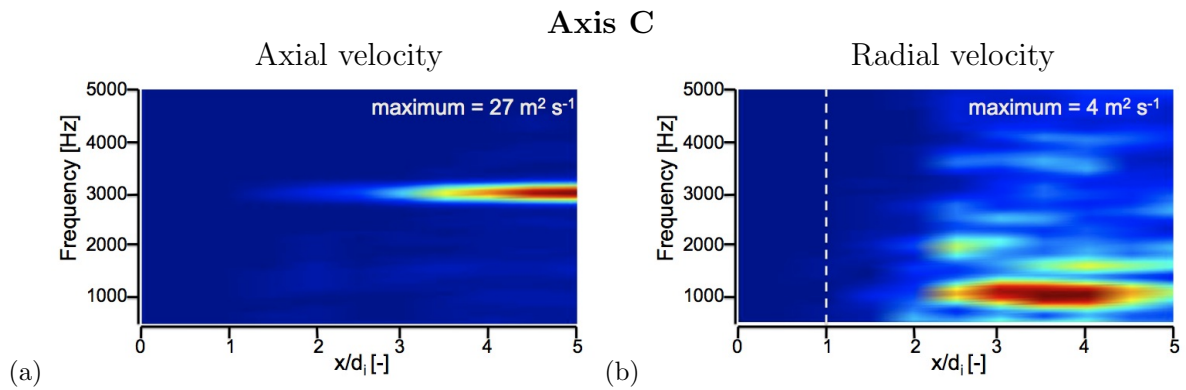
Figure 7.10: Case "N6$_{\phi=0}^{2\%}$" (J= 3.05). Spectral map along line C ($r = 0$). (a) Axial velocity, (b) Radial velocity. The dashed line represents the axial position at which a power spectral density is shown in Fig. 7.11.
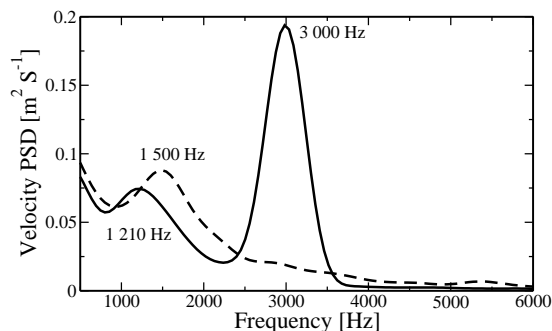
Figure 7.11: Case "N6$^{2\%}_{\phi=0}$" ($J= 3.05$). Power spectral density of axial (—) and radial (− −) velocity in the inner jet centerline at $x = d_i$ (end of the potential core).

Again, the inner jet is essentially unaffected, since the measured amplitudes are much lower than for the two other cases (Fig. 7.14(a)). This stream is dominated by an intermediate frequency. A component at 1 500 Hz is observed just at the inner injector exit. This is confirmed on Fig. 7.15, where the transverse modulation at 3 000 Hz is visible, but leads to a longitudinal response of the jet close to 1 500 Hz. Even though this frequency is clearly identifiable in Fig. 7.14(a) and 7.15, its amplitude is lower than that measured behind the lip or in the outer jet. As previously observed for in phase modulation, the sensitivity of the inner jet to the external modulation is limited. Again, the frequency which dominates at the end of the potential core ($x <0.55$ d$_i$, see Fig. 7.6(a)) is close to half of the modulation frequency and is also observed in density fluctuations.

Axis A
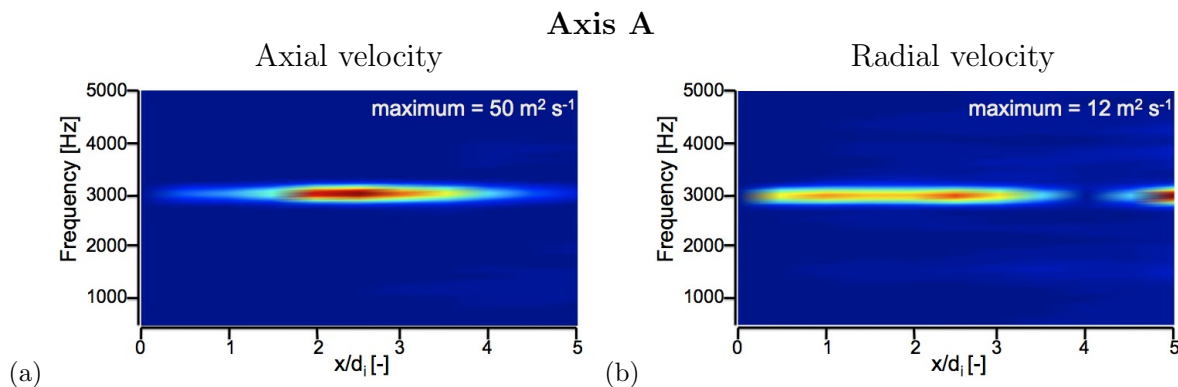
Figure 7.12: Case "N6$^{2\%}_{\phi=\pi}$" ($J= 3.05$). Spectral map along line A ($r = d_i/2 + l_i + h_e/2$). (a) Axial velocity and (b) Radial velocity.

7.4 Discussion

It is found that the inner jet, when submitted to an acoustic modulation at 3 000 Hz, exhibits fluctuations at the subharmonic frequency of 1 500 Hz. This may be explained by considering the stability properties

Axis B

Axial velocity

maximum = 16 m² s⁻¹

(a)

Radial velocity

maximum = 38 m² s⁻¹

(b)
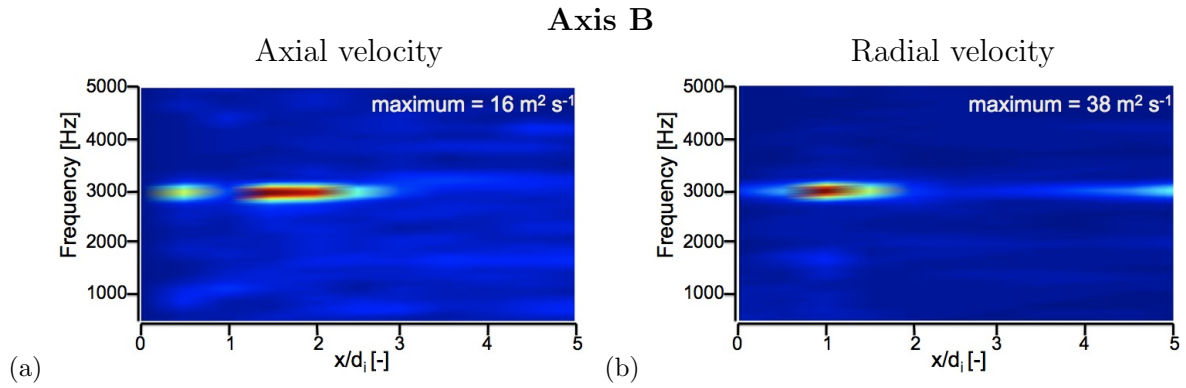
Figure 7.13: Case "N6$_{\phi=\pi}^{2\%}$" (J= 3.05). Spectral map along line B ($r = d_i/2 + l_i/2$). (a) Axial velocity and (b) Radial velocity.

Axis C

Axial velocity

maximum = 4 m² s⁻¹

a)

Radial velocity

maximum = 42 m² s⁻¹

b)
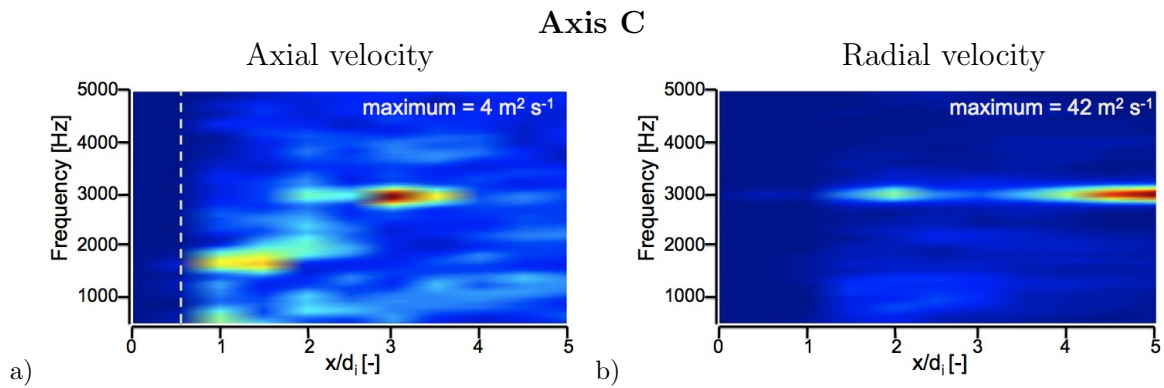
Figure 7.14: Case "N6$_{\phi=\pi}^{2\%}$" (J= 3.05). Spectral map along line C ($r = 0$). (a) Axial velocity and (b) Radial velocity. The dashed line represents the axial position at which a power spectral density is shown in Fig. 7.15.
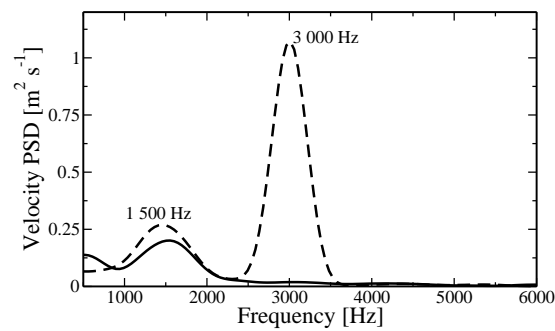

Figure 7.15: Case "N6$_{\phi=\pi}^{2\%}$" (J= 3.05). Power spectral density of axial (——) and radial ($--$) velocity on the inner jet centerline at $x = 0.5d_i$ (end of the potential core).

of the central jet and by analyzing the acoustic transmission from the outer medium into the high density region.

It is first interesting to situate the modulation frequency with respect to the range of unstable frequencies characterizing the jet and more specifically with respect to the preferred frequency of the inner jet. It is known (see for example Birbaud et al. [3] and references in this article) that when the modulation frequency is well above the preferred mode frequency, the flow is not affected by an external acoustic modulation. This is best expressed in terms of a Strouhal numbers which can be calculated by considering the acoustic modulation frequency, the characteristic length and velocity associated with each jet. The resulting "acoustic" Strouhal numbers are given in Tab. 7.3. While St_{ac}^{e} and St_{ac}^{l} are lower or close to the natural Strouhal number of the flow for case "N6", St_{ac}^{i} is higher than the one measured previously without modulation. As a consequence, the jet does not respond to the modulation frequency, but oscillates at a subharmonic frequency (1 500Hz) which is close to the preferred frequency measured previously in the absence of acoustic modulation (Fig. 6.9).

$St = (f_{ac}l)/u$	length scale l	charac. vel. u	value
St_{ac}^{e}	h_e (0.41 mm)	u_e	0.087
St_{ac}^{l}	l_i (0.54 mm)	u_e	0.115
St_{ac}^{i}	d_i (0.51 mm)	u_i	0.45

Table 7.3: Definition of the Strouhal numbers used in this study. f represents the modulation frequency (3 000 Hz).

Another possible explanation of the absence of modulation at the imposed frequency may be obtained by considering the change in acoustic impedance between the outer stream and the inner jet. It is known that a large impedance mismatch reduces the transmission of waves across the interface. Acoustic impedances gathered in Tab. 7.4 indicate that a large variation takes place at the inner jet boundary. Under these circumstances acoustic wave transmission into the jet is reduced explaining the absence of the modulation imposed to the system from the outer region.

Conditions	Impedance ($Z = \rho c$)
Chamber	17 701
Outer jet	19 663
Inner jet	98 700

Table 7.4: Specific acoustic impedance in the chamber, inner and outer jets.

The previous arguments provide some clues on the observed response of the coaxial flow to an externally imposed transverse acoustic motion. The strong reduction of the inner jet length is certainly linked to the strong response of the outer jet to the acoustic modulation, which is not observed for the inner stream. The large vortices generated in the annular jet in turn enhance mixing between the outer and inner jets, and thus enhances mixing of the inner fluid with its surroundings, leading to a reduction of the dense core length.

Chapter 8

Conclusion

The structure of non reactive transcritical and supercritical jets is investigated by examining the flow formed by a coaxial injector operating at high pressure. This unit injects low temperature dense nitrogen surrounded by an outer stream of higher temperature nitrogen. The analysis relies on large eddy simulations which are compared with experimental results. The natural development of the coaxial flow is examined for a set of momentum flux ratios. It is shown that the flow patterns observed experimentally are suitably retrieved and that a good correspondence between experimental results and simulations is obtained. It is shown in particular that when the momentum flux ratio exceeds a critical value, the central jet is terminated in an abrupt fashion at a short distance from the injector exhaust. Calculations indicate that this is linked to the formation of a recirculation region located at a short distance from the injection section. This study is complemented with a spectral analysis of the velocity components in the injector nearfield. It is shown that the frequency content is governed by Strouhal numbers which follow standard rules for jets and wakes. The effect of an external acoustic modulation is then investigated by imposing in phase and out of phase perturbations at the boundaries of the domain. This is used to study the effect of transverse waves on the dark core in the jet. A strong reduction of the jet length is clearly observed, both in experiment and numerics. The spectral content of fluctuations in the coaxial streams is analyzed. In the case considered which corresponds to a Strouhal number (based on the inner jet velocity and diameter) about equal to twice the Strouhal number corresponding to the preferred mode of the jet, it is found that the inner jet responds with a limited amplitude to the external modulation but features a subharmonic motion at half of the modulation frequency. In contrast, the gaseous part of the flow is strongly perturbed by the acoustic modulation. Large scale vortices are released from the outer annulus at the modulation frequency. It is suggested that the relative insensitivity of the inner flow is linked to the fact that the frequency is above the range of unstable frequencies of the central jet. It is also found that the specific acoustic impedance of the central jet is much higher than that corresponding to the surrounding stream and that this may explain why the modulation is not transmitted to the central core.

Acknowledgments

Bibliography

[1] J. Bellan. Supercritical (and subcritical) fluid behavior and modeling: drops, streams, shear and mixing layers, jets and sprays. *Progress in Energy and Combustion Science*, 26:329–366, 2000.

[2] J. Bellan. Theory, modeling and analysis of turbulent supercritical mixing. *Combustion Science and Technology*, 178(1):253–281, 2006.

[3] A. L. Birbaud, D. Durox, S. Ducruix, and S. Candel. Dynamics of free jets submitted to upstream acoustic modulations. *Physics of Fluids*, 19:013602, 2007.

[4] R. Branam and W. Mayer. Characterisation of cryogenic injection at supercritical pressure. *Journal of Propulsion and Power*, 19(3):342–355, May-June 2003.

[5] S. Candel, M. Juniper, G. Singla, P. Scouflaire, and C. Rolon. Structure and dynamics of cryogenic flames at supercritical pressure. *Combustion Science and Technology*, 178:161–192, 2006.

[6] I. Celik, A. Smirnov, and J. Smith. Appropriate initial and boundary conditions for LES of a ship wake. In *Proceedings of the 3rd ASME/JSME Joint Fluids Engineering Conference*, volume FEDSM99-7851, San Francisco, California, USA, 1999.

[7] M.W. Chase. *NIST-JANAF thermochemical tables*. American Institute of Physics,-1, 1998.

[8] B. Chehroudi and D. Talley. Interaction of acoustic waves with a cryogenic nitrogen jet at sub- and supercritical pressures. In *40th AIAA, Aerospace Science Meeting & Exhibit, Reno, Nevada*, January 2002.

[9] B. Chehroudi, D. Talley, and E. Coy. Visual characteristics and initial growth rate of round cryogenic jets at subcritical and supercritical pressures. *Physics of Fluids*, 14(2):850–861, february 2002.

[10] C. J. Chen and W. Rodi. *Vertical turbulent buoyant jets: A review of experimental data*. Pergamon Press, 1980.

[11] G.C. Cheng and R. Farmer. Real fluid modeling of multiphase flows in liquid rocket engine combustors. *Journal of Propulsion and Power*, 22(6):1373–1381, 2006.

[12] T.H. Chung, M. Ajlan, L.L. Lee, and K.E. Starling. Generalized multiparameter correlation for nonpolar and polar fluid transport properties. *Industrial & Engineering Chemistry Research*, 27(4):671–679, 1988.

[13] D. W. Davis and B. Chehroudi. Measurements in an acoutically-driven coaxial jet under sub-, near-, and supercritical conditions. *Journal of Propulsion and Power*, 23(2):364–374, 2007.

49

[14] D.W. Davis, B. Chehroudi, and I. Sorensen. Measurements in an acoustically driven coaxial jet under supercritical conditions. In *43rd AIAA Aerospace Sciences Meeting & Exhibit*, pages 10–13, 2005.

[15] R. Dehoff. *Thermodynamics in Materials Science*. Taylor & Francis, second edition edition, 2006.

[16] F.X. Demoulin, S. Zurbach, and A. Mura. High-Pressure Supercritical Turbulent Cryogenic Injection and Combustion: A Single-Phase Flow Modeling Proposal. *Journal of propulsion and power*, 25(2), 2009.

[17] N. Guezennec and T. Poinsot. Acoustically non-reflecting and reflecting boundary conditions for injection of vortical flows in compressible solvers. *American Institute of Aeronautics and Astronautics Journal*, 2009.

[18] J. Gullbrand and F. K. Chow. The effect of numerical errors of turbulence models in large eddy simulations of channel flow, with and without explicit filtering. *Journal of Fluid Mechanics*, 495:323–341, 2003.

[19] M. Habiballah, M. Orain, F. Grisch, L. Vingert, and P. Gicquel. Experimental studies of high-pressure cryogenic flames on the Mascotte facility. *Combustion Science and Technology*, 178(1):101–128, 2006.

[20] J.O. Hirschfelder, C.F. Curtiss, and R.B. Bird. *Molecular theory of gases and liquids*. Wiley New York, 1954.

[21] A. G. Kravchenko and P. Moin. On the effect of numerical errors in large eddy simulations of turbulent flows. *Journal of Computational Physics*, 131:310–322, 1996.

[22] JC Lasheras, E. Villermaux, and EJ Hopfinger. Break-up and atomization of a round water jet by a high-speed annular air jet. *Journal of Fluid Mechanics*, 357:351–379, 1998.

[23] E.W. Lemmon, M.O. McLinden, and D.G. Friend. Thermophysical properties of fluid systems. In Eds. P.J. Linstrom and W.G. Mallard, editors, *NIST Chemistry WebBook, NIST Standard Reference Database 69*, Gaithersburg, MD, first retrieved May 2007. National Institute of Standards and Technology.

[24] I. A. Leyva, J. Rodriguez, B. Chehroudi, and D. Talley. Preliminary results on coaxial jet spread angles and the effects of variable phase transverse acoustic fields. In *46th AIAA Aerospace Sciences Meeting and Exhibit, Reno, Nevada, Jan. 7-10*, volume AIAA-2008-950, 2008.

[25] I.A. Leyva, B. Chehroudi, and D. Talley. Dark Core Analysis of Coaxial Injectors at Sub-, Near-, and Supercritical Conditions in a Transverse Acoustic Field. In *43rd AIAA/ASME/SAE/ASEE Joint Propulsion Conference and Exhibit, Cincinnati, OH, July 8-11*, volume AIAA-2007-5456, 2007.

[26] T. Liu, N. Zong, and V. Yang. Dynamics of Shear-Coaxial Cryogenic Nitrogen Jets with Acoustic Excitation under Supercritical Conditions. In *44th AIAA Aerospace Sciences Meeting and Exhibit, 9 - 12 January 2006, Reno, Nevada, AIAA 2006-75*, 2006.

[27] M. Masquelet, S. Menon, Y. Jin, and R. Friedrich. Simulation of unsteady combustion in a LOX-GH2 fueled rocket engine. *Aerospace Science and Technology*, 13(8):466–474, 2009.

[28] S. Matsuyama, J. Shinjo, S. Ogawa, and Y. Mizobuchi. Large Eddy Simulation of LOX/GH2 Shear-Coaxial Jet Flame at Supercritical Pressure. In *48th AIAA Aerospace Sciences Meeting, Orlando, Florida*, January 2010.

[29] W. Mayer, J. Tellar, R. Branam, G. Schneider, and J. Hussong. Raman measurement of cryogenic injection at supercritical pressure. *Heat and Mass Transfer*, 39:709–719, 2003.

[30] W.O.H. Mayer and R. Branam. Atomization characteristics on the surface of a round liquid jet. *Experiments in Fluids*, 36:528–539, 2004.

[31] H. Meng and V. Yang. A unified treatment of general fluid thermodynamics and its application to a preconditioning scheme. *Journal of Computational Physics*, 189(1):277–304, 2003.

[32] Y. Mery, S. Ducruix, P. Scouflaire, and S. Candel. Injection coupling with high amplitude transverse modes: Experimentation and simulation. *Comptes Rendus Mécanique*, 337(6-7):426–437, 2009.

[33] R. S. Miller, K. G. Harstad, and J. Bellan. Direct numerical simulation of supercritical fluid mixing layers applied to heptane-nitrogen. *Journal of Fluid Mechanics*, 436:1–39, 2001.

[34] V. Moureau, G. Lartigue, Y. Sommerer, C. Angelberger, O. Colin, and T. Poinsot. High-order methods for DNS and LES of compressible multi-component reacting flows on fixed and moving grids. *Journal of Computational Physics*, 202(2):710–736, 2005.

[35] F. Nicoud and F. Ducros. Subgrid-scale stress modelling based on the square of the velocity gradient. *Flow, Turbulence and Combustion*, 62(3):183–200, 1999.

[36] J. C. Oefelein and V. Yang. Modeling high-pressure mixing and conbustion processes in liquid rocket engines. *Journal of Propulsion and Power*, 14(5):843–857, 1998.

[37] J.C. Oefelein. Thermophysical characteristics of shear-coaxial LOX-H2 flames at supercritical pressure. *Proceedings of the Combustion Institute*, 30(2):2929–2937, 2005.

[38] J.C. Oefelein. Mixing and combustion of cryogenic oxygen-hydrogen shear-coaxial jet flames at supercritical pressure. *Combustion Science and Technology*, 178(1):229–252, 2006.

[39] N. Okong'o and J. Bellan. Consistent boundary conditions for multicompoment real gas mixtures based on characteristic waves. *Journal of Computational Physics*, 176:330–344, 2002.

[40] M. Oschwald and M. M. Micci. Spreading angle and centerline variation of density of supercritical nitrogen jets. *Atomization and Sprays*, 11:91–106, 2002.

[41] M. Oschwald and A. Schik. Supercritical nitrogen free jet investigated by spontaneous raman scattering. *Experiments in Fluids*, 27:497–506, 1999.

[42] M. Oschwald, A. Schik, M. Klar, and W. Mayer. Investigation of coaxial LN2-GH2-injection at supercritical pressure by spontaneous Raman scattering. AIAA 99-2887. In *35th Joint Propulsion Conference, Los Angeles, CA*, 1999.

[43] M. Oschwald, J. J. Smith, R. Branam, J. Hussong, A. Shick, B. Chehroudi, and D. Talley. Injection of fluids into supercritical environments. *Combustion Science and Technology*, 178:49–100, 2006.

[44] N. Otsu. A threshold selection method from gray-level histograms. *Automatica*, 11:285–296, 1975.

[45] D. Peng and D. B. Robinson. A new two-constant equation of state. *Ind. Eng. Chem. Fundam.*, 15:59–64, 1976.

[46] T. Poinsot and S. Lele. Boundary conditions for direct simulations of compressible viscous flows. *Journal of Computational Physics*, 101(1):104–129, 1992.

[47] B. E. Poling, J. M. Prausnitz, and J. P. O'Connel. *The properties of gases and liquids*. McGraw-Hill, fifth edition, 2001.

[48] L. Pons, N. Darabiha, S. Candel, T. Schmitt, and B. Cuenot. The structure of multidimensional strained flames under transcritical conditions. *Comptes rendus-Mécanique*, 337(6-7):517–527, 2009.

[49] M.M. Poschner and M. Pfitzner. CFD-Simulation of the injection and combustion of LOX and H2 at supercritical pressures. In *Proceedings of the European Combustion Meeting 2009*, 2010.

[50] L. Quartapelle and V. Selmin. High-order Taylor-Galerkin methods for non-linear multidimensional problems., 1993.

[51] H. Rehab, E. Villermaux, and EJ Hopfinger. Flow regimes of large-velocity-ratio coaxial jets. *Journal of Fluid Mechanics*, 345:357–381, 1997.

[52] C. Rey, S. Ducruix, and S. Candel. A method for the transverse modulation of reactive flows with application to combustion instability. *Combustion Theory and Modelling*, 9:5–22, 2005.

[53] F. Richecoeur, P. Scouflaire, S. Ducruix, and S. Candel. High-frequency transverse acoustic coupling in a multiple-injector cryogenic combustor. *Journal of propulsion and power*, 22(4):790–799, 2006.

[54] J. Rodriguez, J. Graham, I. Leyva, and D. Talley. Effect of Variable Phase Transverse Acoustic Fields on Coaxial Jet Forced Spread Angles. In *47th AIAA Aerospace Sciences Meeting including The New Horizons Forum and Aerospace Exposition, Orlando, Florida, Jan. 5-8*, volume AIAA-2009-231. American Institute of Aeronautics and Astronautics, 1801 Alexander Bell Dr., Suite 500 Reston VA 20191-4344 USA,, 2009.

[55] J. Rodriguez, I. Leyva, J. Graham, and D. Talley. Mixing Enhancement of Liquid Rocket Engine Injector Flow. In *45th AIAA/ASME/SAE/ASEE Joint Propulsion Conference and Exhibit, Denver, Colorado, Aug. 2-5*, volume AIAA-2009-5143, 2009.

[56] A. Roy and C. Segal. Experimental Study of Fluid Jet Mixing at Supercritical Conditions. *Journal of Propulsion and Power*, 26(6), 2010.

[57] T. Schmitt, Y. Méry, M. Boileau, and S. Candel. Large-Eddy Simulation of oxygen/methane flames under transcritical conditions. *Proceedings of the Combustion Institute*, 2010.

[58] T. Schmitt, L. Selle, B. Cuenot, and T. Poinsot. Large-Eddy Simulation of transcritical flows. *Comptes Rendus Mécanique*, 337(6-7):528–538, 2009.

[59] T. Schmitt, L. Selle, A. Ruiz, and B. Cuenot. Large-Eddy Simulation of Supercritical-Pressure Round Jets. *AIAA journal*, 48(9), 2010.

[60] T. Schönfeld and T. Poinsot. Influence of boundary conditions in LES of premixed combustion instabilities. In *Annual Research Briefs*, pages 73–84. Center for Turbulence Research, NASA Ames/Stanford Univ., 1999.

[61] C. Segal and SA Polikhov. Subcritical to supercritical mixing. *Physics of Fluids*, 20:052101, 2008.

[62] L. Selle and T. Schmitt. Large-eddy simulation of single-species flows under supercritical thermodynamic conditions. *Combustion Science and Technology*, 182(4):392–404, 2010.

[63] L.C. Selle, N.A. Okong'o, J. Bellan, and K.G. Harstad. Modelling of subgrid-scale phenomena in supercritical transitional mixing layers: an a priori study. *Journal of Fluid Mechanics*, 593:57–91, 2007.

[64] G. Singla. *Etude des Flammes Cryotechniques Oxygène Liquide/Méthane à Haute Pression.* PhD thesis, Ecole Centrale de Paris, 2005.

[65] G. Singla, P. Scouflaire, C. Rolon, and S. Candel. Planar laser-induced fluorescence of OH in high-pressure cryogenic LOx/GH2 jet flames. *Combustion and Flame*, 144(1-2):151–169, 2006.

[66] A. Smirnov, S. Shi, and I. Celik. Random flow generation technique for large eddy simulations and particle-dynamics modeling. *Trans. ASME. Journal of Fluids Engineering*, 123:359–371, 2001.

[67] J. J. Smith, G. Schneider, D. Suslov, M. Oschwald, and O. Haidn. Steady-state high pressure lox/h2 rocket engine combustion. *Aerospace Science and Technology*, 11:39–47, 2007.

[68] E.S. Taskinoglu and J. Bellan. A posteriori study using a DNS database describing fluid disintegration and binary-species mixing under supercritical pressure: heptane and nitrogen. *Journal of Fluid Mechanics*, 645:211–254, 2010.

[69] E. Villermaux and H. Rehab. Mixing in coaxial jets. *Journal of Fluid Mechanics*, 425:161–185, 2000.

[70] D. Wee, T. Yi, A. Annaswamy, and A.F. Ghoniem. Self-sustained oscillations and vortex shedding in backward-facing step flows: Simulation and linear instability analysis. *Physics of Fluids*, 16:3361–3373, 2004.

[71] V. Yang. Modeling of supercritical vaporization, mixing, and combustion processes in liquid-fueled propulsion systems. *Proceedings of the Combustion Institute*, 28(1):925–942, 2000.

[72] V. Yang. *Liquid rocket thrust chambers: aspects of modeling, analysis, and design.* Aiaa, 2004.

[73] N. Zong. *Modeling and simulation of cryogenic fluid injection and mixing dynamics under supercritical conditions.* PhD thesis, The Pennsylvania State University, 2005.

[74] N. Zong, H. Meng, S.-Y. Hsieh, and V. Yang. A numerical study of cryogenic fluid injection and mixing under supercritical conditions. *Physics of Fluids*, 16(12):4248–4261, 2004.

[75] N. Zong and V. Yang. A numerical study of high-pressure oxygen/methane mixing and combustion of a shear coaxial injector. *AIAA paper*, 152, 2005.

[76] N. Zong and V. Yang. Cryogenic fluid jets and mixing layers in transcritical and supercritical environments. *Combustion Science and Technology*, 178(1):193–227, 2006.

[77] N. Zong and V. Yang. Near-field flow and flame dynamics of LOX/methane shear-coaxial injector under supercritical conditions. *Proceedings of the Combustion Institute*, 31(2):2309–2317, 2007.

Nomenclature

α Thermal expansion coefficient

β Isothermal compressibility coefficient

λ Thermal conductivity

μ Dynamic viscosity

μ^t Turbulent dynamic viscosity

ν^t Turbulent kinematic viscosity

ω Acentric factor

ρ Density

ρ^* Normalized density $(\rho - \rho_\infty)/(\rho_c - \rho_\infty)$

ρ_∞ Far field density

ρ_∞ Reservoir initial density

ρ_c Time averaged centerline density

ρ_e Outer jet injection density

ρ_i Inner jet injection density

τ Viscous-stress tensor

τ^t SGS stress tensor

a, b, c Coefficients for the Peng-Robinson equation of state

c_p Constant pressure specific heat

c_v Constant volume specific heat

C_w WALE model constant

d_i Inner jet diameter

E Total energy

e_s Internal energy

E_ρ^H	Spreading rate of the density profile
h_e	annular duct thickness
h_s	Enthalpy
J	Momentum flux ratio
l_i	Inner lip thickness
L_ρ	'Half Width at Half Maximum' of the density profile
$l_\rho^{0.1}$	$x_\rho^{0.1} - x_0$
$l_\rho^{0.5}$	$x_\rho^{0.5} - x_0$
$l_\rho^{0.99}$	$x_\rho^{0.99} - x_0$
l_u	$x_u - l_u$
p	Pressure
P_c	Critical pressure
R	Ideal gas constant
r	Specific gas constant
S	Density ratio
S	Symmetric part of the velocity-gradient tensor
s	Symmetric traceless part of the square of the velocity-gradient tensor
T	Temperature
T_c	Critical temperature
T_r	Reduced temperature
T_∞	Reservoir initial temperature
T_{aver}	Duration of the averaging procedure
T_e	Outer jet injection temperature
T_i	Inner jet injection temperature
U	Velocity ratio
u	Axial velocity
$u^* = u/u_e$	Normalized velocity
u_∞	Reservoir initial velocity
u_e	Outer jet injection velocity
u_i	Inner jet injection velocity

$x_\rho^{0.1}$ Axial centerline position where $\rho = 0.1(\rho_i - \rho_e) + \rho_e$

$x_\rho^{0.5}$ Axial centerline position where $\rho = 0.5(\rho_i - \rho_e) + \rho_e$

$x_\rho^{0.99}$ Axial centerline position where $\rho/\rho_i = 0.99$

x_u Axial centerline position where axial velocity is minimum

$\mathbf{q^t}$ SGS heat flux vector

$\mathbf{q}$ Heat flux

$\mathbf{v}$ Velocity vector

$\mathbf{w}$ Vector of conservative variables

Pr^t Turbulent Prandtl number

Re Reynolds number

St^b $(fu_e)/(d_i + l_i)$

St^e $(fu_e)/h_e$

St^i $(fu_i)/d_i$

St^l $(fu_e)/l_i$

Appendix A

Injection conditions for the computed cases

Outer jet injection conditions

Case	T_e [K]	$\dot{m}_e$ [g.s^{-1}]	ρ_e [kg.m^{-3}]	u_e [m.s^{-1}]	Re_e
N2	152	1.57	101	5.95	41 600
N6	183	2.69	73.1	14.1	64 800
N8	192	6.46	68.3	36.2	151 000

Table A.1: Injection conditions corresponding to the cases "N2", "N6" and "N8" for the **outer** jet. $\dot{m}$ denotes the mass flow rate.

Inner jet injection conditions

Case	T_i [K]	$\dot{m}_i$ [g.s^{-1}]	ρ_i [kg.m^{-3}]	u_i [m.s^{-1}]	Re_i
N2	117	0.289	590	2.4	15 000
N6	126	0.292	420	3.4	25 000
N8	128	0.295	220	6.6	52 000

Table A.2: Injection conditions corresponding to the cases "N2", "N6" and "N8" for the **inner** jet. $\dot{m}$ denotes the mass flow rate.

Part II

Experiments and Modeling of Transcritical Flows: Spectral Analysis of Results

Spectral analysis of coaxial jets under transcritical conditions

Authors: J. Rodriguez[1,2], T. Schmitt[1], S. Candel[1] and I. A. Leyva[2]

[1]EM2C, CNRS, École Centrale Paris, 92295 Châtenay-Malabry, France,
[2]AFRL/RZSA, Edwards AFB, CA. 93524, USA

List of Figures

List of Tables

Chapter 1

Abstract

The following work stems from the spectral analysis performed by Schmitt *et al.* [1] to the LES data presented in chapters 6 and 7 in part I of this report. In this study, results from the spectral analysis of the experimental data corresponding to two cases analyzed by Schmitt *et al.* [1] with the LES techinque are presented and compared. An introduction explaining the objective of spectral analysis is given in Chapter 2 and the specific methods used are provided in Chapter 3. Results of this analysis are used to provide a better picture of the behavior of transcritical coaxial jets with and without acoustic excitation. In fact, spectral analysis is a technique that could be used extensively on other experimental datasets already obtained at AFRL to analyze frequency content. In Chapter 4, spectral maps of both experimental data and simulation results are presented. It is found that both techniques clearly identify the modulation frequency for cases with acoustic modulation.

Chapter 2

Introduction

Spectral analysis is a useful tool when there is a need to obtain more information about recurring events or values contained in any type of signal. From a large continuous data set one can extract the frequencies at which these recurring events or values take place. If there is only one recurring event on a signal, a clear, strong mode will be found using spectral analysis. If a signal has several recurring events taking place but there is one that predominates, the frequency or mode of this event will be highlighted over the others by this analysis, though it will not appear in a unique fashion as if there was only one recurring event.

Spectral methods have been used to determine whether a jet of variable density issuing into ambient air presents absolute or convective instability depending on the density ratio between the jet and the air [2]. According to the authors' analysis, different density ratios lead to different forms of the power spectral density (PSD). One shows the PSD of the jet's velocity with very sharp peaks in the near field of the jet while the other shows broader and less prominent peaks. Using an analogy between the PSD measured in the wake of a circular cylinder (with prominent peaks well above the rest of the signal) and the PSD measured in the unstable shear layer of a constant density isothermal round jet (with peaks that are hardly one order of magnitude larger than the rest of the signal), they conclude that the behavior one of the jets corresponds to absolutely instability and the other to convective instability.

Raynal et al. [3] studied variable-density jets using hot-wire anemometry. They used their power spectral results to find that flow stability was not affected by the presence of the hot-wire one jet diameter downstream the exit of the flow at several density ratios. They did find that as the probe was moved downstream (from 2 to 6 jet diameters) the spectra was characterized by the rise of a subharmonic frequency which is one half the dominant frequency. The previous behavior might be associated with the pairing process of periodic structures present in the flow. They also observed an increase of the spectral level, which reflects the spatial amplification of the perturbations as the hot-wire was moved downstream. The power spectra also showed that when the jet-to-ambient density ratio is increased from 0.31 to 0.61 the peak frequency decreases several orders of magnitude until it reaches the same size of the other smaller peaks at 0.51 and reaches the same magnitude of the background noise at 0.61.

In their work identifying combustion instabilities in a multiple inlet combustor, Poinsot et al. [4] use the power spectral density maps of the signal detected by a microphone and plot it as a function of air flow rate and equivalence ratio. Each map spans a frequency band centered around one resonant frequency of the system. They found that each mode occurs in a restricted domain of parameters and as

these parameters are increased the trend is to have higher acoustic intensities and frequencies.

For this brief analysis, we will use spectral analysis as a tool to identify periodicities in our data sets. These sets have been obtained via experiments and computer simulations of a cryogenic, transcritical coaxial jet. On the experimental side, the signal is the intensity of light at each pixel from the images captured by a high-speed camera. On the modeling side our data consists of the values of the different variables at a given location or node in the simulation mesh. There are two cases which are studied both experimentally and computationally. The effects of acoustics are also studied for one of the cases. These two cases will be compared and the results will be shown.

Chapter 3

Methods, assumptions and procedures

The experimental setup and the modeling method are the same as those described in sections 3 and 5 in part I of this report. For reference, the injector used in the experimental study and the computational model with respective lengths are reproduced in Figs. 3.1 and 3.2 below.
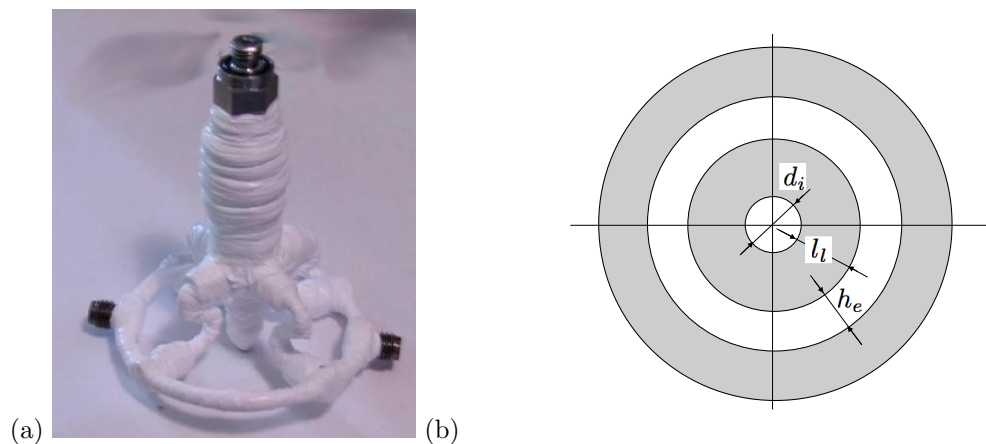
(a)   (b)

Figure 3.1: (a) Photograph of the shear coaxial injector used in this study. (b) Exit plane view of the injector with characteristic dimensions.

In order to analyze the spectral content of the data Welch's method was used in this study. This method allows the user to obtain an estimate of the intensity of the signal as a function of frequency. Welch's method is based on the method of averaged periodograms also known as Bartlett's method [5]. Periodograms are used to estimate the spectral content of a signal, but they present inherent problems such as large variance of the data and measurement noise. Bartlett's method takes the signal and divides it in smaller segments, then computes the periodogram of each segment and finally finds the average of the periodograms. This helps decrease variance issues with the data in exchange for the ability to resolve smaller frequency ranges [6].
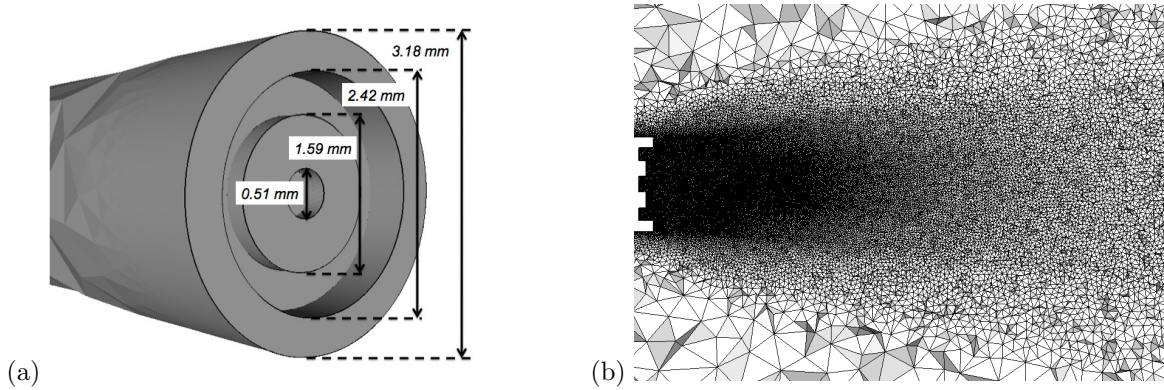
Figure 3.2: (a) Closer view of the injector. (b) Longitudinal cut of the mesh (35 d_i).

Welch's method also uses the same type of averaging introduced by Bartlett's method and adds a procedure that helps reduce the noise. First the signal is divided in overlapping segments and the amount of overlapping might be changed as desired by the user. If the all the data points in the signal are part of two different segments the overlapping is maximized. This is referred to as a 50 % overlap. If there is no overlap assigned by the user one returns to Bartlett's method. After creating overlapping segments, the segments will be altered by a so-called window function which helps reduce the noise but generally gives more weight to the data at the center of the segment and less to the data at the edges, thus the reason for the data overlap. Once the segments are overlapped and "windowed" the periodogram of each is found and then the periodograms are averaged. The results is the graph of intensity or power spectral density of the signal as a function of frecuency [6, 7, 8].

| Case 2 (J $\approx$ 1.05, P$_r$ = 1.05)	T [K]	$\dot{m}$ [g.s^{-1}]	ρ [kg.m^{-3}]	u [m.s^{-1}]	Re
outer jet	152	1.57	101	5.95	41 600
inner jet	117	0.289	590	2.4	15 000

Table 3.1: Injection conditions for the outer jet and for the inner jet corresponding to the cases "N2" (simulation) & "near2" (experiment). J is the momentum flux ratio, P$_r$ is the reduced pressure and $\dot{m}$ denotes the mass flow rate.

Case 6 (J $\approx$ 3.0, P$_r$ = 1.05)	T [K]	$\dot{m}$ [g.s^{-1}]	ρ [kg.m^{-3}]	u [m.s^{-1}]	Re
outer jet	183	2.69	73.1	14.1	64 800
inner jet	126	0.292	420	3.4	25 000

Table 3.2: Injection conditions for the outer jet and for the inner jet corresponding to the cases "N6" (simulation) & "near6" (experiment). J is the momentum flux ratio, P$_r$ is the reduced pressure and $\dot{m}$ denotes the mass flow rate.

For the simulation data the signals analyzed were radial velocity, axial velocity and pressure. Spectral graphs representing the power spectral density of these signals as a function of frequency at a given downstream location from the inner jet exit were obtained. Spectral maps were built showing contours of the signal power spectral density at different frequencies for all downstream locations. The graphs and maps obtained from simulation data are shown in Sections 6.3 and 7.3 in part I of this report and most of them are reproduced in this part of the report for comparison.

In the case of experimental measurements, the signal consisted of the intensity of light in the recorded images. The same procedure followed to extract the power spectral density from simulation data was used with the experimental results. Spectral maps were also built showing contours of the signal power spectral density at different frequencies for all downstream locations. In order to compare results with experiments, the same axes selected to analyze the simulation data were selected for the spectral analysis of the experimental data. An image showing the axes superimposed to a shadowgraph of the coaxial jet is shown in Fig. 3.3.a while the image shown to illustrate the axes in section 7.3 in part I of this report is reproduced in Fig. 3.3.b below.
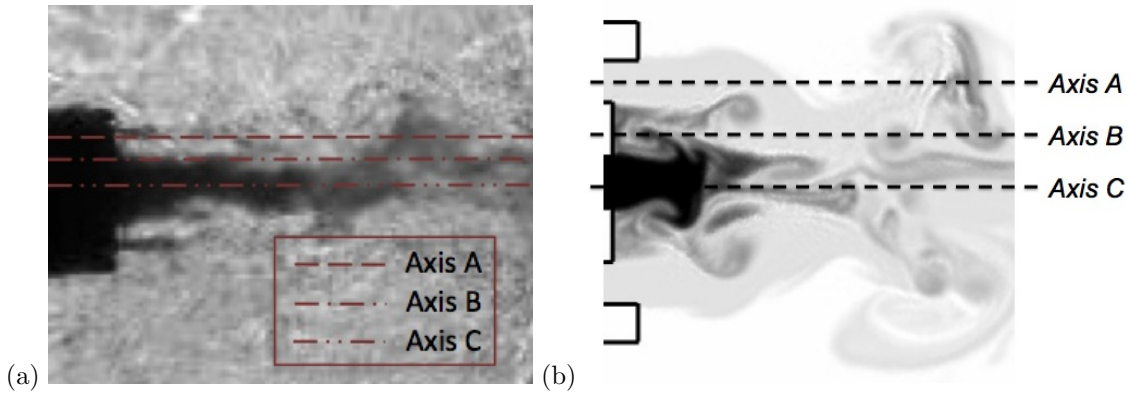
Figure 3.3: Positions of the three axial lines used in the spatial spectral analysis. (a) Experimental case "near6". (b) Simulation case "N6$^{2\%}_{\phi=0}$".

To apply Welch's method both the simulation and experimental data sets were segmented in M overlapping blocks with a 50 % overlap to minimize variance problems. Because the number of samples is limited the averaging is carried out over $M = 8$ blocks in the outer flow region and on $M = 4$ blocks in the inner jet region for the simulations and over $M = 8$ blocks for all experimental data. The frequency resolution corresponding to the different locations along the axes shown in Fig. 3.3 is given in Table 3.3.

$St = (fl)/u$	l (Fig. 3.1.b)	u	Axis (Fig. 3.3)	Δf [Hz]
St^i	d_i (0.51 mm)	u_i	C	N2: 187; N6: 125; near2 & near6: 200
St^l	l_l (0.54 mm)	u_e	B	N2: 375; N6: 250; near2 & near6: 200
St^e	h_e (0.41 mm)	u_e	A	N2: 375; N6: 250; near2 & near6: 200

Table 3.3: Definition of characteristic Strouhal numbers. The characteristic length and velocity l and u are given in the second and third columns. The frequency f corresponds to the power spectral density maximum from simulations and experiments. Δf is the frequency resolution.

Chapter 4

Results and discussion

4.1 Spectral analysis of cases without acoustic modulation

For cases without acoustic modulation, it is of interest to identify any periodicities in the flow dynamics. The spectral maps of these cases thus shed some light into the natural modes that might be present in the coaxial jet's dynamics. This information is useful when identifying modes that might be enhance by the modulation frequency or to find approximate Strouhal numbers for the natural modes present. In the following figures the spectral maps of transcritical cases "near2" and "near6" are shown. The plots show frequency in Hertz versus distance downstream the coaxial injector's exit in inner jet diameters (d_i) where one d_i corresponds to 0.51 millimeters.
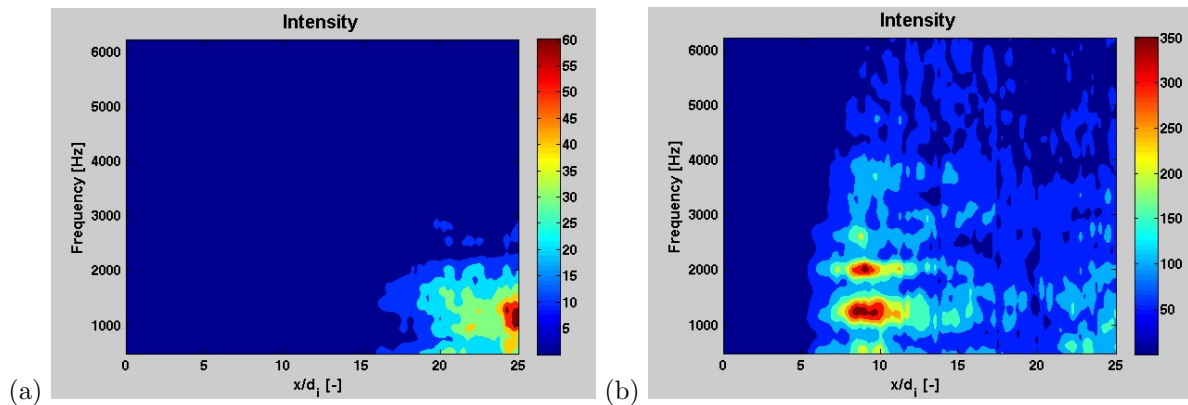
Figure 4.1: Spectral maps of experimental cases "near2" and "near6" without acoustic modulation along the inner jet center axis or axis C as shown in Fig. 3.3. (a) Case "near2". (b) Case "near6".

In the spectral maps we can observe the different values that the intensity of the signal reaches. In Fig. 4.5.a along the central axis we observe a mode of approximately 1.2 kHz towards the end of the image (around 25 d_i downstream) for case near2, this might appear as a strong mode but its intensity is low compared to the maximum value in Fig. 4.5.b. This map presents modes near 1.3 and 2.1 kHz between 8 to 10 d_i downstream. The location of the modes follows the same trend as the length of the inner jet

core with a lower momentum flux ratio case such as near2 having a mode present further downstream as compared to the higher momentum flux ratio case near6
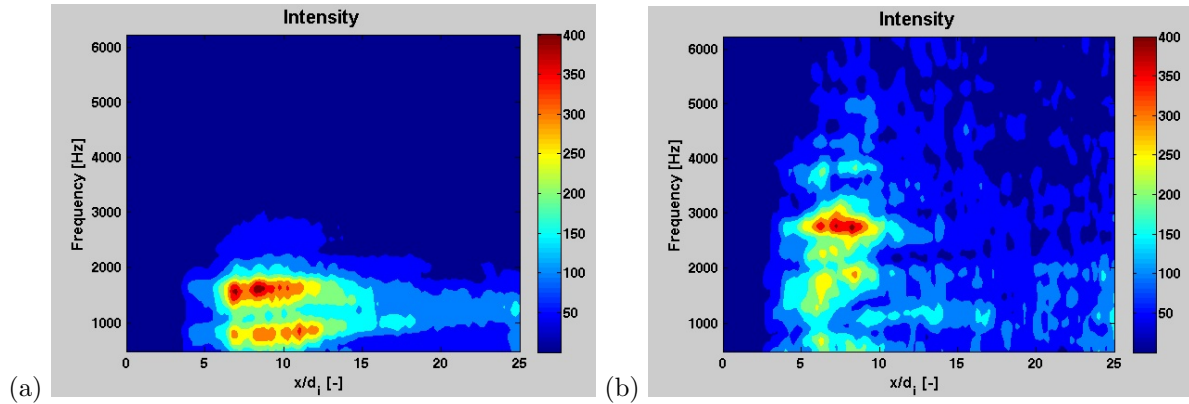
Figure 4.2: Spectral maps of experimental cases "near2" and "near6" without acoustic modulation along the center of the inner jet post or axis B as shown in Fig. 3.3. (a) Case "near2". (b) Case "near6".

The maps in Fig. 4.8 show different dynamics then the ones in the previous image. Now the maximum intensity of the signal for both cases is similar and the low momentum flux ratio case shows a mode near 1.7 kHz between 6 and 8 d_i downstream whereas the higher momentum flux ratio case shows a mode near 2.8 kHz also around 7 and 8 d_i downstream. A natural mode near 3 kHz is always interesting since modulation has been applied at this frequency and certain phenomena could be better understood if we find there is coupling between a natural mode and the imposed acoustic forcing.
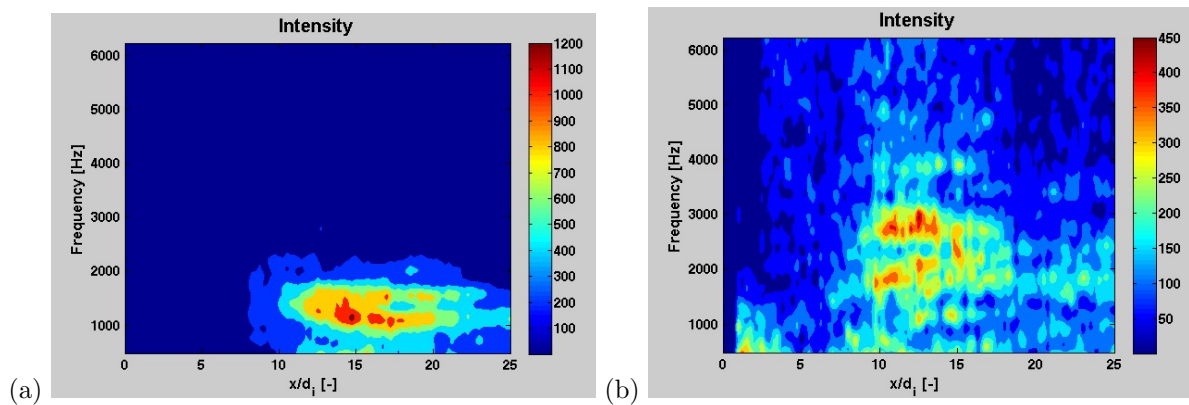

Figure 4.3: Spectral maps of experimental cases "near2" and "near6" without acoustic modulation along the outer jet center axis or axis A. as shown in Fig. 3.3. (a) Case "near2". (b) Case "near6".

For the last two maps in Fig. 4.5 we focus on the dynamics of the outer jet axis. We notice that the maximum intensity of the signal for case "near2" is higher than any of the other maps we have seen so far. The mode with such intensity is located 15 d_i downstream the inner jet exit and at a frequency of 1.2 kHz. More interestingly, the case "near6" features a region of maximum intensity very close to 3.0 kHz; however, the rest of the map shows regions of high intensity at several locations and frequencies, which make a clear mode difficult to distinguish.

70
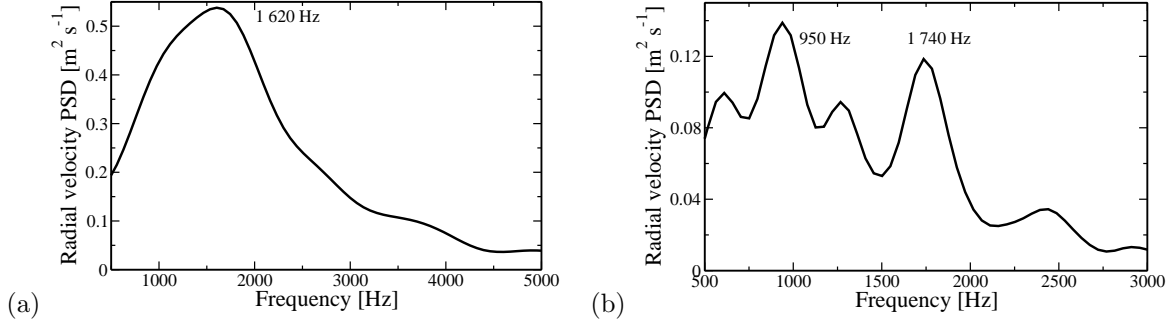
Figure 4.4: Power spectral density of radial velocity for simulation data. (a) Case "N2" in the mixing layer behind the inner lip (this spectrum is found 3 d_i downstream along the B axis as shown in Fig. 3.3). (b) Case "N6" in the inner jet centerline (this spectrum is found 2 d_i downstream along the C axis as shown in Fig. 3.3).

The two graphs shown in Fig. 4.4 show results without acoustic forcing found from simulation data that have similar trends to those obtained from the experimental images. The first graph (Fig. 4.4.a) shows a distinctive wide peak at a location along the center of the inner jet post (B axis) near 1.6 kHz for the simulation case "N2" which is the equivalent to the experimental case "near2" which shows a mode which is not as wide but still strong near this frequency too in Fig. 4.8.a. The main difference however is the physical location of the mode. In the simulation we find the mode at a location 3 d_i downstream while the experimental results show a mode predominantly between 6 to 10 d_i downstream the injector exit.

In Fig. 4.4.b there are two peaks that are clearly visible near 0.95 and 1.7 kHz. These peaks are close to the same modes found in the spectral map of Fig. 4.5 where we observe maximum intensities near 1.3 and 2.1 kHz. Again, for the simulation we find the location of these nodes at 2 d_i downstream while the experimental ones are located between 8 to 10 d_i downstream. Since the location of the probe for the simulation case is related to the end of the potential core as explained in section 6.3.1 in part I, the phenomena in both cases might be equivalent since the end of the dark core for the experimental case was measured at 6 d_i downstream the injector.

4.2   Spectral analysis of a case with acoustic modulation

Spectral maps of experimental case "near6" and simulation case "N6" with acoustic modulation are presented in this section. The spectral information shows a clear influence of the acoustic modulation with maps with very large maximum intensities and modes that correspond to the excitation frequency. This is further proof of the strong effect that the acoustic modulation has on the flow even if the perturbation is only a small fraction (1% or 2% maximum) of the mean values.
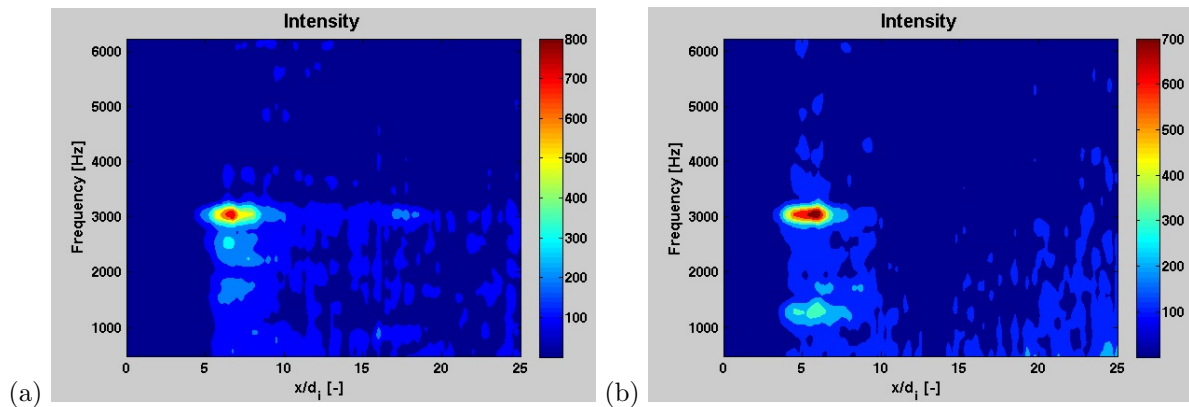
Figure 4.5: Spectral maps of experimental case "near6" with acoustic modulation along the inner jet centerline or axis C as shown in Fig. 3.3. (a) In-phase modulation. (b) Out-of-phase modulation.
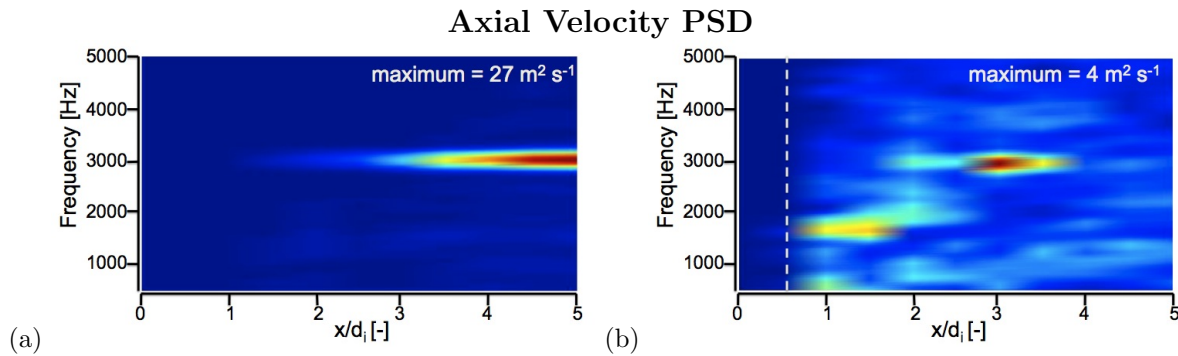
Figure 4.6: Spectral maps of axial velocity along the inner jet centerline or axis C ($r = 0$) for (a) Case "N6$_{\phi=0}^{2\%}$" (in-phase modulation) and (b) Case "N6$_{\phi=\pi}^{2\%}$" (out-of-phase modulation).

In the first set of maps the dynamics along the central axis are shown. For the case in Fig. 4.5.a with acoustic modulation in phase a mode just over 3.0 kHz can be observed between 6 and 7 d_i. This is basically the same mode observed for the case with out-of-phase modulation in Fig. 4.5.b. Interestingly, the modes are located at the location downstream where the inner jet dark core ends when no acoustic modulation is applied. This means that the zone where the last dense packets of fluid exist when no acoustic excitation is applied now becomes a region where intense flow periodicities and mixing take place. In fact, if one looks at the spectral maps from the simulation data, on observes modes at the forcing frequency of 3 kHz that reach a maximum 5 d_i downstream for the axial velocity signal when the

72

Radial Velocity PSD
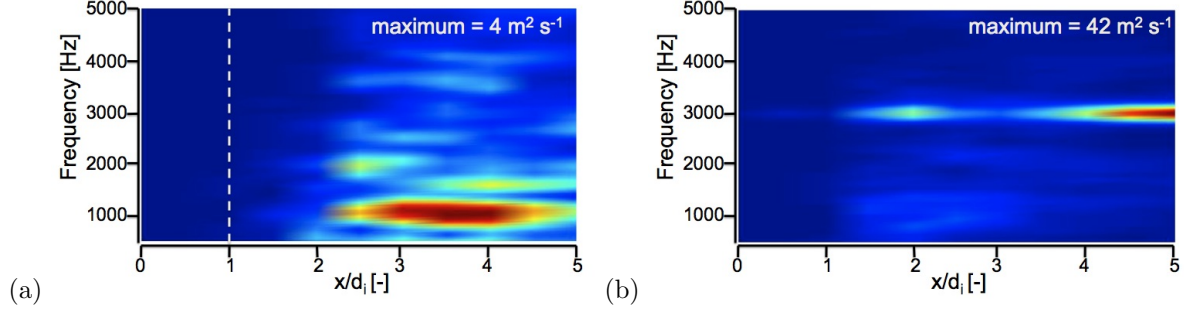
Figure 4.7: Spectral maps of radial velocity along the inner jet centerline or axis C ($r = 0$) for (a) Case "N6$^{2\%}_{\phi=0}$" (in-phase modulation) and (b) Case "N6$^{2\%}_{\phi=\pi}$" (out-of-phase modulation).

modulation is in phase (Fig. 4.6.a) and for the radial velocity signal when modulation is out of phase (Fig. 4.7.b). Both images clearly show a mode that might extend downstream beyond the 5 d_i shown which would correspond very closely with the mode observed in Fig. 4.5 for the experimental cases.
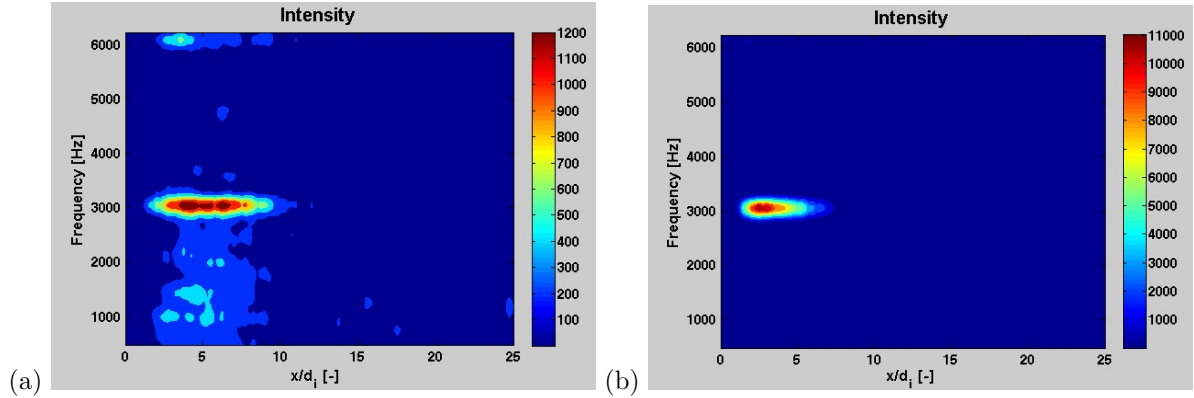

Figure 4.8: Spectral maps of experimental case "near6" with acoustic modulation along the center of the inner jet post or axis B as shown in Fig. 3.3. (a) Modulation in phase. (b) Modulation out of phase.

The spectral map in Fig. 4.8.a also shows a mode at the same frequency, slightly over 3.0 kHz, as the one shown in the previous images. This is expected since the modulation applied was the same for all conditions. The interesting feature of this image is the "distance of influence" of the mode which extends from 3 to 7 d_i downstream. Such a region could indicate that a larger "periodic mass transfer" or recirculation zone is created just after the inner jet post. For the out-of-phase condition in Fig. 4.8.b, however, no such band exists but instead there is a point, which highlights a mode with a level of intensity an order of magnitude larger than its in-phase counterpart. This very strong mode shares the same frequency though it is located between 2 and 3 d_i downstream. This could be the consequence of strong transversal velocity oscillations acting near the exit of the injector and quickly mixing the dense inner jet shortly afterwards. An interesting feature of these last two spectral maps has to do with the region where the strongest modes appear. Up to this point no previous experimental spectral map had shown any significant activity in the region between 0 and 5 d_i downstream except maybe for the case "near 6" along the outer jet centerline in Fig. 4.11.b where there is some activity in the sub 1kHz range

73

Axial Velocity PSD

(a)

(b)
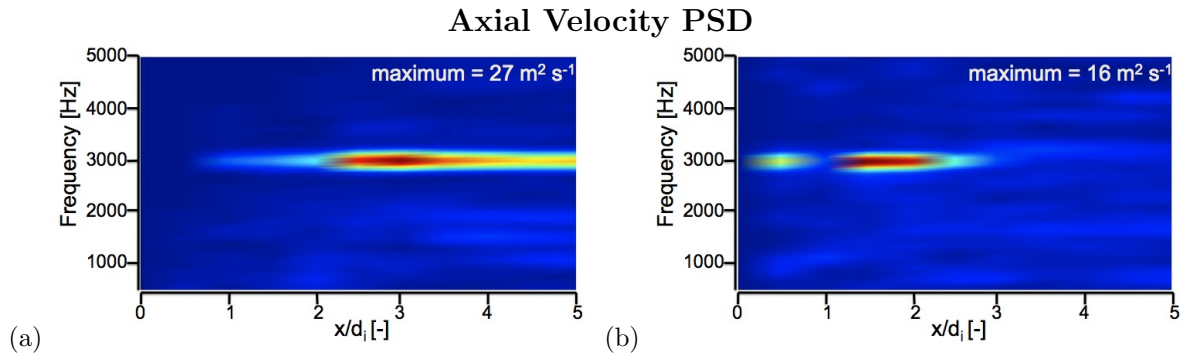
Figure 4.9: Spectral maps of axial velocity along the inner jet post centerline or axis B ($r = d_i/2 + l_l/2$) for (a) Case "N6$^{2\%}_{\phi=0}$" (in-phase modulation) and (b) Case "N6$^{2\%}_{\phi=\pi}$" (out-of-phase modulation).

Radial Velocity PSD

(a)

(b)
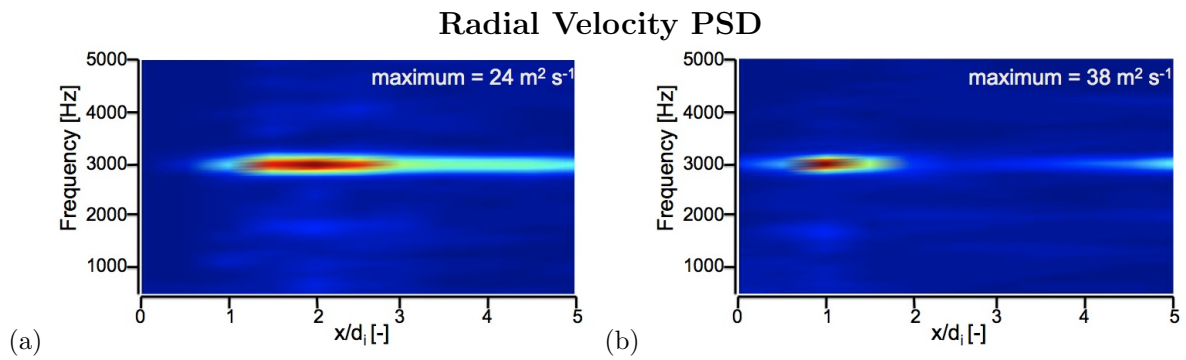
Figure 4.10: Spectral maps of radial velocity along the inner jet post centerline or axis B ($r = d_i/2 + l_l/2$) for (a) Case "N6$^{2\%}_{\phi=0}$" (in-phase modulation) and (b) Case "N6$^{2\%}_{\phi=\pi}$" (out-of-phase modulation).

and more recently in our out-of-phase modulation case "near2" along the inner jet centerline in Fig. 4.5.b where the 3kHz mode starts showing around 4 d_i downstream. Now we have two very strong modes, specially the one present when modulation is out of phase in the region between the two jets shortly before the jets exit the injector and start mixing. To confirm this new trend, the spectral maps can be compared with the spectral data from simulations. The similarities could not be closer since the radial velocity signal for the in-phase modulation case (4.10.a) shows a relatively broad mode starting just after 1 d_i and continuing until 3 d_i and extending weakly into 5 d_i downstream; however, when the radial velocity mode loses strength the axial velocity one predominates as seen in Fig. 4.9.a and extends until the end of the map. This "combined" broad mode is similar to the broad mode observed in experimental case in Fig. 4.8.a. The same comparison between simulation and experiment could be drawn by observing the case "N6" under out-of-phase modulation, where the combined regions of influence of the axial and radial velocity modes in Figs. 4.10.b and 4.10.b, result in a larger mode extending from approximately 0.5 to 2.5 d_i downstream. This is a very close match to the region of influence of the mode found from case "near6" under out-of-phase modulation and shown in Fig. 4.8.b.

(a)   (b)
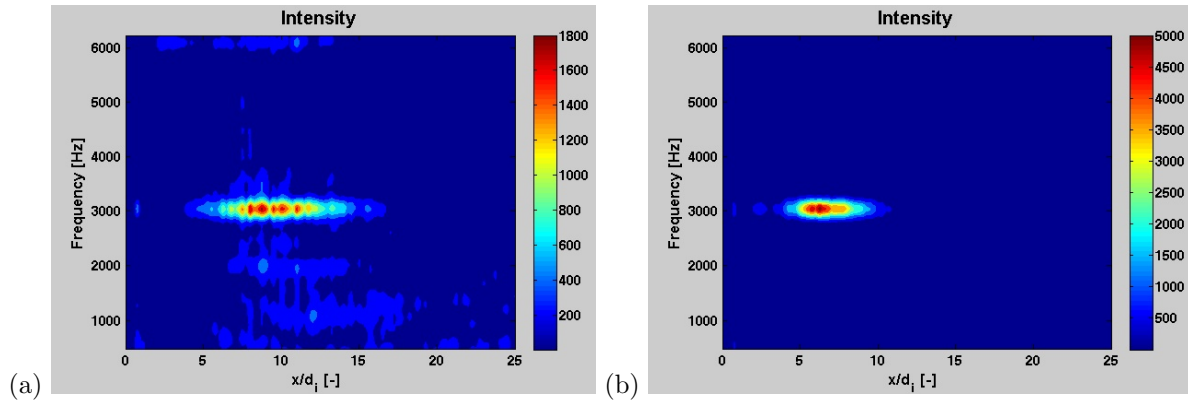
Figure 4.11: Spectral maps of experimental case "near6" with acoustic modulation along the outer jet center axis or axis A. as shown in Fig. 3.3. (a) In-phase modulation. (b) Out-of-phase modulation.


(a)   (b)
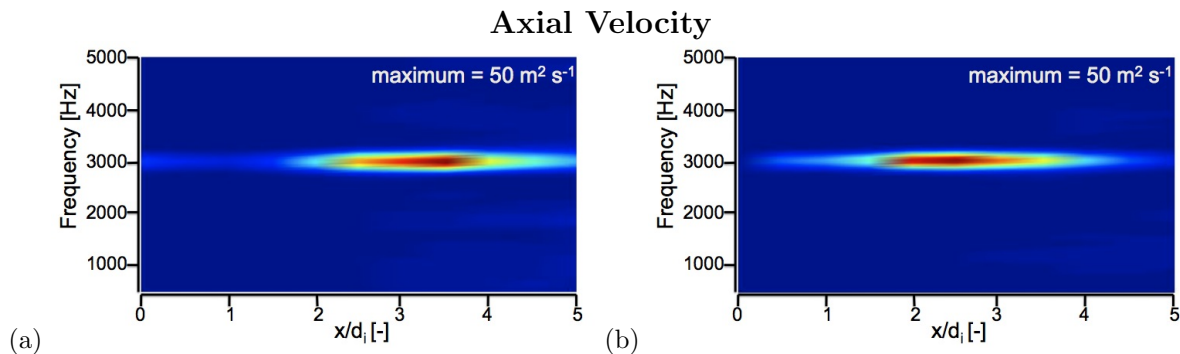
Figure 4.12: Spectral maps of axial velocity along the outer jet flow centerline or axis A ($r = d_i/2 + l_l + h_e/2$) for (a) Case "N6$_{\phi=0}^{2\%}$" (in-phase modulation) and (b) Case "N6$_{\phi=\pi}^{2\%}$" (out-of-phase modulation).

The last two spectral maps are shown in Fig. 4.11 and they represent the center region of the annular jet. Both conditions present phenomena at the excitation frequency of 3 kHz. The condition with in-phase

Radial Velocity

(a)   (b)
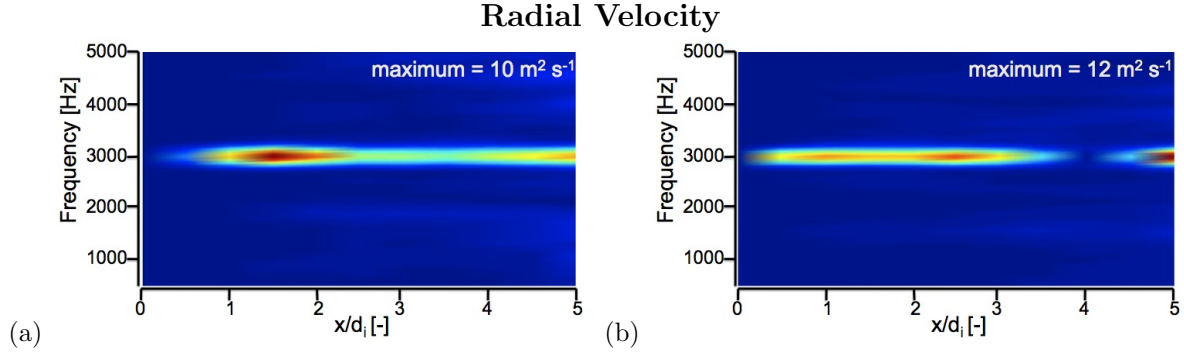
Figure 4.13: Spectral maps of radial velocity along the outer jet flow centerline or axis A ($r = d_i/2 + l_l + h_e/2$) for (a) Case "N6$_{\phi=0}^{2\%}$" (in-phase modulation) and (b) Case "N6$_{\phi=\pi}^{2\%}$" (out-of-phase modulation).

modulation shows again a mode that is spread over a few d_i but the mode is farther downstream than the one in Fig. 4.8.a. The mode is thus now located between 8 and 11 d_i and with similar overall strength but now with 50% larger maximum intensity. Similarly, the out-of-phase condition presents a very well defined mode as that shown in Fig. 4.8.b but now between 6 and 7 d_i downstream. This trend might give us an idea of the direction the strongest interactions follow as they are convected downstream. Also wider spread of the modes along the interrogation line is observed when the modulations are in-phase for axes A and B as compared to the spread of the modes when the modulations are out-of-phase. The periodicities in the outer layers of the flow are apparently more localized when the flow has large velocity fluctuations at its center. The simulation results in Fig. 4.12 support the already expected findings that strong modes observed at the modulation frequency and they also show combined broad modes; however, their locations differ, since the nodes from the simulation spectral maps show stronger nodes between 2 and 4 d_i downstream and the spectral maps from experiments show these modes in the 6 to 10 d_i downstream zone.

Chapter 5

Conclusions

The study of the spectral content of the experimental images is useful to further support the findings drawn from direct image processing and simulation results. This analysis provides another tool to interrogate the behavior of the flow. It is an effective manner to identify periodicities which otherwise could go unnoticed. For instance, the low momentum flux ratio case studied, "near2" featured modes in the 1 to 2 kHz range at different locations downstream the jet exit when no acoustic modulation was applied. This is an interesting information when trying to decide if the imposed frequency during acoustic forcing might be exciting existing modes. This could make a difference in previous experimental findings showing that small acoustic perturbations lead to large dark core length reductions and enhanced mixing, since it would not be the same it the perturbations are imposed at a resonant frequency or mode of the coaxial jet.

Another instructive feature of this analysis is the close agreement between experimental and simulation data when comparing spectral maps of the cases "near6" and "N6" with acoustic modulation even when the signals compared were not the same (light intensity from each pixel for the experimental data and radial and axial velocity for the simulation data). The expected forcing frequency of 3kHz was clearly present in all spectral maps obtained from experimental data and these findings were in agreement with the spectral maps from the simulation data, not only qualitatively but also qualitatively in regard to the distance downstream from the injector at which the modes were found. These is more significant given the fact that the spectral information of the non-acoustic case did not agree to the same extent. On the other hand, the comparison between the experimental data and simulation data for the case without acoustics was not as extensive.

Further analysis of experimental and simulation data could be performed to identify periodicities and relate them to the observed features of the flow. The spectral data could be useful to identify characteristic modes of the coaxial jet and obtain the associated non-dimensional frequencies (Strouhal numbers). Then a map showing the trends of these modes as various coaxial jet parameters are changed could be created. This could help elucidate certain types of behavior observed in recent experimental results, such as the inversion of the effects of in-phase versus out-of-phase modulation for different types of injectors [9] and extreme reduction and even obliteration of the inner jet core when forced at certain frequencies [9, 10].

Bibliography

[1] Schmitt, T., Rodriguez, J., Leyva, I. A., Candel, S., "Experiments and Numerical Simulation of Mixing under Supercritical Conditions", *submitted to Physics of Fluids*.

[2] Sreenivasan, K. R., Raghu, S., Kyle, D., "Absolute Instability in Variable Density Round Jets", *Experiments in Fluids, 7*, (1989) 309-317.

[3] Raynal, L., Harion, J.-L., Favre-Marinet, M., Binder, G., "The Oscillatory Instability of Plane Variable-Density Jets", *Physics of Fluids, 8*, (1996) 993-1006.

[4] Poinsot, T. J., Trouvé, A. C., Veynante, D. P., Candel, S. M., Esposito, E. J., "Vortex-Driven Acoustically Coupled Combustion Instabilities", *Journal of Fluid Mechanics, 177*, (1987) 265-292.

[5] Engelberg, S., **Digital Signal Processing**, *Springer, 1st ed.*, (2010).

[6] Proakis, J. G., Manolakis, D. K., **Digital Signal Processing: Principles, Algorithms and Applications**, *Prentice Hall, 3rd ed.*, (1995).

[7] Welch, P. D., "The Use of Fast Fourier Transform for the Estimation of Power Spectra: A Method Based on Time Averaging over Short, Modified Periodograms", *IEEE Transactions on Audio Electroacoustics, 15*, (1967) 70-73.

[8] Oppenheim, A. V., Schafer, R. W., **Digital Signal Processing**, *Prentice Hall*, (1975).

[9] Rodriguez, J. I., "Acoustic Excitation of Liquid Fuel Droplets and Coaxial Jets", *Ph.D. Thesis, UCLA* (2009).

[10] Graham, J. J., Leyva, I. A., Rodriguez, J. I., Talley, D., "On the Effect of a Transverse Acoustic Field on a Flush Shear Coaxial Injector", *45th AIAA/ASME/SAE/ASEE Joint Propulsion Conference and Exhibit*, AIAA 2009-5142.

Nomenclature

d_i inner jet diameter

Δf resolution frequency of spectral data

e subscript or superscript for outer jet flow

h_e outer jet thickness

i subscript or superscript for inner jet flow

f frequency, characteristic frequency

Hz   Hertz or cycles per second [m^{-1}]

J Momentum flux ratio ($J = \rho_e u_e^2 / \rho_i u_i^2$)

kHz   kiloHertz or 1000 cycles per second [10^3 m^{-1}]

l characteristic length, subscript for inner jet post or lip

LES   Large Eddy Simulation

l_l inner jet post thickness

M   Number of blocks used for spatial averaging

$\dot{m}$ mass flow rate

$\text{N6}_{\phi=0}^{2\%}$ simulation case N6 with 2% amplitude and in-phase modulation

$\text{N6}_{\phi=\pi}^{2\%}$ simulation case N6 with 2% amplitude and out-of-phase modulation

P pressure

P_c critical pressure

P_r reduced pressure ($P_r = P/P_c$)

PSD   Power Spectral Density

r radial (transversal) distance from the center axis of the flow

Re Reynolds Number

ρ density

St Strouhal Number

T Temperature

u velocity, characteristic velocity

Part III

Direct Numerical Simulation of Flows under Transcritical Conditions

Calculations of transcritical flows using an adapted direct numerical simulation code

Authors: J. Rodriguez[1], J. Caudal[1], B. Fiorina[1], N. Darabiha[1], S. Candel[1], A. Coussement[1,2], and O. Gicquel[1,2]

[1]EM2C, CNRS, École Centrale Paris, 92295 Châtenay-Malabry, France,
[2]FSA, Université Libre de Bruxelles, 1050, Brussels, Belgium.

List of Figures

Chapter 1

Abstract

The purpose of this study is to develop and validate a direct numerical simulation (DNS) code used to analyze the behavior of transcritical flows. The code, which is intended to become a general purpose DNS code with an emphasis on combustion, has been developed by the numerical combustion group at the EM2C laboratory of École Centrale Paris. It comprises different thermodynamic modules which range from simple air calculations without combustion to complex real gas thermodynamics of flows close to the critical point of the substance. An initial validation of this code is first carried out by observing the evolution of an initial temperature profile with a basic Gaussian shape. This validation process provides the order of the numerical scheme. The code is next used to test situations that will be of interest to the transcritical evolution of shear flows in parts I and II of this report. The case of a two-dimensional mixing layer is envisaged. Initial calculations are carried out in the case of a two-dimensional (2D) problem in which two streams form an initial vortex sheet. The results of this analysis are used to provide a picture of how DNS tools can be used to study transcritical behavior in these types of flows.

Chapter 2

Introduction

Direct Numerical Simulation (DNS) is a useful modeling tool when the geometry of the problem is not complex and the difference between the largest and smallest scales of the flow is not too large. In practice, very few applications have the characteristics mentioned above so DNS is often used to give the researcher the opportunity to study more in depth one characteristic of a more complex problem or to help develop models that can be later used in Large Eddy Simulations (LES) to handle complex geometries such as those required in aircraft and space propulsion problems.

Research involving DNS for supercritical flows has been done by Okong'o and Bellan [1, 2] on the characteristics of high pressure transitional flows. They formulate their equations according to fluctuation-dissipation theory which adds the thermal diffusion factor to the list of transport properties playing a role in high pressure systems. They observe that dissipation is mostly due to species mass flux and turbulence models should focus in this property rather than the momentum flux. Selle *et al.* [4] analyze this transitional supercritical mixing layer in detail with DNS to observe the behavior of the small scales of the flow and compare that to the subgrid-scale (SGS) closure models used in LNS techniques. Selle and Ribert also investigate the impact of the equation of state used in DNS on turbulence models for supercritical flows [3].

At the EM2C laboratory at École Centrale Paris, the Numerical Combustion Group has developed a code nicknamed YWC (Yes We Can) which uses DNS to investigate different types of problems. The code is fully parallel and has many options and functionalities that can be set up by the user. Among them are the posibility of performing a calculation in one, two or three dimensions. The type of numerical scheme used (centered, compact) and the possibility to use filtering. The user also can select which boundary conditions to use: periodic, inlet, outlet, wall, adiabatic wall and even there is an option to create a special boundary condition if a more complex setup is needed.

In particular, the code YWC features different thermodynamic modules to solve various types of problems. The simplest is the module AIR, which only deals with this fluid (air) as a single species and for cases with no chemical reactions. A second module, SIMPLE CHEMISTRY, deals with reactions considering only a few species. This simple chemistry option allows for faster calculation of problems where the details of the reaction are not an issue. The other three modules deal with either perfect or real gas thermodynamic problems. The basic one, REGATH, features more species and handles more complex combustion problems. A "light" version called REGTAH LITE was developed to decrease calculation costs when not all the functionality of REGATH was needed. A final module, REGATH TRC was

conceived for problems dealing with fluids near their critical point. It is this last module which is better suited to study transcritical flow problems such as the ones described in this report.

Chapter 3

Methods, assumptions and procedures

3.1 YWC governing equations

The direct numerical simulation tool YWC solves the balance of mass, species, momentum and energy equations. These are partial differential equations which require extensive computational capability if direct calculation is desired, especially for flows with large differences between their largest and smallest scales (high Re flows).

Conservation of mass

$$\frac{\partial \rho}{\partial t} = -\frac{\partial \rho u_i}{\partial x_i} \tag{3.1}$$

Conservation of species

$$\frac{\partial \rho Y_k}{\partial t} = -\frac{\partial \rho u_i Y_k}{\partial x_i} + \dot{\omega}_k + \frac{\partial}{\partial x_i}\left(\rho D_k \frac{\partial Y_k}{\partial x_i}\right) \tag{3.2}$$

where subscript k refers to the species ($k \in [1, N]$)

Conservation of momentum

$$\frac{\partial \rho u_j}{\partial t} = -\frac{\partial \rho u_i u_j}{\partial x_i} - \frac{\partial p}{\partial x_j} + \frac{\partial \tau_{ij}}{\partial x_i} \qquad j \in [1,3] \tag{3.3}$$

τ_{ij} is the (i, j) element of the viscous tensor τ, which is calculated by :

$$\tau_{ij} = \mu\left(\frac{\partial u_i}{\partial x_j} + \frac{\partial u_j}{\partial u_i}\right) - \frac{2}{3}\left(\mu \frac{\partial u_k}{\partial x_k}\delta_{ij}\right) \tag{3.4}$$

$$S_{ij} = 1/2 \left(\frac{\partial u_i}{\partial x_j} + \frac{\partial u_j}{\partial u_i} \right) \tag{3.5}$$

$$S_{11} = \frac{\partial u}{\partial x} \tag{3.6}$$

$$S_{22} = \frac{\partial v}{\partial y} \tag{3.7}$$

$$S_{33} = \frac{\partial w}{\partial z} \tag{3.8}$$

$$S_{12} = S_{21} = 1/2 \left(\frac{\partial u}{\partial y} + \frac{\partial v}{\partial x} \right) \tag{3.9}$$

$$S_{13} = S_{31} = 1/2 \left(\frac{\partial u}{\partial z} + \frac{\partial w}{\partial x} \right) \tag{3.10}$$

$$S_{23} = S_{32} = 1/2 \left(\frac{\partial v}{\partial z} + \frac{\partial w}{\partial y} \right) \tag{3.11}$$

$$|S| = (\mathbf{S} : \mathbf{S})^{1/2} \tag{3.12}$$

$$= \left(S_{11}^2 + S_{22}^2 + S_{33}^2 + 2S_{21}^2 + 2S_{13}^2 + 2S_{21}^2 \right)^{1/2} \tag{3.13}$$

Conservation of energy

$$\frac{\partial \rho e}{\partial t} = -\frac{\partial \rho u_i e}{\partial x_i} - \frac{\partial p u_i}{\partial x_i} + \frac{\partial \tau_{ij} u_j}{\partial x_i} - \frac{\partial q_i}{\partial x_i} \tag{3.14}$$

3.2 YWC numerical aspects

3.2.1 Temporal discretization

A numerical solver needs to discretize a domain in space and also in time. The method used to discretize the time domain in the YWC solver is the 4th order Runge-Kutta scheme. For the following differential equation :

$$\frac{\partial \rho}{\partial t} = f(t, \rho)$$
$$\rho(t_0) = \rho_0$$

if we know the value of $\rho_n = \rho(t_n)$, this method consists in calculating the new variable $\rho_{n+1} = \rho(t_n + \Delta t)$ with the following procedure :

$$\rho_{n+1} = \rho_n + \Delta t \ K \tag{3.15}$$

K is an evaluated value of the slope of $\rho(t)$. For 4th order Runge-Kutta, we calculate K with a four-step process :

$$K = \frac{1}{6}(k_1 + 2k_2 + 2k_3 + k_4) \tag{3.16}$$

This formula introduces four coefficients, k_1, k_2, k_3 and k_4 defined as following :

$$k_1 = f(t_n, \rho_n) \qquad (3.17)$$

$$k_2 = f(t_{n+\frac{1}{2}}, \rho_n + \frac{\Delta t}{2}k_1) \qquad (3.18)$$

$$k_3 = f(t_{n+\frac{1}{2}}, \rho_n + \frac{\Delta t}{2}k_2) \qquad (3.19)$$

$$k_4 = f(t_{n+1}, \rho_n + \Delta t\, k_3) \qquad (3.20)$$

k_1 is the slope of $\rho(t)$ evaluated at the beginning of the interval (t_n).

k_2 is the slope of $\rho(t)$ evaluated at the middle of the interval $(t_{n+\frac{1}{2}})$, using the value of k_1 to calculate $\rho_{n+\frac{1}{2}}$.

k_3 is the slope of $\rho(t)$ evaluated at the middle of the interval $(t_{n+\frac{1}{2}})$, using the value of k_2 to calculate $\rho_{n+\frac{1}{2}}$.

k_4 is the slope of $\rho(t)$ evaluated at the end of the interval (t_{n+1}), using the value of k_3 to calculate ρ_{n+1}.

3.2.2 Spatial discretization

To solve the equations in space there are three different schemes available. Two of them are centered (4th and 6th order) and the third is a 6th order compact scheme. As an example we assume that $\varphi = \varphi(x)$, and we are estimating the value of $\frac{\partial \varphi}{\partial x}$. This description is relevant for computational domains with uniform grids.

For the spatial derivatives using centered scheme, the grid spacing Δx has to be constant. The discretized equations are:

4th order

$$\frac{\partial \varphi}{\partial x}(x_i) = \frac{\varphi(x_{i-2}) - 8\varphi(x_{i-1}) + 8\varphi(x_{i+1}) - \varphi(x_{i+2})}{12\,\Delta x} \qquad (3.21)$$

6th order

$$\frac{\partial \varphi}{\partial x}(x_i) = \frac{-\varphi(x_{i-3}) + 9\varphi(x_{i-2}) - 45\varphi(x_{i-1}) + 45\varphi(x_{i+1}) - 9\varphi(x_{i+2}) + \varphi(x_{i+3})}{60\,\Delta x} \qquad (3.22)$$

When the values of φ for adjacent points are not available, such as in the limits of the domain for non-periodic boundary conditions the spatial derivatives need to be computed with a uncentered formulation.

For the compact scheme the following method described by Lele [5] is used:

$$a_i \varphi'_{i-1} + b_i \varphi'_i + c_i \varphi'_{i+1} = d_i \qquad (3.23)$$

where a_i, b_i, c_i are constant coefficients and d_i is a variable that depends on the value of φ at point x_i and its neighbors. Several compact schemes can be defined through the choice of the coefficients a_i, b_i, c_i, and the variable d_i [5]. To achieve a 6th order scheme, however, the following values are used:

6th order

$$\frac{1}{3}\varphi'_{i-1} + \varphi'_i + \frac{1}{3}\varphi'_{i+1} = \frac{14}{9}\left(\frac{\varphi_{i+1} - \varphi_{i-1}}{2\Delta x}\right) + \frac{1}{9}\left(\frac{\varphi_{i+2} - \varphi_{i-2}}{4\Delta x}\right) \tag{3.24}$$

Similar to the centered scheme, the compact scheme uses values from adjacent nodes. When these nodes are not available, for instance at the boundaries of the domain, an alternative formulation is specified.

Chapter 4

Results and discussion

4.1 Comparison of the thermodynamic modules

As stated previously, the code YWC gives the user the possibility to choose from various thermodynamic modules depending on the requirements of the problem. The modules to be considered for the treatment of problems involving real gas thermodynamics are REGATH and TRC. It is important to know the capability of each of these modules to represent as accurately as possible the properties of a fluid at transcritical conditions. Therefore, in order to compare the different modules, a plot of density as a function of temperature for nitrogen at a given pressure was used. The reference data was obtained from the online NIST Standard Reference Database [6].
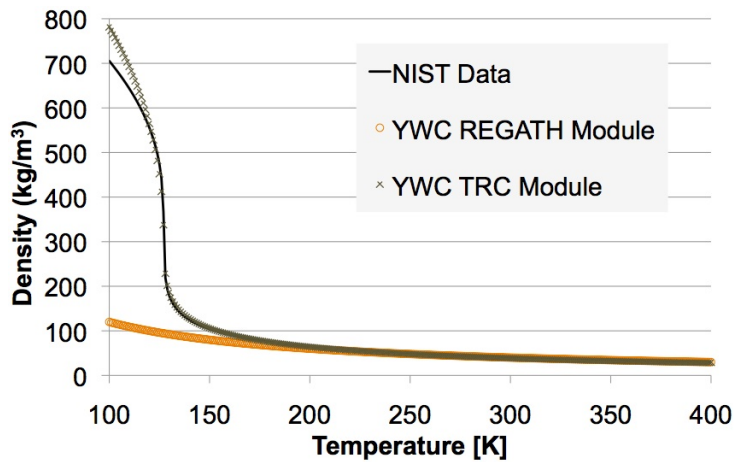

Figure 4.1: Nitrogen thermodynamic values obtained for a pressure of **3.56 MPa** ($P_r = 1.05$) with the two real gas thermodynamic modules of the code YWC and the values from the NIST Standard Reference Database.

It is clear in Fig. 4.1 that the module REGATH starts departing from the actual transcritical behavior of nitrogen when the temperature decreases below 200 K. The module TRC, created specifically for this

kind of high pressure, transcritical environments, follows the reference curve until 120 K, where it starts to deviate. This plot is useful to know which ranges of temperatures are the most accurate for these two modules when the pressure of the system is near the critical point.

4.2   Assessment of the order of the numerical scheme

In order to test the accuracy of the numerical scheme used, a series of one-dimensional simulations were performed. The tests consisted of convecting a gaussian-shaped temperature variation in space through a distance equivalent to 100 domain lengths. To achieve this, a constant velocity was imposed and periodic boundary conditions were used. In principle, if there are no dissipative mechanisms (for instance, thermal conductivity), the two profiles (the initial and the convected one) should always be the same. However, numerical errors that are proportional to the order of the computational scheme appear in the calculations and they cause the profiles to differ. If the numerical error is the only dissipation present, an improvement in the error should be achieved by increasing the number of computational points in the domain, which is the equivalent to reducing the cell size. Thus, the shape of the gaussian pulse after 100 "turns" was compared to the initial gaussian shape and the L_2 error was computed. For the error the following expression was used:

$$L_2 \ Error = \sqrt{\frac{1}{N_x} \sum_{i=1}^{N_x} (T_{oi} - T_{fi})^2} \tag{4.1}$$

where N_x is the number of points that were used in the simulation and T_{oi} and T_{fi} are the temperatures at point i at the initial condition and after 100 "turns", respectively. Fig. 4.2 shows one of the cases with the temperature profiles at the beginning and at the end of the simulation. The initial condition is presented in diamonds and the crosses represent the profile after 100 "turns". The small cell size (0.0025 m) helps achieve a more accurate response. Some slight differences between profiles can be observed in the 128 to 132 K range.
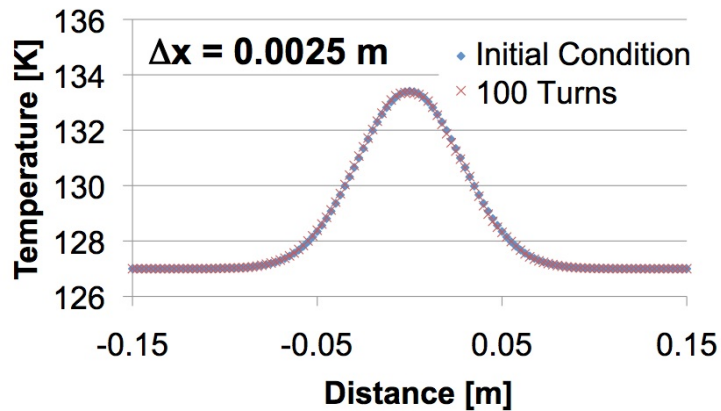

Figure 4.2: Plot reflecting the evolution of a Gaussian temperature profile of nitrogen fluid after being convected 100 domain lengths. The full domain of the pulse (not shown here) is 0.8 meters

After several similar one-dimensional simulations were performed the L_2 error as a function of cell size was retrieved for different scenarios. In a first assessment, the module AIR was used with and without thermal conductivity. One can observe in Fig. 4.3.a that, after a certain threshold, having a transport property active such as thermal conductivity will generate a numerical error that does not improve by decreasing cell size. On the other hand, when no thermal conductivity is present the value of the slope of the error as a function of cell size is closer to the order of the numerical scheme used in the simulations.
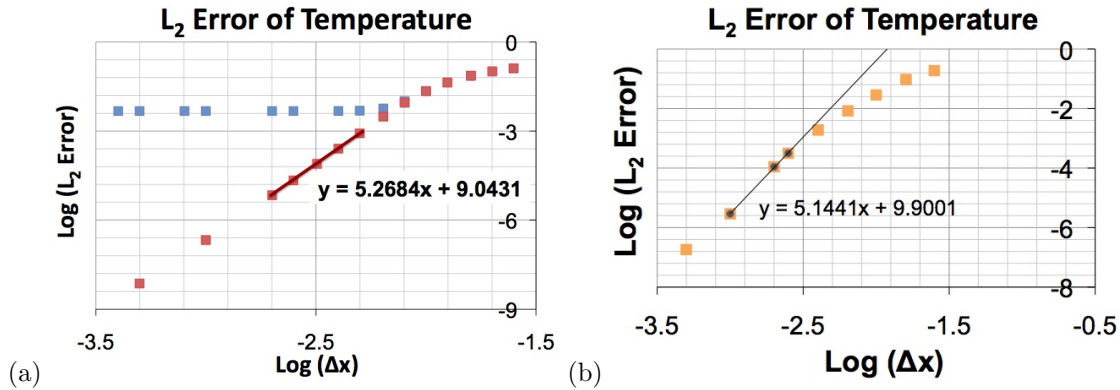

Figure 4.3: Plot of the numerical error as a function of cell size in logarithmic scale. The slope of the curve should be close to the order of the numerical scheme used in the simulation. (a) Error using the AIR thermodynamic module of YWC. (b) Error using the TRC thermodynamic module of YWC with nitrogen as fluid.

In a second study, the same procedure was followed. This time it was the module TRC that was analyzed to look for behavior resembling the order of the numerical scheme. The first data points did not give results close to the order of the scheme and appeared as if belonging to a fourth order scheme. However, after carefully reviewing points with smaller cell sizes, a trend pointing to a sixth order scheme was found as seen in Fig. 4.3.b.

4.3 Two-dimensional direct numerical simulations

The last problem considered in this study of transcritical fluids using direct numerical simulation concerns two-dimensional simulations of flows travelling in opposite directions and forming a shear layer in a rectangular domain. A hyperbolic tangent profile is used to define a smooth transition between the flows and avoid numerical artifacts at the interface. A small perturbation is introduced in the flow to initiate the development of vortical structures. A diagram showing the main flow features of this simulation is shown in Fig. 4.4

The thermodynamic module chosen for this problem was REGATH since the conditions are very close to ambient. The fluid was initialized at atmospheric pressure with a relative velocity of 20 m/s and a 10 K difference between them. The top and bottom boundaries were specified as wall boundary conditions while the side boundaries were periodic boundaries. The flow features a perturbation quantity in the vertical direction with a maximum amplitude of 2.5 m/s. The physical domain is 0.2 m by 0.2 m and the cell size is 1 mm. The CFL number is 0.7. Solutions showing the density field at different times are presented in Fig. 4.5.
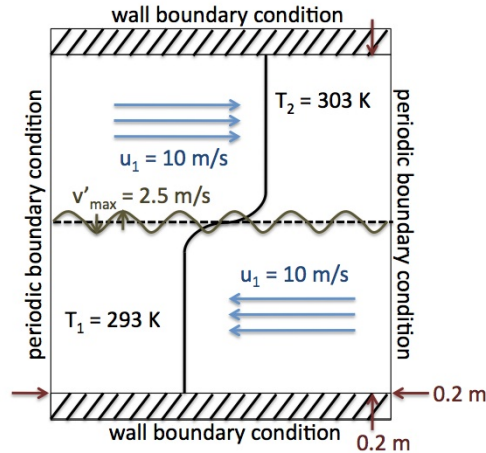
Figure 4.4: Problem modeled using the YWC direct numerical simulation code.

One observes in Fig. 4.5.a the initial condition of the flow, with two different uniform densities throughout most of the domain. At the interface there is a layer which constitutes the transition between both flows; this layer is perturbed by an imposed sinusoidal vertical velocity component that creates the characteristic wave-like appearance in Fig 4.5.b which later evolves into a wave pattern with more pronounced crests in Fig 4.5.c. This mixing mechanism is then set in motion resulting in the development of vortical structures as can be observed in Fig. 4.5.d which then eventually undergo vortex pairing and become two larger vortices between 50 and 70 ms as shown Fig. 4.6 and finally a very large vortex starts developing just after 0.1 s into the simulation (Fig. 4.7).

In the previous process, after the vortical structures are formed in the first step they continue to entrain flow into the mixing layer which grows in size and becomes very thick. The four vortices reach a stable condition for some time until a perturbation starts growing in size (Fig. 4.6.a) and each pair of vortices starts rotating into each other and merging (Figs. 4.6.b and 4.6.c). The process ends when two larger vortices are created as seen in Fig. 4.6.d. These same four steps can be seen for the same simulation in Fig. 4.7 when the two vortices in Fig. 4.6.d start merging to create a single very large vortex.

A second simulation is shown in Fig. 4.8. It has the same setup (CFL number, type of boundaries, domain size and number of nodes) and presents the same flow features shown in Fig. 4.4. The only exception being the temperature difference between the two nitrogen streams. In the first simulation the difference is 10 K and in this second simulation the difference is 200K. The density ratio between the denser flow and the lighter flow is now 2. Fig. 4.8 shows density contours of this simulation at the same physical times as the density contours shown in Fig. 4.5. The processes taking place at those times in the shear layer are practically the same even though the density ratio in the first case is only 1.03. Further simulations at higher pressures and larger density ratios between the fluid streams should provide more information into the mechanics of shear layers under transcritical conditions.
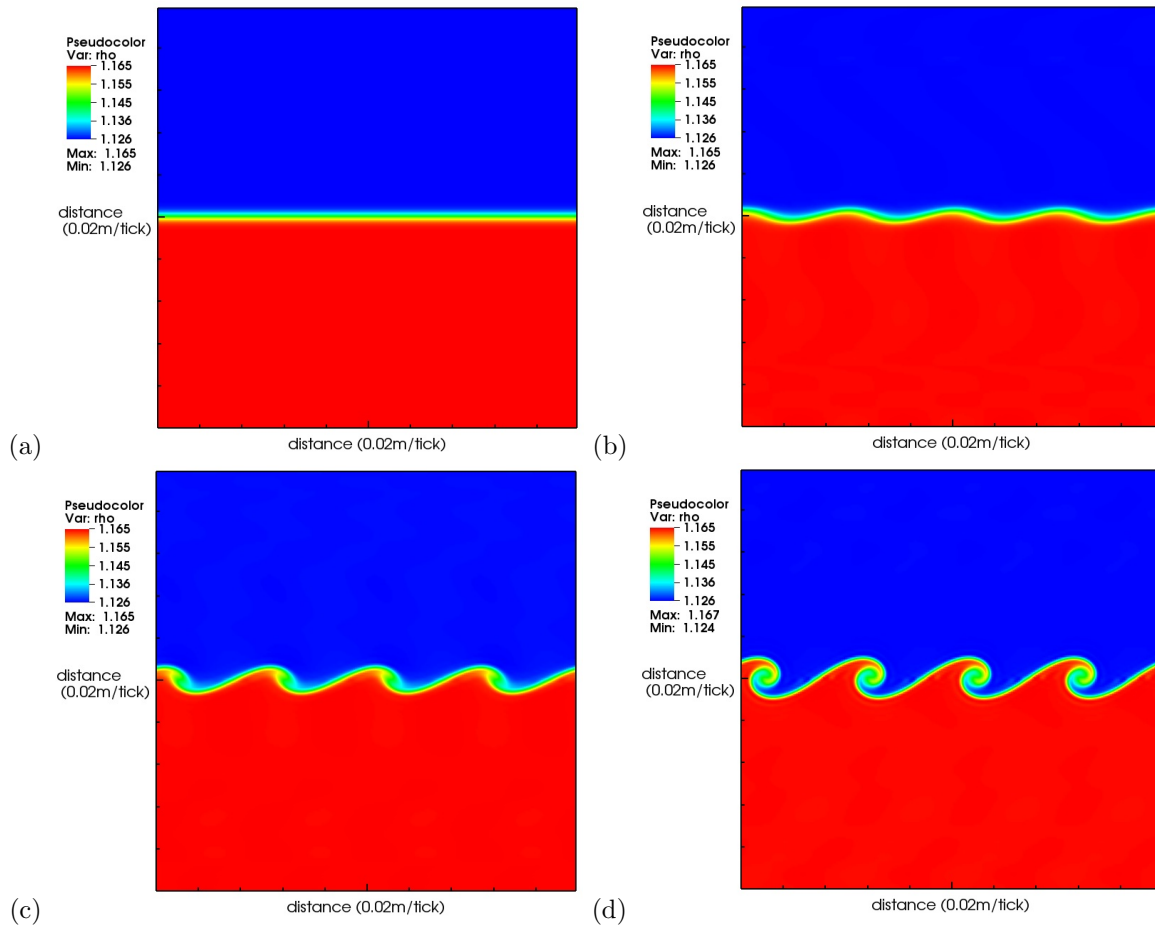
Figure 4.5: *DNS results.* Density contours at different times for a nitrogen mixing layer problem at ambient conditions. (a) 0 s, (b) 0.954ms, (c) 2.04 ms, (d) 3.25 ms. The plots correspond to a 0.20 m by 0.20 m spatial domain.
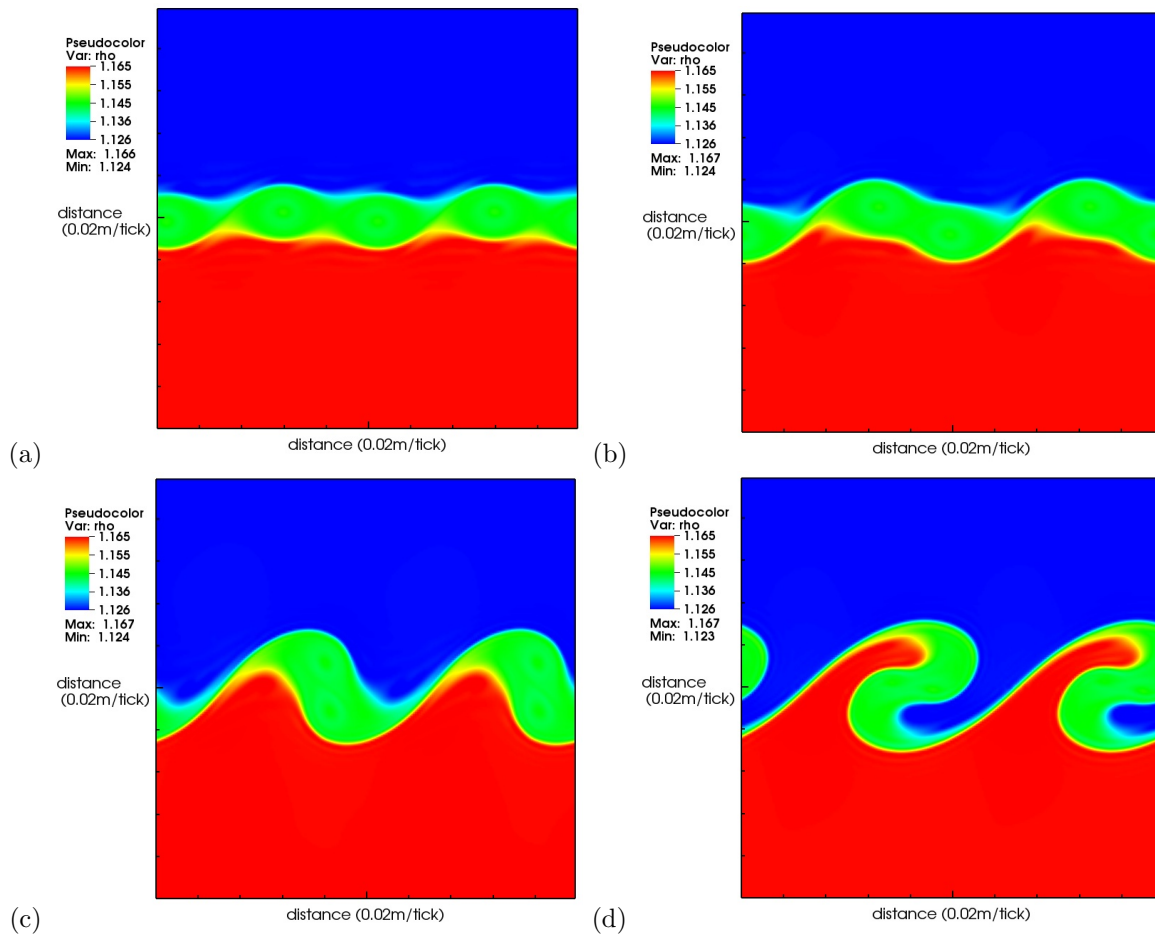
Figure 4.6: *DNS results.* Density contours at different times for a nitrogen mixing layer problem at ambient conditions. (a) 57.0 ms, (b) 60.4ms, (c) 63.5 ms, (d) 66.7 ms. The plots correspond to a 0.20 m by 0.20 m spatial domain.
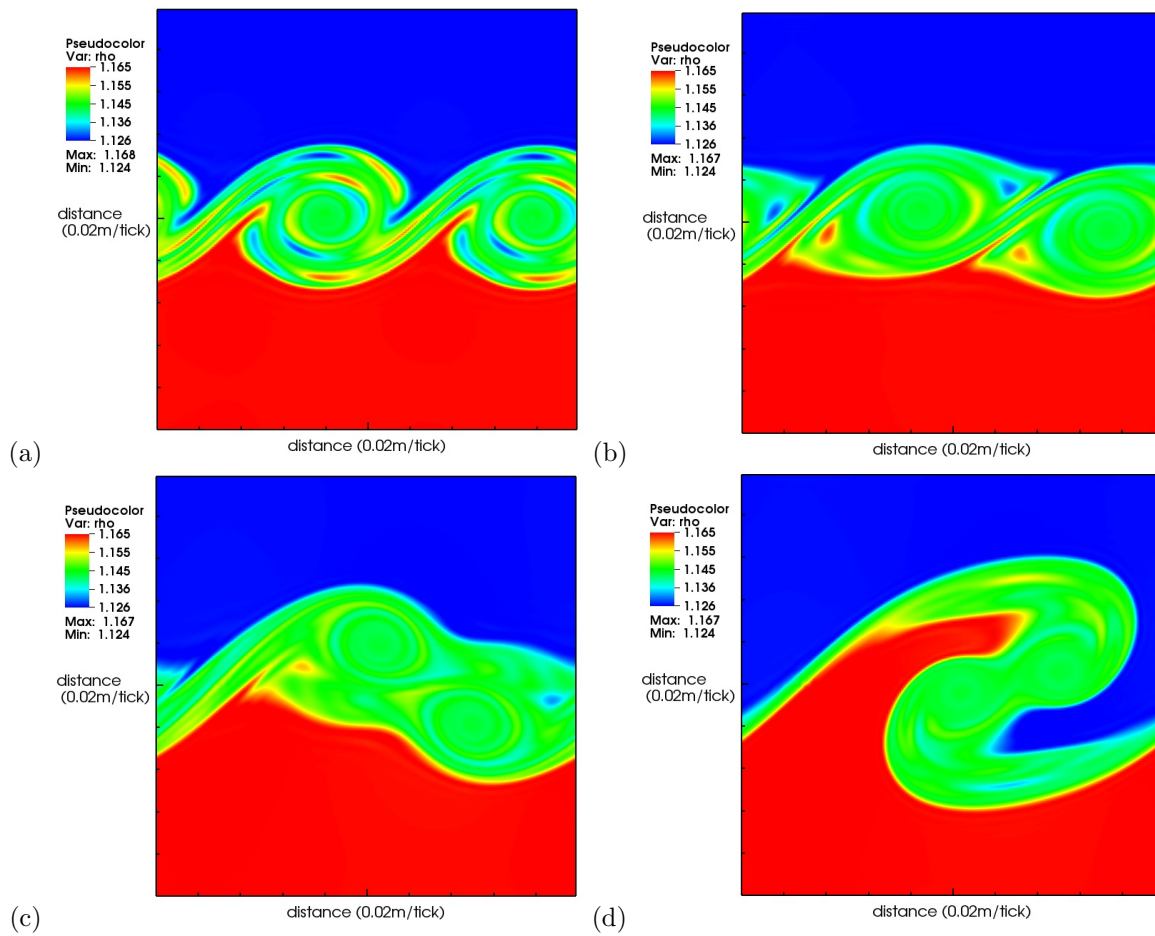
Figure 4.7: *DNS results.* Density contours at different times for a nitrogen mixing layer problem at ambient conditions. (a) 94.9 ms, (b) 112 ms, (c) 122 ms, (d) 130 ms. The plots correspond to a 0.20 m by 0.20 m spatial domain.
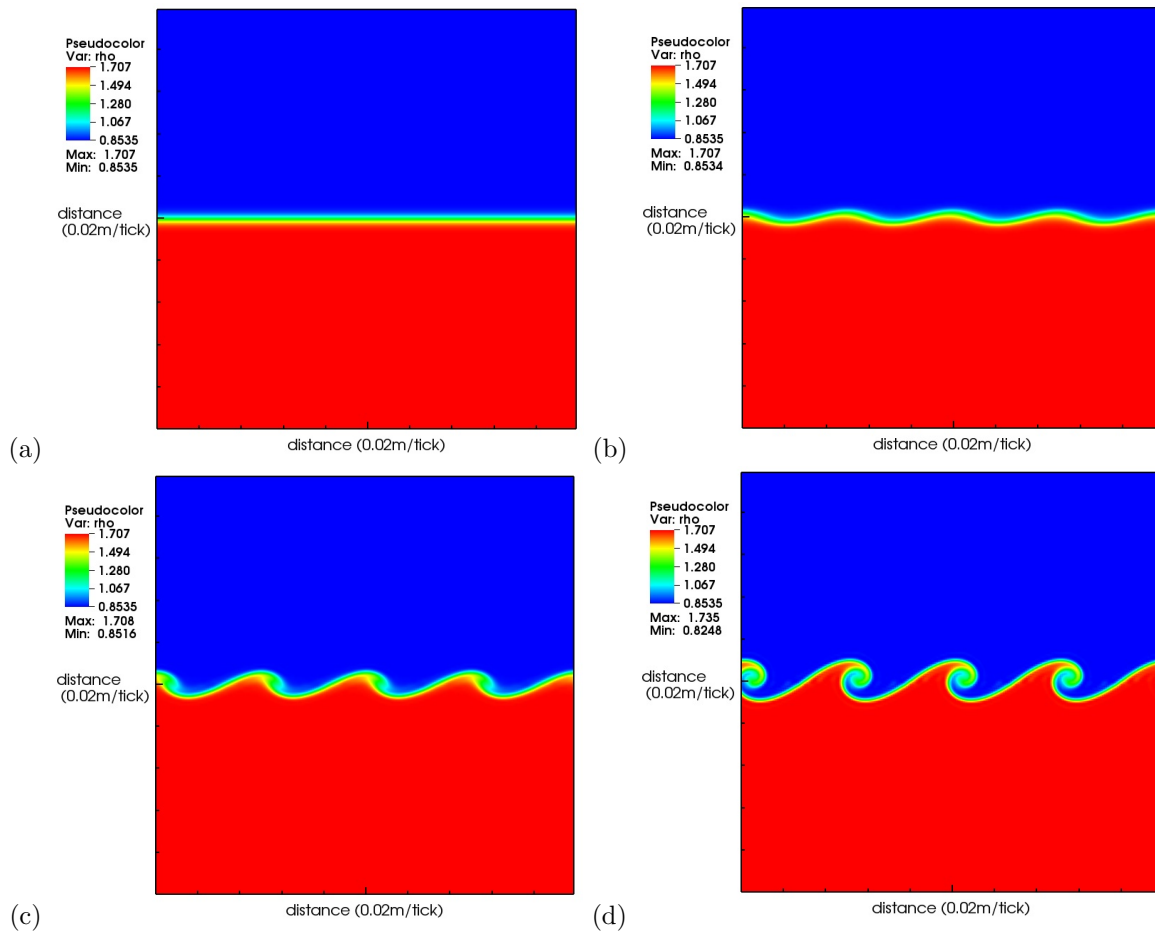
Figure 4.8: *DNS results.* Density contours at different times for a nitrogen mixing layer with a temperature difference of 200K between the two nitrogen streams. (a) 0 s, (b) 0.954ms, (c) 2.02 ms, (d) 3.31 ms. The plots correspond to a 0.20 m by 0.20 m spatial domain.

Chapter 5

Conclusions

Different aspects of the direct numerical simulation of fluid problems were studied in this part of the report. This has been accomplished with the help of a new modeling tool developed at the EM2C laboratory. The code, YMC, has been developed with a large variety of applications in mind and the need to understand many of its functionalities was emphasized. In particular, the use of thermodynamic modules to address different types of problems led to the analysis of the equation of state of the two modules that dealt with real gas formulations, which is the type of thermodynamic capability needed for the larger goal of the current research efforts. Also, the results of one-dimensional validation cases were used to confirm the accuracy of the numerical scheme to sixth order, which was the order of the scheme employed to solve the governing equations. Furthermore, two-dimensional simulations of a nitrogen mixing layer were performed to analyze the behavior of the flow in the interface and study its behavior. The different tasks performed during this research helped understand and assess the different characteristics of direct numerical simulation methods, and later apply the obtained knowledge to the solution of a relevant problem.

Acknowledgments

Bibliography

[1] Okong'o, N., Bellan, J., "*A Priori* Analysis of Subgrid-Scale Models for Large Eddy Simulations of Supercritical Binary-Species Mixing Layers", *43rd AIAA Aerospace Sciences Meeting and Exhibit*, AIAA 2005-0155.

[2] Okong'o, N., Bellan, J., "Direct Numerical Simulation of a Transitional Supercritical Binary Mixing Layer: Heptane and Nitrogen", *Journal of Fluid Mechanics, 464*, (2002) 1-34.

[3] Selle, L., Ribert, G., "Equation of State Effects for Turbulent Flows Under Supercritical Conditions and their Impact on Modeling Strategies", *2nd Colloque INCA*, (2008) Rouen, France.

[4] Selle, L. C., Okong'o, N. A., Bellan, J., Harstad, K. G., "Modelling of Subgrid-Scale Phenomena in Supercritical Transitional Mixing Layers: An *A Priori* Study", *Journal of Fluid Mechanics, 593*, (2007) 57-91.

[5] Lele, S. K., "Compact Finite Difference Schemes with Spectral-Like Resolution", *Journal of Computational Physics, 103*, (1992) 16-42.

[6] Lemmon, E., McLinden, M., Friend, D., **Thermophysical properties of fluid systems**, *NIST Chemistry WebBook, National Institute of Standards and Technology*, http://webbook.nist.gov, (2005).

Nomenclature

CFL	Courant–Friedrichs–Lewy (a condition of convergence in partial differential equations)
CNRS	Centre National de la Recherche Scientifique (France)
δ_{ij}	Kronecker delta (function that can be only 0 or 1 depending on the values of i and j)
D_k	diffusivity of species k
DNS	Direct Numerical Simulation
e	specific energy or total energy divided by mass ($e = E/m$)
EM2C	Energétique, Moléculaire, Macroscopique et Combustion
FSA	Faculté des Sciences Appliquées
LES	Large Eddy Simulation
μ	dynamic viscosity
NIST	National Institute of Standards and Technology
P, p	pressure
P_c	critical pressure
P_r	reduced pressure ($P_r = P/P_c$)
q_i	heat flux vector
ρ	density
Re	Reynolds number ($Re = \rho u l / \mu$)
REGATH	REal GAs THermodynamics
SGS	Subgrid Scale
T	temperature
t	time
τ	viscosity stress tensor
TRC	TRansCritical
u_i	abbreviated notation for the three velocity components u, v and w
$\dot{\omega}_k$	net production rate of species k
x_i	abbreviated notation for the three Cartesian coordinates x, y and z
Δx	length between nodes in a computer simulation, cell size
Y_k	mass fraction of species k
YWC	Yes We Can (an EM2C DNS code)